Electronic Properties and Charge Transport of Polyhedral Oligomeric Silsesquioxanes (POSS) Derivatives and Materials Design for Highly Efficient Organic Light Emitting Diodes

by

Changgua Zhen

A dissertation submitted in partial fulfillment
of the requirements for the degree of
Doctor of Philosophy
(Materials Science and Engineering)
in The University of Michigan
2011

Doctoral Committee:

Professor John Kieffer, Chair
Associate Professor Jinsang Kim
Associate Professor Max Shtein
Assistant Professor Barry D. Dunietz

Acknowledgements

I would like to thank my advisor Prof. John Kieffer for training and instruction on computation and simulation and thank Prof. Barry Dunietz, Prof. Jinsang Kim, and Prof. Max Shtein for helpful discussions. I would like to thank my experimental cooperators, Dr. Zhikuan Chen and Mr. Yanfeng Dai for their support. Also special thanks to my friends Dr. Chandrashekar Shankar, Dr. Arun Kumar Upadayay for many intellectually inspiring conversations and research help without which this thesis could not have been completed. Last but most importantly, I want to thank my wife, Xiuzhen Mai, for her years of support in my life.

Table of Contents

List of figures

List of tables

List of appendices

Abstract

The building units for organic semiconductors are molecules. Due to the basic nature of molecules, these organic materials can be easily modified with functional groups to control their properties and adapt them for specific optoelectronic applications.

Polyhedral oligomeric silsesquioxane (POSS) is used as an example to illustrate the tunability of the electronic properties of organic semiconductors. The structure and electronic properties of polyhedral oligomeric silsesquioxane (POSS) cages functionalized with different organic groups are studied using density functional theory (DFT) and time-dependent density functional theory (TDDFT) calculations. The POSS cage is quite rigid upon functionalization and thus provides a means for controlling the orientation of organic fragments attached to it, which is useful to design novel organic molecular architectures and assemblies. Moreover, the electronic properties can be tuned through the choice of functional groups and their positioning on or within the POSS cage. Attaching an electron-donating group, such as 4-carbazolephenyl, to the silicon atom at the corner of the cage raises the highest occupied molecular orbital (HOMO) level, while attaching an electron-withdrawing group, such as 4-cyanophenyl, to the POSS cage decreases the lowest unoccupied molecular orbital (LUMO) level. Frontier orbital analysis indicates that POSS cage is partially conjugated and serves the role of electron acceptor. Charge transport properties are discussed in the framework of Marcus' electron

hopping theory. Based on the calculated reorganization energies these POSS compounds can be used as carrier transporting or blocking materials, depending on the functionalization. Exciton binding energies were found to strongly depend on the spatial arrangement of frontier orbitals rather than on molecular sizes.

By functionalizing the POSS cage with two pentacene molecules along the diagonal direction, we construct dipentacene POSS hybrid organic-inorganic semiconductor materials. Unlike the herringbone pattern in the pentacene single crystal, in which the neighboring pentacene molecules form V-shape dimers, the dipentacene POSS molecules adopt a parallel configuration in its single crystal that was predicted with molecular dynamics. This parallel configuration enhances the wavefunction overlap between pentacene segments, resulting in fast charge hopping between the molecules. A multi-scale hopping model based on Marcus' electron transfer theory was developed to simulate the charge transport in dipentacene POSS crystal. The simulated hole mobility in dipentacene POSS can be as high as 415 cm^2/Vs at room temperature, compared to 31 cm^2/Vs for pure crystalline pentacene.

The insight gained into the tuning of electronic properties and charge transport was used to design materials for organic light emitting diodes (OLEDs). Based on the results of first-principles calculations of the electronic properties of blue light emitting materials, we optimized the molecular structures by incorporating electron-withdrawing groups into the molecules to balance hole and electron injection and transport for organic light-emitting diodes (OLEDs), resulting in a remarkable improvement in the maximum external quantum efficiency (EQE) of the undoped device from 2.0% to 4.99%. Further

optimization of the device configurations and processing procedures, e.g., by changing the thickness of the emitting layer and through thermal annealing treatments, leads to a very high maximum EQE of 7.40% for the undoped sky-blue device. Finally, by doping the emitters in a suitable host material, 4,4'-bis(carbazol-9-yl)biphenyl (CBP), at the optimal doping concentration, deep blue emission with extremely high maximum EQE of 10.7% and CIE coordinates of (0.151, 0.088) were achieved. The high EQE far exceeds the traditional upper limit of 5% if the singlet generation fraction in fluorescent OLEDs is 25%. A survey of the literature published in the last two decades indicates that singlet generation fraction can be higher than 25%. Using a model developed from Fermi's golden rule, we found that singlet generation fraction of most of the organic emitters for OLEDs is in the range of 40% - 70%. This result clearly indicates that fluorescent materials can make more important contributions to highly efficient and stable OLEDs than previously thought.

The successful materials design for OLEDs suggests that we can prescreen and optimize molecular structures before synthesis in the lab, to avoid iterative and costly Edisonian approaches.

Chapter 1. Introduction of organic semiconductors

1.1. Introduction

Organic semiconductors are of great interest for applications such as organic light-emitting diodes (OLEDs),[1,2] organic solar cells,[3,4] and organic field effect transistors (OFETs).[5,6] Using organic semiconductors in place of inorganic ones as active elements in devices has the potential to: lower the cost fabrication, allow application targeted modifications, improve compatibility with substrates including flexible plastics, and allows the manufacture of light-weight and large-area products.[7] Backing these advantages is the molecular nature of organic semiconductors, i.e., organic semiconductor is a solid-state aggregation of organic molecules or polymer chains, bound by the van der Waals forces. Van der Waals binding is much weaker than covalent bond or ionic bond. This weak interaction between organic molecules induces localized electronic states, which causes unique optical and charge transport properties compared with inorganic semiconductors. Due to the weak intermolecular forces, organic semiconductors can be dissolved in common solutions. They can therefore be processed in solution form by methods such as spin-coating and roll-to-roll printing. Furthermore, the stacking of molecules during the growth process of organic solids from thermal evaporation or solution is random, leading to less ordered structures compared with inorganic crystalline compounds. The spatial arrangement of the organic molecules plays

an important role in electronic properties such as carrier mobility, exciton migration, exciton degradation, and so on. In some cases such as OFETs, random stacking is detrimental because ordered and continuous π-π stacking can form conduction channels for high carrier mobility, which is desired. In other cases, such as emission layer in OLEDs, ordered π-π stacking is to be avoided because it will induce self-quenching leading to lower quantum efficiency. The stacking of molecules is affected by growth conditions such as pressure, temperature, substrate type, and growth rates. Hence, controlling the growth condition can effectively control the properties of solid organic thin films.

Due to their molecular nature, the organic materials can also be easily modified with functional groups to control their properties for specific optoelectronic applications. For instance, electron-donating groups, and electron-withdrawing groups are often used to alter electronic properties of organic materials. Long and flexible alkyls are used to enhance the solubility of large conjugated molecules and polymers. Such subtle changes of the chemical structure of organic/polymeric materials will induce significant variation in chemical, electrical and mechanical properties. Therefore, sequences of molecules with small differences in structure are often synthesized simultaneously, from which the desired ones will be chosen for specific applications.

Despite the attractive features, the performance of many organic electronic devices is far below that of their inorganic counterparts. For example, the power efficiency of OLEDs is not as high as expected because of the low conductivity of organic amorphous films.[8] Because of this low conductivity, to achieve practical current densities or

adequate response rates, the conducting pathways must be kept shorter in organic amorphous materials than in inorganic crystalline materials, *i.e.*, the layer thickness in organic electronic devices must be limited to the order of about 100 nm. Several problems are associated with forming such thin organic films. For example, ultra-thin films are very sensitive to micro- or nanoscale protrusions on substrates and contaminating particles, which can cause pinholes or aerial defects prone to leakage currents, and can even lead to failure during operation. Thus, low-roughness substrates and very clean fabrication environments are required, which raises production cost. Consistent performance of devices is difficult to achieve because of the typical thickness variation in ultra-thin films. Hence, there is a strong incentive for developing highly conductive materials that allow for thicker charge transport layers while maintaining comparable current intensities and signal response times. Another issue is that the maximum power efficiency of organic solar cells is around 5%,[4] while inorganic solar cells can achieve more than 20%.[9] One of the main reasons for this shortcoming is the large exciton binding energy in organic materials.[10,11]

As mentioned above, to some degree, the properties of organic semiconductors can be controlled via the process parameters that affect the growth kinetics. However, the tendency of a material to assemble into a structure with a particular order ultimately depends on the geometry and functionality of its elementary building blocks. Hence, there exists an ongoing quest to develop novel molecules, from which materials with desirable properties can be made. Before they can measure the properties of new functional materials, researchers spend a significant amount of time and resources to identify the appropriate synthesis routes and optimal growth conditions for the newly

conceived organic molecules. Due to the complexity of molecules, organic synthesis methods possess enormous flexibility. While this provides virtually endless possibilities for molecular design, it also poses the challenge of multi-variable searches. Oftentimes this requires an iterative and costly Edisonian approach. In some cases this method may never result in a satisfactory outcome, simply because the desired properties are inherently impossible to achieve for a given molecular system. Hence, at the heart of my thesis research lies the development of efficient strategies for exploring such a vast parameter space.

1.2. A brief history of organic semiconductor materials and devices

In1862, Henry Letheby obtained a partly conductive material by anodic oxidation of aniline in sulfuric acid. The material was probably polyaniline.[12] In the 1950s, semiconductor charge-transfer complex salts achieved a high conductivity of ~ 0.1 S/cm. Similar conductivity values were reported in linear backbone polymers of polypyrrole (in an iodine-"doped" and oxidized polypyrrole black) in 1963.[13-15] In 1977, Shirakawa *et al.* reported high conductivity in oxidized and iodine-doped polyacetylene[16,17], which ignited enthusiasm in organic semiconductors and device research in academia and industry.

1.2.1. Organic light-emitting diodes

In addition to the development of conducting polymers, investigations of molecular organic semiconductors were also in progress. Since the transport properties of organic semiconductors are strongly dependent on molecular order in organic solids, most of the initial studies of the solid-state properties of these materials used molecular crystals. The

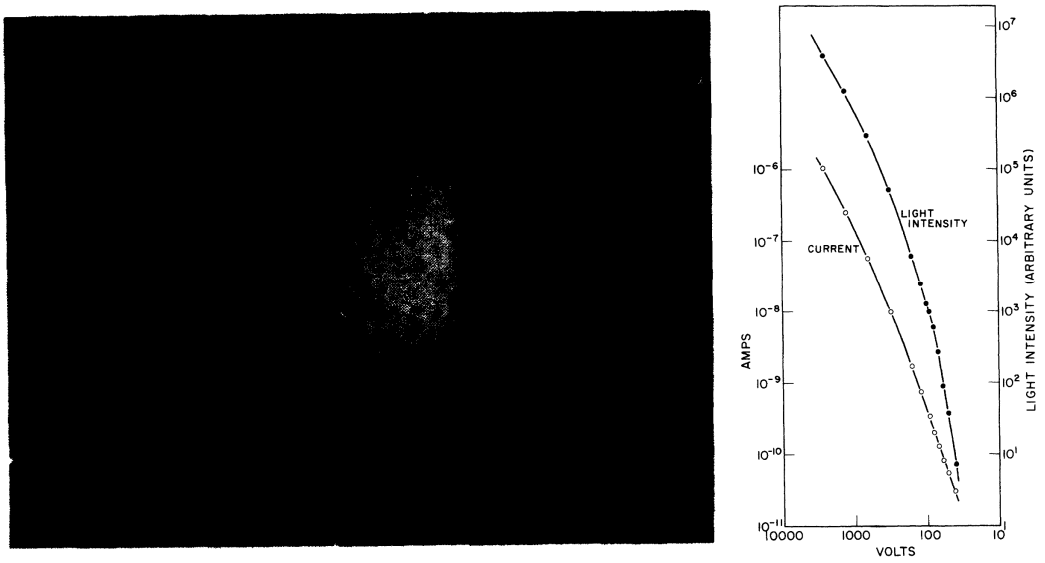

Figure 1.1. The photograph of the recombination radiation and current-voltage-luminescence characteristics of the first organic electroluminescent device. The driving voltage was around $10^2 \sim 10^3$ V. The region of the maximum brightness zone (right-hand side) was close to the positive electrode. The active material was a 5mm anthracene crystal. From Helfrich and Schneide (1965).

first electroluminescent device was reported by Helfrich who used a 5 mm thick anthracene crystal as the active material (Figure 1.1). The operation voltage of the device was $10^2 \sim 10^3$ V, which was not suitable for practical applications. Using a much thinner polycrystalline anthracene film of 0.6 μm as the active material notably reduced the operation voltage to around 30 V, but the quantum efficiency of these single-layer devices was low because the electron-hole recombination zone was near the hole-injection electrode.

A substantial step forward in OLEDs towards practical applications came with the invention of Tang's thin film devices (Figure 1.2).[1] These devices were fabricated from thin (less than 100 nm) amorphous organic layers deposited by thermal evaporation in

vacuum. The substrate was low-cost ITO coated glass with a sheet resistance around 10-20 Ω/square. 75 nm of aromatic diamine was deposited on top of ITO, followed by deposition of 60 nm Alq_3, before a final layer of low-work-function metal alloy. The performance of the OLEDs was very promising with 1% quantum efficiency, 1.5 lm/W power efficiency, and high brightness (>1000 cd/m^2) at a driving voltage below 10 V. The most notable contribution of Tang is that he invented the first organic heterostructure. Unlike the single layer organic devices, in an organic heterostructure, holes and electrons are injected and transported in electron-donating and electron-withdrawing organic materials. This structure improves the balance of holes and electrons inside the emitting zone. The efficiency of recombination of electrons and holes is thus greatly enhanced. In contrast, in single-layer organic devices, either the hole or the electron is the minority charge while the other one is the majority charge. Most of the majority charges will

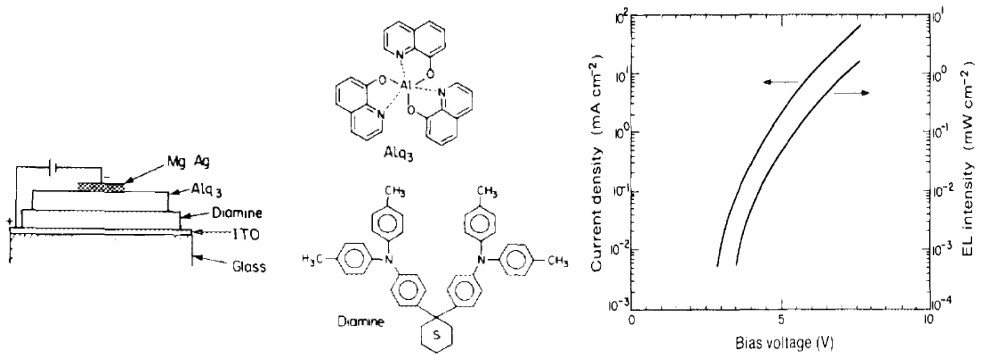

Figure 1.2. Device configuration, molecular structures of the *p*-type (diamine) and *n*-type (Alq_3) organic semiconductors and device performance of Tang and Van Slyke's heterojunction organic light-emitting diode. The operational voltage was less than 10 V. Diamine is an electron donor that can transport holes and Alq_3 is an electron acceptor that can transport electrons. From Tang and Van Slyke (1987).

migrate to the opposite electrode without recombining with the minority charges, resulting in low recombination efficiency and poor device performances.

Tang's work on OLEDs encouraged many chemists, materials scientists and electrical engineers to further examine and expand the concepts behind, and enhance the performance of OLEDs, making this technology capable of practical applications, e.g., displays and lighting. Tang's other contribution is the application of the guest-host system in organic electronics (Figure 1.3).[18] For full-color display applications, emitters with various emissions spanning the whole visible region of light are required. Making

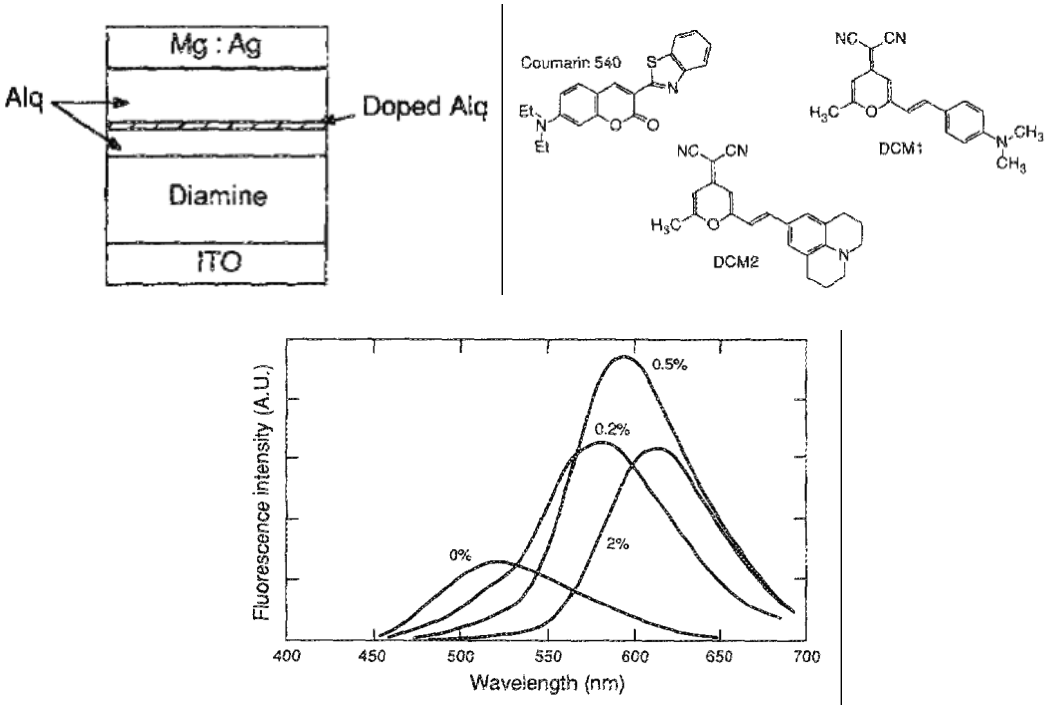

Figure 1.3. Configuration of Tang's doped organic light-emitting diode, the molecular structure of the semiconductors used in the device, and the electroluminescent spectra of doped devices as a function of dopant (DCM1) concentration in the host (Alq_3). The red-shift of the spectra with the increasing dopant concentration clearly demonstrated the energy transfer from host to dopant. From Tang, Van Slyke, and Chen (1989).

these emitters was challenging due to the difficulty of finding emitting materials with desired color, high fluorescent quantum efficiency, and simultaneously, the ability to transport charge. Tang and his coworkers demonstrated that a small amount of highly fluorescent dye (guest) could be doped into a charge transport material (host) to achieve desired color and high quantum efficiency because there was a complete energy transfer from the host to the guest. This guest-host design in device configurations allows that: (1) the functions of charge transport and luminescence can be realized by two materials that can be chemically tailored separately; (2) higher quantum efficiency can be achieved due to less concentration quenching; (3) the search for suitable materials for desired colors can be focused on the guest materials.

Conjugated polymers were also used for light-emitting diodes.[2] Compared to molecular organic materials, polymers are too large to be thermally evaporated. Therefore, most of the conjugated polymers used in organic semiconductors are processed from solution, through casting, spin-coating, screen-printing, injet-printing or other techniques.

Both of the fluorescent dyes and conjugated polymers used in light-emitting diodes can generate singlet excitons and triplet excitons in an electrical field. Triplet excitons cannot radiatively decay to the singlet ground state due to selection criteria for electronic transitions in organic semiconductors. Therefore, a large part of excitation energy carried by triplet excitons cannot be utilized for luminescence. The first high-efficiency OELD harvesting triplet excitons was reported by Forrest's group. In their OLED a phosphorescent emitter, 2,3,7,8,12,13,17,18-octaethyl-21H,23H-porphine platinum(II)

(PtOEP), was doped in Alq_3 host.[19] The heavy atom, platinum, enhances the spin-orbit coupling so that the triplet states gain additional singlet character and vice versa. This opens a radiative decay channel for triplet- excited states to singlet ground states. The utilization of phosphorescent dyes in OLEDs has led to 100% internal quantum efficiency.[20]

Besides development for display industry, high efficiency white OLEDs can be used for lighting applications with their potential for significantly improved efficiency over traditional lighting sources, low-cost, high-throughput manufacturability, and high color-rendering qualities. The first white organic electroluminescent device was reported by Ogura.[21] In this device the spectrum was composed of blue and orange emissions. Generally there are three strategies to generate white light: (1) utilizing exciplex emission that covers a broad spectrum range from a single component in a single emissive layer; [22,23] (2) combining complementary emissions from a multiply doped single emissive layer; [24,25] (3) combining complementary emissions from multiple emissive layers.[26,27]

New materials, device configurations, and concepts have since been developed to enhance the energy efficiency and reduce the cost of OLEDs, in order to compete with and replace incandescent lamps and fluorescent tubes. Sun *et al*. used fluorescent dyes to harness the high-energy singlet exciton for blue emission, and used phosphorescent dyes to harness low-energy triplet exciton for green and red emissions (Figure 1.4).[28] By this strategy, they successfully eliminated the exchange energy loss to the blue fluorophore, which allows for roughly 20 per cent increased power efficiency compared to a fully phosphorescent device. Their lab achieved a total external quantum efficiency of 18.4 ±

0.5 % and power efficiency of 23.8 ± 0.5 lm/W at a high luminance of 500 cd/m^2. Reineke *et al.* have achieved 90 lm/W at 1000 cd/m^2 by combining a carefully chosen emitter layer with high-refractive-index substrates, and using a periodic out-coupling structure.[29] Further engineering of the light extraction can improve the power efficiency to 124 lm/W,[29] which is much superior to fluorescent tubes which normally have a power efficiency of 60-80 lm/W.

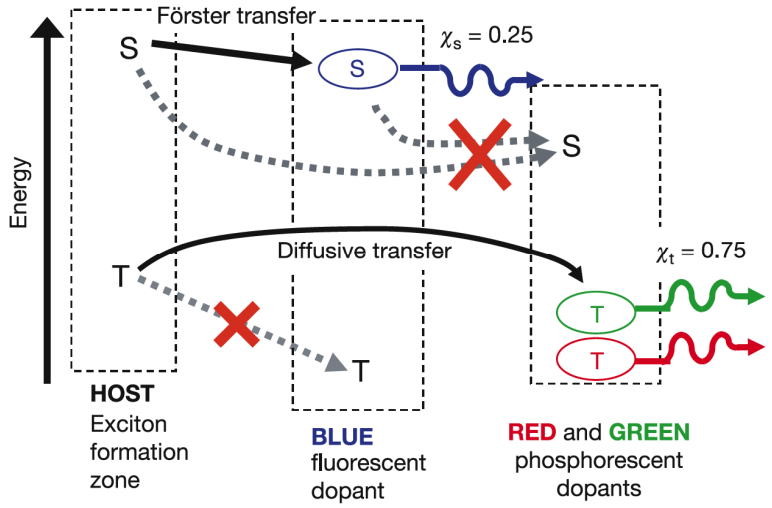

Figure 1.4. Energy transfer mechanisms in the fluorescent/phosphorescent WOLED proposed by Sun *et. al.*. Triplets (T) and singlets (S) form and transfer directly onto their corresponding emissive dopants by separate channels. The majority of excitons are formed in the host material. The singlet excitons are rapidly, and near-resonantly, transferred to the blue fluorescent. The phosphor-doped region is located in the center of the emitting layer and separated from the exciton formation zones by spacers of undoped host material. The triplets then diffuse efficiently to the central region, where they transfer to the lower energy green or red phosphor dopants, again by a nearly resonant process to the green dopant triplet manifold, and with some energy loss to the red triplet. Diffusion of singlet excitons to the phosphor dopants is negligible due to their intrinsically short diffusion lengths. From Sun *et. al.* (2006).

1.2.2. Organic solar cells

In 1906, Pochettino observed photoconductivity in anthracene.[30] This was the first time that photovoltaic and related properties were observed in organic compounds. Research on photovoltaic effects such as photovoltages in organic materials to a large extent began in 1950s. Before Tang's heterojunction organic solar cells (Figure 1.5), published in 1986,[3] the conventional structure of the cells was a single layer of organic material sandwiched between two dissimilar electrodes, in which the built-in potential was determined by the difference in work function of the electrodes or by the Schottky

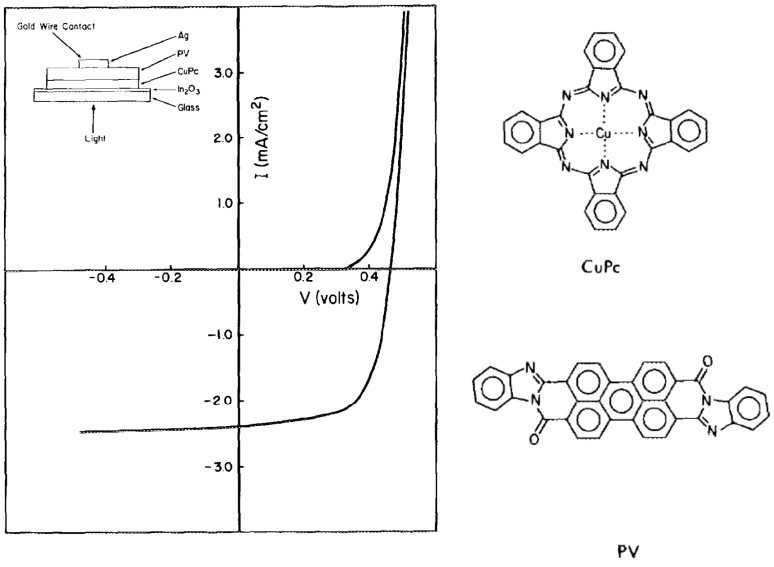

Figure 1.5. Device configuration of Tang's heterojunction photovoltaic cell and the chemical structures of the *p*-type (CuPc) and *n*-type (PV) materials. 30nm of copper phthalocyanine (CuPc) and then 50nm of a perylene tetracarboxylic derivative (PV) were thermally deposited on an ITO-coated glass substrate. A thin layer of Ag was used as the top contact. Excitons are generated in the organic layers after light absorption and diffuse to the organic/organic interface where they are dissociated into free holes and electrons, which are collected to electrodes through *p*-type and *n*-type organic layers. From Tang (1986).

barrier at one of the metal/organic interfaces.[31-37] Although the power conversion efficiency of Tang's heterojunction cell was around 1%, not much better than from a single layer organic solar cell (for example, Morel's highly efficient cell[35]), the fill-factor of the heterojunction cells was much higher than for the single layer cells. Tang proposed that the photo-generated excitons are dissociated at the organic/organic interface where a built-in field is sufficiently high to break the excitons into free holes and electrons that migrate in *p*-type (CuPc) and *n*-type (PV) organic materials towards the electrodes. In this case, the carrier generation efficiency would be primarily determined by the diffusion of excitons into the organic/organic interface. Applying a small external voltage would moderately affect the carrier collection, thus leading to a weak bias dependence of the photocurrent, that is, leading to a higher fill factor.

As Tang pointed out, the organic/organic interface plays a critical role in organic solar cells. Hiramoto *et al*. introduced a co-deposited *p*-type and *n*-type mixture layer between pure *p*-type and pure *n*-type layers. The photocurrent increased to 2 fold compared with the bilayer heterojunction device without the co-deposited layer. Yu *et al*. further proposed the concept of "bulk heterojunction" which was composed of interpenetrating phase-separated *p*-type and *n*-type polymers or molecular domains (Figure 1.6).[38] The ideal situation is for any point in the network to be close to the *p*-*n* interface so that the photo-generated excitons can diffuse to the interface to dissociate to free carriers before de-excited, while each phase is continuous for carrier transport. Therefore, controlling morphology in dispersed heterojunction devices is a critical point. The degree of phase separation and domain size depends on solvent choice, rate of solvent evaporation,

chemical solubility, miscibility of the donor and acceptor, etc.[38] On the basis of this concept, a high energy conversion efficiency of >6% has been achieved recently.[39]

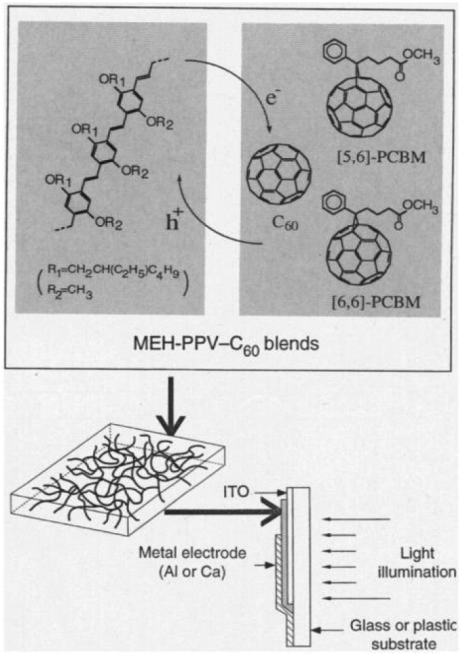

Figure 1.6. Schematic diagram of the photoinduced charge transfer process in MEH-PPV:C60 donor (D)-acceptor (A) blends and the structure of the photovoltaic cell fabricated. When cast as a film, the D and A species phase-separate into a bicontinuous network (bulk heterojunction material), as shown schematically. From Yu *et. al.* (2006).

1.2.3. Organic transistors

Printable organic transistors are versatile, thinner and more efficient compared to traditional transistors based on inorganic semiconductors because organic semiconductors are compatible with plastic substrates due to similar expansion coefficient and flexibility. This technology has potential applications in electronics for flexible, lightweight displays, e-books, RFID, and smart labels and packages.

At the end of the 1980s, several groups studied transistors using organic materials as the active materials.[40-42] During this time, Garnier demonstrated the potential applications of organic transistors in flexible electronics.

In 1989, Garnier and co-workers reported their organic transistors with a structure as shown in Figure 1.7. The active material they used was alpha-sexithiophene. They obtained a field effect mobility of 10^{-3} cm^2/Vs, several orders of magnitude larger than reported in previous organic thin film transistors. Subsequently, Garnier and co-workers demonstrated flexible transistors in which all components are made from polymers using printing techniques (Figure 1.8).[43] The insulating layer they used was polyethylene terephthalate, the gate, source and drain electrodes were from a conducting graphite-based polymer ink, and the organic semiconductor was α,ω-di(hexyl)sexithiophene.

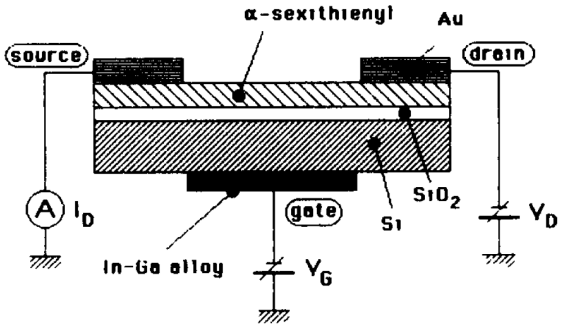

Figure 1.7. A schematic view of Horowitz and Garnier's organic thin film transistor. From Horowitz *et al*. (1989)

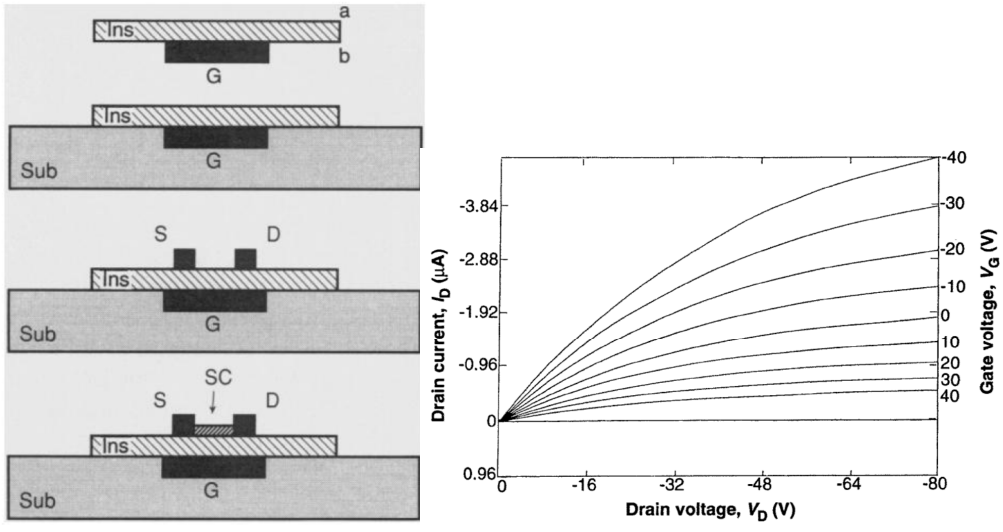

Figure 1.8. Fabrication steps of the all-polymer transistor (left) and drain current versus drain voltage curves at various gate voltages for the all-polymer transistor (right). From Garnier *et al*. (1994)

Although Garnier's contribution demonstrated that organic transistors could be potentially low-cost due to printable characteristics of organic materials, the performance of the organic transistors were not as good as their inorganic counterparts, especially their low charge mobility. Recently, Yan *et al*. reported that their *n*-type organic semiconductors had an electron mobility as high as 0.85 cm^2/Vs, comparable to or even better than amorphous hydrogenated silicon.[44] Using their *n*-type organic semiconductors, they successfully fabricated all-printed polymeric complementary inverters.[44]

1.3. Charge transport and energy transfer in organic semiconductors

Excited molecular states can transfer from one molecule to another with conservation of their spin and energy, which can be treated as particles, or 'excitons'. An exciton can be modeled as a two-electron system: one electron is excited into a higher energy orbital while leaving another one in a partially filled orbital. The total spin of the system is the vector sum of the spins of the individual electrons:

$$\vec{S} = \sum_{i=1}^{n} \vec{S}_i \tag{1.1}$$

The individual spin quantum numbers S_1 and S_2 are both 1/2. The total spin of such a two-electron system can be $S = 0$ or $S = 1$, corresponding to the two spins being antiparallel or parallel. For the same spatial electronic wavefunction, the degeneracy is determined to be $2S + 1$.

The spin wavefunction for $S = 0$ is antisymmetric under particle exchange:

$$\sigma = \frac{1}{\sqrt{2}}\left[\alpha(1)\beta(2) - \beta(1)\alpha(2)\right] \tag{1.2}$$

where α and β represent the possible spin states of each electron. The electrons are denoted by (1) and (2). For S = 1, there are three possible spin wavefunctions, all symmetric under particle exchange:

$$\sigma = \alpha(1)\alpha(2) \tag{1.3}$$

$$\sigma = \frac{1}{\sqrt{2}}\left[\alpha(1)\beta(2) + \beta(1)\alpha(2)\right] \tag{1.4}$$

$$\sigma = \beta(1)\beta(2) \tag{1.5}$$

In a two-electron system, symmetric and antisymmetric spatial wavefunctions ψ_+ and ψ_- satisfy

$$\psi_+(\mathbf{r}_1,\mathbf{r}_2) = \psi_+(\mathbf{r}_2,\mathbf{r}_1) \tag{1.6}$$

$$\psi_-(\mathbf{r}_1,\mathbf{r}_2) = -\psi_-(\mathbf{r}_2,\mathbf{r}_1) \tag{1.7}$$

under particle exchange.

The probability of electron transition is proportional to the electronic dipole moment between the initial and final electronic states. For a two-electron system, the electric dipole moment operator is $-e\mathbf{r}_1 - e\mathbf{r}_2$, and the dipole moment between states of different symmetry is

$$\mu = -e\left\langle \psi_+(\mathbf{r}_1,\mathbf{r}_2)\middle|(\mathbf{r}_1 + \mathbf{r}_2)\middle|\psi_-(\mathbf{r}_1,\mathbf{r}_2)\right\rangle \tag{1.8}$$

Under particle exchange, the dipole moment changes sign. Since the transition probability cannot depend on the labeling of the electrons, the dipole moment must be zero, as is the transition probability. Therefore, the electronic transitions can only occur between states with similar spatial symmetry.

The overall wavefunction Ψ of a two-electron system is composed of a spatial wavefunction ψ and a spin wavefunction σ. According to Pauli's principle, which states that the wavefunction of a system of electrons must be antisymmetric with respect to interchange of any two electrons, the two components of the total wavefunction must have opposite symmetry

$$\Psi = \psi_{+}\sigma_{-} \tag{1.9}$$

or

$$\Psi = \psi_{-}\sigma_{+} \tag{1.10}$$

Since the electronic transitions from the initial state Ψ_1 to the final state Ψ_2, both of which must have similar spatial symmetry, the spin components of the initial and final states must also have similar symmetry, i.e., the only allowed electronic transition are triplet$\rightarrow$triplet and singlet$\rightarrow$singlet.

1.3.1. Charge transport in organic semiconductors

The main concerns with charge transport in organic semiconductors are the magnitude of charge mobility and the mechanism of the carrier transport. The charge mobility μ is

defined as the ratio between the velocity of charge carriers, v, and the strength of electric field, F:

$$\mu = \frac{v}{F} \tag{1.11}$$

Normally, the mobility of amorphous organic materials is in the range of 10^{-5} – 10^{-1} cm^2/Vs. Organic crystals can reach a mobility of 10 cm^2/Vs, as compared to the range for inorganic single crystal silicon, which is 10^2 – 10^3 cm^2/Vs .

1.3.1.1. Experimental measurements of carrier mobilities

Charge mobilities can be determined by various experimental methods such as time-of-flight (TOF),[45] space-charge-limited current (SCLC), drain current of an organic field-effect transistor (OFET),[46] and pulse-radiolysis time-resolved microwave conductivity (PR-TRMC).[47] The factors affecting the measurement results include the chosen method and the purity and morphology of the materials.[48]

Time-of-Flight (TOF)

For TOF measurements, a thin film of the organic semiconductor of around 10 μm is sandwiched between two electrodes of which at least one is transparent. A laser beam is used to excite the material to generate charges near the transparent electrode. The photo-generated holes or electrons will drift to the opposite electrode depending on the polarity of the applied bias. The photocurrent is recorded as a function of time. An obvious cusp is obtained in the case of a nondispersive photocurrent. This cusp denotes the transient time (τ) for the charges migrating across the film. For a dispersive photocurrent, due to

lack of a sharp cusp, τ is determined from the double logarithmic plots of the photocurrent vs. time, according to the Scher-Montroll theory.[49]

The mobility of holes or electrons is:

$$\mu = \frac{v}{F} = \frac{d}{F\tau} = \frac{d^2}{V\tau} \tag{1.12}$$

where d is the thickness of the organic film and V is the applied voltage.

To ensure the accuracy of τ from the transient photocurrent, the instantaneously photo-generated charges should be in a thin sheet with thickness far less than the distance between the electrodes. Normally the organic materials having large absorption coefficient can absorb most of the incident light in less than a few hundred nanometers. In case that the absorption of the organic material is not strong enough in the available excitation wavelength, a suitable thin charge carrier generation layer (CGL) can be incorporated between the transparent electrode and the organic layer. CGL is composed of materials with a large absorption coefficient for optical absorption and pohto-carrier generation.[50]

Space-charge-limited current (SCLC)

To measure the SCLC, the organic material is sandwiched between two electrodes to form a diode. The current density – applied voltage (*J–V)* profile is used to determine the mobility of the organic material. Normally the electrodes are chosen to inject only holes or electrons into the organic material at low voltage and have a suitable workfunction to ensure the current is bulk transport limited instead injection limited. The *J–V* profile is

linear at low applied voltage because of ohmic contact. With increasing voltage, the J–V characteristics become space-charge-limited because the electrostatic potential of the injected charges prevents the injection of additional charges.[51] In this regime, the current density is proportional to the square of the electric field:

$$J = \frac{9}{8}\varepsilon\mu\frac{V^2}{d^3}\theta = \frac{9}{8}\varepsilon\mu\frac{1}{d}F^2\theta \tag{1.13}$$

where ε is the permittivity and θ equals to 1 if the organic layer is trap-free. In the present of traps, θ is the ratio of the number of free carriers to the total number of carriers.

Normally the mobility of an organic material is field dependent, in agreement with the Poole-Frenkel effect. In this case, the above equation is modified as:

$$J = \frac{9}{8}\varepsilon\mu_0 \exp(\beta F^{1/2})\frac{1}{d}F^2\theta \tag{1.14}$$

where μ_0 is the mobility at $F = 0$. If the mobility is independent on the electric field, $\beta = 0$.

Drain current of an OFET

To measure the drain current of an OFET, the organic material is situated on the top of an insulator (gate dielectric), which is on top of gate electrode. Two electrodes (source and drain) can be located on top of the organic material (top-contact configuration) or embedded in the organic material (bottom-contact configuration). The current from the source electrode to the drain electrode (I_{SD}) under a given gate voltage (V_G) increases linearly with the increasing source/drain voltage (V_{SD}) and gradually becomes saturated.

The charge mobility can be extracted from the electrical characteristics of the field-effect transistors using organic materials as active layers, either from the linear region or the saturated region:

$$\mu = \frac{LI_{\mathrm{SD,linear}}}{CW\left(V_{\mathrm{G}} - V_{\mathrm{T}}\right)V_{\mathrm{SD}}} \tag{1.15}$$

$$\mu = \frac{2LI_{\mathrm{SD,sat}}}{CW\left(V_{\mathrm{G}} - V_{\mathrm{T}}\right)^2} \tag{1.16}$$

Here, C is the capacitance of the gate dielectric, W and L are the width and the length of the conducting channel, and V_{T} is the threshold voltage. Charge migration occurs within the interfaces between the organic material and the dielectric (bottom-contact) or with the air (top-contact).[52,53] The surface morphology, polarity of the dielectric, and the presence of traps in the interfaces affects the performances of the OFETs.

Pulse-radiolysis time-resolved microwave conductivity (PR-TRMC)

For PR-TRMC measurements, the sample can be in bulk form or as single polymer chains in solution. The conductivity of the sample changes when a pulse of highly energetic electrons in the MeV range excites the sample. The change in conductivity $\Delta\sigma$ can be measured via the change in microwave power reflected by the sample:[54]

$$\Delta\sigma = eN_{\mathrm{e-h}}\sum\mu, \tag{1.17}$$

where e is elementary charge, $N_{\mathrm{e\text{-}h}}$ is the density of generated electron-hole pairs and $\Sigma\mu$ is the sum of hole and electron mobilities. PR-TRMC is a contact-free technique that is

not affected by space-charge effects. The charges are directly generated in the bulk. The transport properties are limited on a very local spatial scale and are determined by the frequency of the microwave radiation.

PR-TRMC is different from DC measurements such as TOF, in which charges migrate across the structural defects and interact with the impurities, in that it can provide intrinsic AC transport information for the bulk, in a small spatial dimension. Furthermore the mobility is higher for PR-TRMC when compared to DC measurements. A mobility as high as 600 cm^2/Vs was reported recently from fully planar, ladder-type polyparaphenylene chains in dilute solution.[55] This confirms that the intrachain mobility of conjugated polymers can be as high as or even higher than inorganic semiconductors.

1.3.1.2. Charge transport mechanism in organic semiconductors

Both band and hopping models are used to explain the charge transport mechanism in organic semiconductors. A recent study was done on the transport properties of polyacenes, based on a tight-binding band model with electron-phonon scattering under a constant time approximation. The study showed that the mean free path of charge carriers is comparable or even shorter than the lattice constant at high temperatures. This result indicates that there is a localized transport regime within organic semiconductors.[56] The reason for the failure of band model originates from the weak interaction between organic molecules that are held together by van der Waals forces. A continuous band structure does not always exist in organic semiconductors. Instead, the charge transport mechanism is more accurately described by the hopping model, in which holes and electrons hop between discontinuous localized electronic states.[57] More specifically, for

a disordered organic system, charge transport occurs through sequential redox process between molecules. Electrons are transferred from anions to neutral molecules through the lowest unoccupied molecular orbitals (LUMO) while holes are transferred from cations to neutral molecules through the highest occupied molecular orbitals (HOMO).

$$M_1^{+/-} + M_2 \rightarrow M_1 + M_2^{+/-} \tag{1.18}$$

Two main models for the hopping mechanism are often used in the literature. The first one is expressed by the Miller-Abrahams equation:[58]

$$k_{ij} = f \exp(-2\gamma R_{ij}) \exp(-\frac{\varepsilon_j - \varepsilon_i}{k_B T}), \text{ when } \varepsilon_j > \varepsilon_i \tag{1.19}$$

$$k_{ij} = f \exp(-2\gamma R_{ij}), \text{ when } \varepsilon_j < \varepsilon_i. \tag{1.20}$$

Here, f is the hopping attempt frequency, R_{ij} is the distance between hopping sites i and j, γ is the overlap factor, and ε_i and ε_j are the site energies. The first exponential term originates from the decrease in electronic coupling with increasing distance. The second exponential term is a Boltzmann factor for an upward jump in energy and is equal to 1 for a downward jump in energy. Therefore, there is always a channel to accept the energy difference if there is a downward jump in energy.

The other model for the hopping rate is Marcus electron-transfer theory:[59]

$$k_{et} = \frac{2\pi}{\hbar} \frac{H_{da}^2}{\sqrt{4\pi\lambda kT}} \exp(-\frac{(\Delta G + \lambda)^2}{4\lambda kT}) \tag{1.21}$$

where λ is the reorganization energy, k is Boltzmann's constant, H_{da} is the electronic coupling, ΔG is the free energy change for the electron transfer reaction. The charge transfer integral, H_{da}, is determined by the overlap of the wavefunctions of adjacent molecules, which is in turn determined by the relative spatial overlap and patterns of the wavefunctions.[60] λ is the energy required to reconfigure the molecular structures during the charge transfer (a positive value).[61]

Both of the models consider electronic coupling in the process of charge hopping. If we assume that H_{da} in the Marcus electron-transfer equation is exponentially dependent on hopping distance as $H_{da} = H_{da,0}\exp(-\gamma R_{ij})$, the pre-exponent factors of the equations are similar. The two models consider the energy difference of hopping sites as a driving force. If we neglect the entropy contribution, $\Delta G = \varepsilon_j - \varepsilon_I$, in the hopping process, the assistance of thermal fluctuations is required to ensure energy conservation.

For the Miller-Abrahams model, the carrier hops are assisted by the absorption or emission of a single phonon that compensates for the energy difference $\varepsilon_j - \varepsilon_i$. This model only applies if the energy difference between hopping sites does not exceed the maximum energy (Debye energy) of the phonons effectively coupled to the electron-transfer reaction. Therefore, the Miller-Abrahams model is only valid for weak electron-phonon (vibration) coupling and low temperatures.

On the other hand, Marcus electron-transfer model is valid for large electron-phonon interactions and high temperatures. The model takes the vibration (λ) explicitly into the electron-transfer equation. The hopping rate does not increase monotonically with the

driving force ΔG. For a given λ, the transfer rate first increases with an increasing driving force (ΔG is more negative) until a maximum when $|\Delta G| = \lambda$. When the driving force continues to increase and is larger than λ, that is, $|\Delta G| > \lambda$, the hopping rate decreases. This behavior is totally absent in Miller-Abrahams model.

Since organic molecules possess both intrinsic intermolecular and intramolecular vibrational modes that are much stronger than the usual electron-phonon coupling in inorganic crystals,[62] Marcus' theory is more widely used in organic materials research.

1.3.2. Energy transfer in organic semiconductors

Transfer of electronic excitation energy from one molecule to another involves

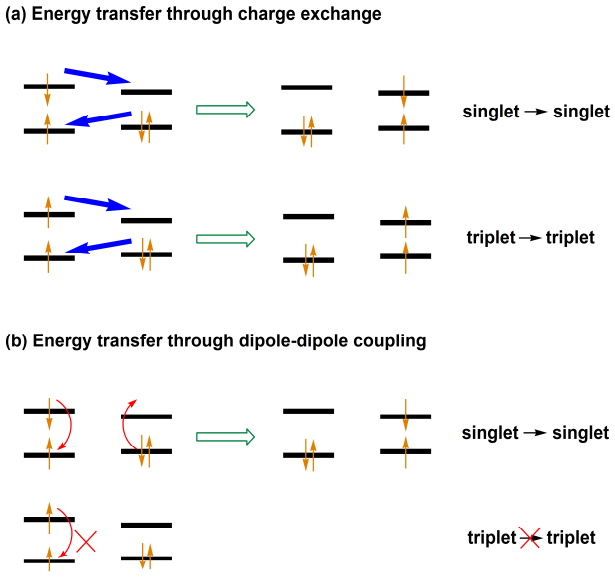

Figure 1.9. Energy transfer mechanism. (a) Energy transfer is mediated by charge exchange. In this mechanism, both singlet and triplet can propagate in organic semiconductors. (b) Energy transfer via dipole-dipole coupling. Due to spin restriction, only singlet can propagate in organic semiconductors through dipole-dipole coupling.

different electronic states and may occur via various mechanisms. Two commonly discussed energy exchange mechanisms are charge exchange interaction, and dipole-dipole coupling (Figure 1.9).

The mechanism of the former relates to the physical transfer of an exciton from a donor site to an acceptor site at a rate proportional to the electronic coupling between the donor and acceptor molecules. Since the electronic coupling between two molecules attenuates exponentially with distance, this transfer is a short-range process (~10Å). By this mechanism, both singlet $\rightarrow$ singlet and triplet $\rightarrow$ triplet can hop from donor to acceptor, as illustrated in Figure 1.9. However, no hopping between singlet and triplet states is allowed due to spin conservation.

The energy transfer mechanism of dipole-dipole coupling is called Förster energy transfer, as it was first recognized by Förster. If the emission spectrum of the donor molecule overlaps with the absorption spectrum of the acceptor molecule, then rapid, long range (< 100Å) energy transfer may occur without the emission of a photon.

Following Dexter's approach,[63] the energy transfer rate from donor to acceptor is:

$$k_{da} = \frac{2\pi}{\hbar}\left|\left\langle \Psi_I^* \middle| H \middle| \Psi_F \right\rangle\right|^2 \rho(E) \tag{1.22}$$

where Ψ_I^* is the initial state composed of excited donor and ground state acceptor, and Ψ_F is the final state composed of ground state donor and excited acceptor, and ρ is the density of states. H is the dipole-dipole interaction given by:

$$H(R) = \frac{e^2}{4\pi\varepsilon_r\varepsilon_0 R^3}\left[\mathbf{r}_d \cdot \mathbf{r}_a - 3(\mathbf{r}_d \cdot \mathbf{R})(\mathbf{r}_a \cdot \mathbf{R})/R^2\right] \tag{1.23}$$

where ε_r and ε_0 are the relative dielectric constant and the permittivity of free space, $\mathbf{r}_d$ and $\mathbf{r}_a$ are the vector of the donor and acceptor, $\mathbf{R}$ is the separation between donor and acceptor. H can be expressed in terms of dipole moment operator:

$$H(R) = \frac{1}{4\pi\varepsilon_r\varepsilon_0 R^3}\left|\mu_d \cdot \mu_a - 3(\mu_d \cdot \hat{\mathbf{R}})(\mu_a \cdot \hat{\mathbf{R}})\right| \tag{1.24}$$

where μ_d and μ_a are the respective electric dipole moment operators on the donor and acceptor molecules, and $\hat{\mathbf{R}}$ is the unit vector between the donor and acceptor molecules.

Averaging over all possible orientations of $\mathbf{R}$ yields:

$$\left\langle\left|\mu_d \cdot \mu_a - 3(\mu_d \cdot \hat{\mathbf{R}})(\mu_a \cdot \hat{\mathbf{R}})\right|^2\right\rangle = \frac{2}{3}\left|\langle\mu_d\rangle\right|^2\left|\langle\mu_a\rangle\right|^2 \tag{1.25}$$

Therefore,

$$k_{da} = \frac{1}{12\pi\hbar\varepsilon_r^2\varepsilon_0^2 R^6}\int dE \int \rho_a(\omega_a)\left|\langle\psi_a|\mu_a|\psi_a^*\rangle\right|^2 d\omega_a \int \rho_a(\omega_a)\left|\langle\psi_d^*|\mu_d|\psi_d\rangle\right|^2 d\omega_d \tag{1.26}$$

where ψ_a and ψ_a^* are the ground state and excited acceptors, ψ_d and ψ_d^* are the ground state and excited donors.

The emission spectra of the donor and absorption spectra of the acceptor molecules are:

$$A(E) = \frac{n_d^3 E^3}{3\pi\varepsilon_0^2\hbar^4 c^3}\int \rho_a(\omega_a)\left|\langle\psi_d^*|\mu_d|\psi_d\rangle\right|^2 d\omega_d \tag{1.27}$$

$$\alpha(E) = \frac{n(\nu) n_a E}{6\varepsilon_0 \hbar^2 c} \int \rho_a(\omega_a) \left| \langle \psi_a | \mu_a | \psi_a^* \rangle \right|^2 d\omega_a \tag{1.28}$$

where $A(E)$ is the coefficient of spontaneous emission of the donor at energy E, $\alpha(E)$ is the absorption coefficient of the acceptor, and $n(\nu)$ is the number density of acceptor molecules to absorb light in the frequency range of ν to ν+dν. n_d and n_a are the refractive indices of the mediums for the donor and acceptor molecules. By combining these terms the energy transfer rate becomes:

$$k_{da} = \frac{3\hbar^4 c^4 n_d^3 n_a}{4\pi\varepsilon_r^2 R^6} \int \frac{\alpha(E) A(E)}{E^4 n(E)} dE \tag{1.29}$$

The rate can be further written in terms of the normalized donor emission spectrum $f_d(E)$ and the normalized acceptor absorption spectrum $F_a(E)$:

$$k_{da} = \frac{3\hbar^4 c^4 n_d^3 n_a}{4\pi\varepsilon_r^2 R^6} \frac{\alpha_a}{N_a} \frac{1}{\tau_d} \int \frac{f_d(E) F_a(E)}{E^4} dE \tag{1.30}$$

where α_a is the total absorption coefficient of the acceptor (m^{-1}), N_a is the number density of acceptor molecules (m^{-3}), and $\tau_d = 1/A$ is the fluorescence life time of the donor in the absence of the acceptor.

In a system where the donor molecules are doped with a low-concentration of acceptor molecules, the transfer rate of excitation energy is:

$$k_{da} = \frac{9(\ln 10)\kappa^2 Q_d}{128\pi^5 n_d^4 N \tau_d R^6} \frac{\int f_d(\lambda) F_a(\lambda) \lambda^4 d\lambda}{\int f_d(\lambda) d\lambda} \tag{1.31}$$

Here κ^2 is the orientation factor for dipole-dipole interaction, which is equal to 2/3 if the donor and acceptor molecules are isotropically oriented. Q_d is the fluorescence quantum yield of the donor in the absence of the acceptor. N is Avogadro's number. $f_d(\lambda)$ is the fluorescence intensity of the donor in the absence of the acceptor at wavelength λ. $F_a(\lambda)$ is the molar absorption coefficient of the acceptor at wavelength λ.

Obviously, the energy transfer rate depends on the distance of the donor-acceptor pair, the angle between the donor and acceptor dipoles, and the overlap of the emission spectrum of the donor, and absorption spectrum of the acceptor.

An alternative expression of the transfer rate is given by:

$$k_{da} = \frac{1}{\tau_d}(\frac{R_0}{R})^6, \tag{1.32}$$

where

$$R_0^6 = \frac{9(\ln 10)\kappa^2 Q_d}{128\pi^5 n_d^4 N} \frac{\int f_d(\lambda)F_a(\lambda)\lambda^4 d\lambda}{\int f_d(\lambda)d\lambda} \tag{1.33}$$

If only fluorescence emission and energy transfer deactivate the excited donor molecules, the efficiency of energy transfer from donor to acceptor molecules is:

$$\eta = \frac{k_{da}}{k_{da} + 1/\tau_d} = \frac{1}{1 + (R/R_0)^6} \tag{1.34}$$

R_0 is also called the Förster critical distance because 50% of the excitation energy will be transferred from donor to acceptor for $R = R_0$. Because of the R^6 in the denominator, the energy transfer is almost complete when $R < R_0$.

1.4. Principles and operation of organic semiconductor devices

1.4.1. Organic light-emitting diodes

OLEDs are current-driven devices that convert electrical energy to photons by electronically exciting the organic molecules and allowing them to undergo radiative

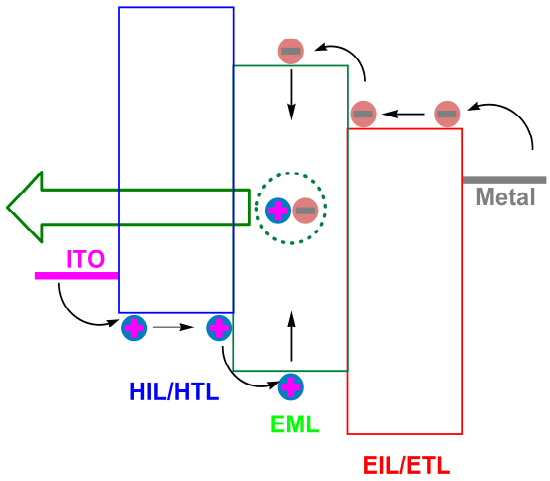

Figure 1.10. Mechanism of organic light-emitting diodes. HIL/HTL: hole injection/transport layer; EML: emitting layer; EIL/ETL: electron injection/transporting layer. HIL/HTL are organic materials have electron-donating characteristic such as polyphenylamines. EIL/ETL are electron-withdrawing materials such as Alq_3. EML are normally highly efficient fluorescent or phosphorescent materials. The electron process involved in the operation of OLEDs are charge injection, transport, and recombination to form excitons, followed by radiative decay of excitons to give photons. Only part of the photons can escape the devices from the forward direction for practical use while the others are absorbed by the organics or waveguided in substrate.

decay. The basic device configuration for OLEDs is for an emitting organic layer to be sandwiched by a transparent electrode (e.g., ITO) and a reflective electrode. Holes and electrons are injected from anode and cathode and transported in the organic layer until they recombine to form excitons. Only some of the excitons can decay radiatively to emit photons. Some of the emitted photons will be absorbed by the organics, some will escape using the substrate as a waveguide, and only a small part will emit from the forward surface.

The external quantum efficiency (EQE) is defined as the ratio of the number of photons detected from the forward direction to the number of the charge carriers injected into the diode. From the definition of EQE and the mechanism described above, EQE can be expressed as:

$$\mathrm{EQE} = \gamma\chi\eta_{pl}\eta_{oc} \tag{1.35}$$

where γ is the probability of exciton formation from injected carriers. Ideally, holes and electrons are fully balanced and completely recombined to form excitons. In this case $\gamma = 1$. γ is normally less than 1 due to the imbalance of holes and electrons in the diode. This imbalance leads to incomplete recombination. Optimizing device configuration and carrier injection/transportation layers can improve γ. χ is the fraction of excitons that have the potential to radiatively decay due to selection criteria for electronic transitions in organic semiconductors. η_{pl} is the photoluminescence (PL) efficiency. η_{oc} is the light out-coupling factor, which is the ratio of the number of photons that escape from the device to the overall number of photons generated. η_{oc} is about 20 ± 2%, which can be

calculated from $\eta_{oc} = 1 - \sqrt{1 - \frac{1}{n^2}}$,[64] where n is the refractive index of the emitting layer (normally n = 1.7±0.1 for organic solids), for flat glass substrates. η_{pl} is referred as intrinsic photoluminescence (PL) efficiency, assuming that the decay mechanism of the electrically generated excitons is the same as for the optically generated excitons. PL efficiency can be measured directly using an integrating sphere.

To enhance the electroluminescence (EL) efficiency, it is necessary to optimize all four factors. First, we need to achieve efficient charge injection from electrodes for both holes and electrons at low voltage to create a good charge balance. To do this, we need to add extra organic layers, with suitable HOMO and LUMO energy levels, for charge injection and transport between the emitting layer and the electrodes. Confinement of the injected charges in the emitting layer to increase the recombination probability is also required for higher γ. Therefore, hole and electron-blocking layers are necessary to prevent the charges from escaping to the adjacent layers. Secondly, χ depends on the emitting materials of OLEDs, either phosphorescent dyes or fluorescent dyes. The former exploit both triplet and singlet excitons, while the latter can only utilize singlet excitons to convert electrical energy to light.[65] According to classical degeneracy statistics, the probability of generating triplet excitons from recombination of injected carriers is 75%, while it is 25% for singlet excitons, assuming the formation cross-sections for triplet and singlet are equal.[66] Therefore, χ for POLEDs is 100% while it is 25% for FOLEDs. Recent progress in experiments[67,68] and theory[69,70] suggest that singlet generation probability for conjugated systems can be larger than 25%. However, the determination of the singlet generation fraction is still heavily debated because it is not easily measured

directly.[71-74] In Chapter 4, further discussion about χ will be presented based on simulation and experimental results. Third, to obtain large PL efficiency, one needs to avoid bimolecular quenching.[75-77] To reduce bimolecular quenching, molecular structures can be engineered to carry large steric groups to prevent the aggregation of emitting molecules.[78] One can also dope host materials with the emitting molecules, in order to separate the emitting molecules from each other. Fourth, the out-coupling factor depends on the structure and optical properties of the organic layers, electrodes and substrate. Using high-refractive-index glass substrates and index-matched glass half-spheres can enhance the EQE by a factor of 2.4.[29]

The EQE can be calculated from current density – voltage – luminescence data and EL spectrum, assuming Lambertian distribution of the EL emission:

$$\mathrm{EQE} = \frac{\pi L \int F(\lambda) d\lambda}{hcK_m \int \frac{F(\lambda)}{\lambda} y(\lambda) d\lambda} \div \frac{J}{e} \tag{1.36}$$

where L is the measured luminance from forward direction, J is the current density, K_m is the maximum luminous efficacy (namely 680 lm/W), $y(\lambda)$ is the normalized photopic spectral response function, $F(\lambda)$ is the EL spectrum of the device, and λ is the wavelength.

1.4.2. Organic solar cells

Organic solar cells convert the energy of sunlight into electrical energy directly by optically exciting the organic molecules to generate excitons. The excitons then disassociate into free charge carriers that are collected by the electrodes and flow through

the external circuit. The performance of a solar cell is evaluated by its power conversion efficiency (η) and its fill factor (*FF*), as defined:

$$\eta = \frac{(VJ)_{\max}}{P_{in}} \tag{1.37}$$

$$FF = \frac{(VJ)_{\max}}{V_{OC} J_{SC}} \tag{1.38}$$

where P_{in}, V_{OC}, J_{SC} are the incident light power, the open circuit voltage, and the short-circuit current density, respectively (Figure 1.11).

The mechanism of *pn*-heterojunction (including bulk heterojunction) organic solar cells is the opposite to that of OLEDs. The incident light is absorbed by organic semiconductors to form excitons. The excitons then diffuse to the organic-organic interfaces. Next, the excitons separate into electrons and holes. The electrons and holes are then transported through the organic materials, and finally the electrons and holes are collected by electrodes.

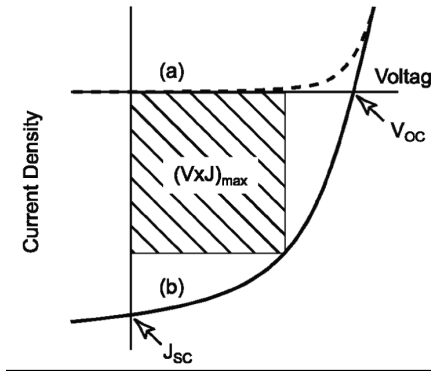

Figure 1.11. Schematic *J-V* cure of OPVs: (a) in dark (b) under illumination.

1.4.3. Organic transistors

OFETs consist of three electrodes (source, drain, gate), an insulator (gate dielectric), and an organic semiconductor as the active material. Normally there are two types of electrode configurations for OFETs; top-contact and bottom-contact. Because organic

materials have negligible amounts of free charge, only small currents flow between the source and drain if there is no voltage applied to the gate electrode. This state is referred to as the 'off' state. For a *p*-channel device, a negative voltage is applied to the gate electrode to attract holes in the organic semiconductor layer and to accumulate at the interface with the gate dielectric. Holes can travel from the source to the drain electrodes if a voltage is applied. The transistor is now in the 'on' state. Similarly, application of positive voltage to the gate electrode induces electron transport in the case of *n*-channel devices. The current from source to drain (I_{SD}) can be modulated by both the gate voltage (V_G) and the source/drain voltage (V_{SD}). I_{SD} under a given V_G increases almost linearly with increasing V_{SD} until gradually becoming saturated. I_{SD} is given by:

$$I_{SD} = \frac{CW\mu}{L}\left[(V_G - V_T)V_{SD} - \frac{V_{SD}^2}{2}\right] \tag{1.39}$$

where μ is the field-effect mobility of the charge carrier, L is the channel length, W is the channel width, C is the capacitance of the gate dielectric, and V_T is the threshold voltage.

The charge mobility can be extracted from the electrical characteristics of the field-effect transistors using organic materials as active layers either from the linear region or the saturated region:

$$\mu = \frac{LI_{SD,linear}}{CW(V_G - V_T)V_{SD}} \tag{1.15}$$

$$\mu = \frac{2LI_{SD,sat}}{CW(V_G - V_T)^2} \tag{1.16}$$

Charges migrate within the interfaces between the organic material and the dielectric (bottom-contact) or the air (top-contact).[52,53] The surface morphology, polarity of the dielectric and the presence of traps in the interfaces affects the performance of OFETs.

1.5. Concluding remarks and the arrangement of the thesis

From the discussions above, the electronic processes in OLEDs, organic solar cells and OFETs include; carrier injection and transport, carrier recombination, exciton formation, and exciton decay or separation. All of these processes are determined by the electronic properties and optical properties of organic semiconductor materials. Novel organic semiconductors with suitable properties for targeted applications are in great demand to boost the performances of organic electronic devices.

One of the advantages of organic semiconductors over inorganic semiconductors is the tunability of electronic properties by modifying chemical structures. Ideal organic semiconductors should have suitable optical and electronic properties for specific applications. Tuning the electronic properties of organic semiconductors is very important. For example, emitting materials with different band gaps are required for multi-color electroluminescent in OLEDs. Suitable energy positions of HOMO and LUMO are necessary to assist charge separation in organic solar cells. Molecules with small charge transfer activation energies are vital for OFETs with high carrier mobility.

Due to the complexity of organic molecules, organic synthesis possesses enormous flexibility. Through manipulation and modification of chemical structures, we can achieve the desired electronic properties. On the one hand this is fortunate, as it provides

virtually endless possibilities for molecular design. On the other hand, it poses the challenge of multi-variable searches. Without efficient molecular design, the process to achieve desired properties is labor intensive, because much trial synthesis and laboratory characterization is required. Hence, in order to obtain basic knowledge about the possible properties of the structures of interest, a reasonable approach is to first carry out theoretical calculations on the structures. Therefore, we used computational methods to tune the electronic properties of organic materials.

In this thesis, the contents are arranged as following. First, polyhedral oligomeric silsesquioxanes (POSS), a nanoscale building block, is used as an illustration for tuning the electronic properties including energy level of frontier orbitals, energy bandgap, reorganization energy, and exciton binding energy. Second, based on the insights obtained from the study on POSS, a rational design of a hybrid organic-inorganic hybrid dipentacene POSS molecule is demonstrated for high charge mobility. A multiscale model based on quantum mechanics, molecular dynamics and kinetic Monte Carlo is established and used to investigate charge transport in this hybrid material. Third, using the insights obtained from the study of POSS and the charge transport model, we designed highly efficient blue fluorescent materials for OLEDs. Finally, the research presented in this thesis is summarized and possible extension of the work is discussed.

1.6. References

(1) Tang, C. W.; VanSlyke, S. A. *Appl. Phys. Lett.* **1987**, *51*, 913-915.

(2) Burroughes, J. H.; Bradley, D. D. C.; Brown, A. R.; Marks, R. N.; MacKay, K.; Friend, R. H.; Burns, P. L.; Holmes, A. B. *Nature* **1990**, *347*, 539-541.

(3) Tang, C. W. *Appl. Phys. Lett.* **1986**, *48*, 183-185.

(4) Kim, J. Y.; Lee, K.; Coates, N. E.; Moses, D.; Nguyen, T. Q.; Dante, M.; Heeger, A. J. *Science* **2007**, *317*, 222-225.

(5) Stutzmann, N.; Friend, R. H.; Sirringhaus, H. *Science* **2003**, *299*, 1881-1884.

(6) Facchetti, A.; Mushrush, M.; Yoon, M. H.; Hutchison, G. R.; Ratner, M. A.; Marks, T. J. *J. Am. Chem. Soc.* **2004**, *126*, 13859-13874.

(7) Forrest, S. R.; Thompson, M. E. *Chem. Rev.* **2007**, *107*, 923-925.

(8) Walzer, K.; Maennig, B.; Pfeiffer, M.; Leo, K. *Chem. Rev.* **2007**, *107*, 1233-1271.

(9) Slaoui, A.; Collins, R. T. *MRS Bull.* **2007**, *32*, 211-218.

(10) Gregg, B. A. *J. Phys. Chem. B* **2003**, *107*, 4688-4698.

(11) Scholes, G. D.; Rumbles, G. *Nat. Mater.* **2006**, *5*, 683-696.

(12) *The Nobel Prize in Chemistry, 2000: Conductive polymers.*

(13) McNeill, R.; Weiss, D. E.; Wardlaw, J. H.; Siudak, R. *Aust. J. Chem.* **1963**, *16*, 1056-&.

(14) Bolto, B. A.; Weiss, D. E. *Aust. J. Chem.* **1963**, *16*, 1076-&.

(15) Bolto, B. A.; McNeill, R.; Weiss, D. E. *Aust. J. Chem.* **1963**, *16*, 1090-&.

(16) Shirakawa, H.; Louis, E. J.; MacDiarmid, A. G.; Chiang, C. K.; Heeger, A. J. *J. Chem. Soc., Chem. Commun*. **1977**, 578-580.

(17) Chiang, C. K.; Fincher, C. R.; Park, Y. W.; Heeger, A. J.; Shirakawa, H.; Louis, E. J.; Gau, S. C.; MacDiarmid, A. G. *Phys. Rev. Lett.* **1977**, *39*, 1098-1101.

(18) Tang, C. W.; Vanslyke, S. A.; Chen, C. H. *J. Appl. Phys*. **1989**, *65*, 3610-3616.

(19) Baldo, M. A.; O'Brien, D. F.; You, Y.; Shoustikov, A.; Sibley, S.; Thompson, M. E.; Forrest, S. R. *Nature* **1998**, *395*, 151-154.

(20) Adachi, C.; Baldo, M. A.; Thompson, M. E.; Forrest, S. R. *J. Appl. Phys*. **2001**, *90*, 5048-5051.

(21) Ogura, T.; Yamashita, T.; Yoshida, M.; Nakajima, S. *Sharp Tech. J* **1992**, 15-18.

(22) Liu, Y.; Nishiura, M.; Wang, Y.; Hou, Z. M. *J. Am. Chem. Soc.* **2006**, *128*, 5592-5593.

(23) Furuta, P. T.; Deng, L.; Garon, S.; Thompson, M. E.; Frechet, J. M. J. *J. Am. Chem. Soc*. **2004**, *126*, 15388-15389.

(24) Kawamura, Y.; Yanagida, S.; Forrest, S. R. *J. Appl. Phys.* **2002**, *92*, 87-93.

(25) Kido, J.; Hongawa, K.; Okuyama, K.; Nagai, K. *Appl. Phys. Lett.* **1994**, *64*, 815-817.

(26) Tokito, S.; Iijima, T.; Tsuzuki, T.; Sato, F. *Appl. Phys. Lett.* **2003**, *83*, 2459-2461.

(27) Xie, Z. Y.; Huang, J. S.; Li, C. N.; Liu, S. Y.; Wang, Y.; Li, Y. Q.; Shen, J. C. *Appl. Phys. Lett.* **1999**, *74*, 641-643.

(28) Sun, Y. R.; Giebink, N. C.; Kanno, H.; Ma, B. W.; Thompson, M. E.; Forrest, S. R. *Nature* **2006**, *440*, 908-912.

(29) Reineke, S.; Lindner, F.; Schwartz, G.; Seidler, N.; Walzer, K.; Lussem, B.; Leo, K. *Nature* **2009**, *459*, 234-U116.

(30) Pochettino, A. *Acad. Lincei Rend.* **1906**, *15*, 355-&.

(31) Bonham, J. S. *Aust. J. Chem.* **1976**, *29*, 2123-2136.

(32) Tnag, C. W.; Albrecht, A. C. *J. Chem. Phys.* **1975**, *62*, 2139-2149.

(33) Kampas, F. J.; Gouterman, M. *J. Phys. Chem.* **1977**, *81*, 690-695.

(34) Merritt, V. Y.; Hovel, H. J. *Appl. Phys. Lett.* **1976**, *29*, 414-415.

(35) Morel, D. L.; Ghosh, A. K.; Feng, T.; Stogryn, E. L.; Purwin, P. E.; Shaw, R. F.; Fishman, C. *Appl. Phys. Lett.* **1978**, *32*, 495-497.

(36) Fan, F. R.; Faulkner, L. R. *J. Chem. Phys.* **1978**, *69*, 3334-3340.

(37) Loutfy, R. O.; Sharp, J. H.; Hsiao, C. K.; Ho, R. *J. Appl. Phys.* **1981**, *52*, 5218-5230.

(38) Yu, G.; Gao, J.; Hummelen, J. C.; Wudl, F.; Heeger, A. J. *Science* **1995**, *270*, 1789-1791.

(39) Park, S. H.; Roy, A.; Beaupre, S.; Cho, S.; Coates, N.; Moon, J. S.; Moses, D.; Leclerc, M.; Lee, K.; Heeger, A. J. *Nat. Photon*. **2009**, *3*, 297-U5.

(40) Burroughes, J. H.; Jones, C. A.; Friend, R. H. *Nature* **1988**, *335*, 137-141.

(41) Garnier, F.; Horowitz, G.; Fichou, D. *Synth. Met.* **1989**, *28*, C705-C714.

(42) Madru, R.; Guillaud, G.; Alsadoun, M.; Maitrot, M.; Andre, J. J.; Simon, J.; Even, R. *Chem. Phys. Lett.* **1988**, *145*, 343-346.

(43) Garnier, F.; Hajlaoui, R.; Yassar, A.; Srivastava, P. *Science* **1994**, *265*, 1684-1686.

(44) Yan, H.; Chen, Z. H.; Zheng, Y.; Newman, C.; Quinn, J. R.; Dotz, F.; Kastler, M.; Facchetti, A. *Nature* **2009**, *457*, 679-U1.

(45) Mort; J. *Photoconductivity and Related Phenomena*; Elsevier: New York, 1976;

(46) Sze; S. M. *Physics of Semiconductor Devices*; Wiley: New York, 1981;

(47) Schouten, P. G.; Warman, J. M.; Dehaas, M. P. *J. Phys. Chem.* **1993**, *97*, 9863-9870.

(48) Shirota, Y.; Kageyama, H. *Chem. Rev.* **2007**, *107*, 953-1010.

(49) Scher, H.; Montroll, E. W. *Phys. Rev. B* **1975**, *12*, 2455-2477.

(50) Borsenberger; P. M.; Weiss; D. S. *Organic Photoreceptors for Imaging Systems*; Marcel Dekker: New York, 1993;

(51) Blom, P. W. M.; deJong, M. J. M.; Vleggaar, J. J. M. *Appl. Phys. Lett.* **1996**, *68*, 3308-3310.

(52) Horowitz, G. *J. Mater. Res.* **2004**, *19*, 1946-1962.

(53) Dodabalapur, A.; Torsi, L.; Katz, H. E. *Science* **1995**, *268*, 270-271.

(54) Warman, J. M.; de Haas, M. P.; Dicker, G.; Grozema, F. C.; Piris, J.; Debije, M. G. *Chem. Mater.* **2004**, *16*, 4600-4609.

(55) Prins, P.; Grozema, F. C.; Schins, J. M.; Savenije, T. J.; Patil, S.; Scherf, U.; Siebbeles, L. D. A. *Phys. Rev. B* **2006**, *73*,

(56) Cheng, Y. C.; Silbey, R. J.; da Silva, D. A.; Calbert, J. P.; Cornil, J.; Bredas, J. L. *J. Chem. Phys.* **2003**, *118*, 3764-3774.

(57) Wang, L. J.; Nan, G. J.; Yang, X. D.; Peng, Q.; Li, Q. K.; Shuai, Z. G. *Chem. Soc. Rev.* **2010**, *39*, 423-434.

(58) Miller, A.; Abrahams, E. *Phys. Rev.* **1960**, *120*, 745-755.

(59) Marcus, R. A.; Sutin, N. *Biochim. Biophys. Acta* **1985**, *811*, 265-322.

(60) Bredas, J. L.; Calbert, J. P.; da Silva, D. A.; Cornil, J. *Proc. Natl. Acad. Sci. U.S.A.* **2002**, *99*, 5804-5809.

(61) Coropceanu, V.; Malagoli, M.; da Silva, D. A.; Gruhn, N. E.; Bill, T. G.; Bredas, J. L. *Phys. Rev. Lett.* **2002**, *89*,

(62) Coropceanu, V.; Cornil, J.; da Silva, D. A.; Olivier, Y.; Silbey, R.; Bredas, J. L. *Chem. Rev.* **2007**, *107*, 926-952.

(63) Dexter, D. L. *J. Chem. Phys.* **1953**, *21*, 836-850.

(64) Saleh; B. E. A.; Teich; M. C. *Fundamentals of Photonics*; Wiley: New York, 1991;

(65) Baldo, M.; Segal, M. *Phys. Stat. Sol. A-appl. Res.* **2004**, *201*, 1205-1214.

(66) Friend, R. H.; Gymer, R. W.; Holmes, A. B.; Burroughes, J. H.; Marks, R. N.; Taliani, C.; Bradley, D. D. C.; Dos Santos, D. A.; Bredas, J. L.; Logdlund, M.; Salaneck, W. R. *Nature* **1999**, *397*, 121-128.

(67) Cao, Y.; Parker, I. D.; Yu, G.; Zhang, C.; Heeger, A. J. *Nature* **1999**, *397*, 414-417.

(68) Wohlgenannt, M.; Tandon, K.; Mazumdar, S.; Ramasesha, S.; Vardeny, Z. V. *Nature* **2001**, *409*, 494-497.

(69) Shuai, Z.; Beljonne, D.; Silbey, R. J.; Bredas, J. L. *Phys. Rev. Lett.* **2000**, *84*, 131-134.

(70) Karabunarliev, S.; Bittner, E. R. *Phys. Rev. Lett.* **2003**, *90*, 057402.

(71) Lee, M. K.; Segal, M.; Soos, Z. G.; Shinar, J.; Baldo, M. A. *Phys. Rev. Lett.* **2005**, *94*, 137403.

(72) Yang, C. G.; Eherenfreund, E.; Vardeny, Z. V. *Phys. Rev. Lett.* **2006**, *96*, 089701.

(73) Segal, M.; Baldo, M. A.; Lee, M. K.; Shinar, J.; Soos, Z. G. *PHYSICAL REVIEW B* **2005**, *71*, 245201.

(74) Yang, C. G.; Ehrenfreund, E.; Wohlgenannt, M.; Vardeny, Z. V. *PHYSICAL REVIEW B* **2007**, *75*, 246201.

(75) Xiao, S.; Nguyen, M.; Gong, X.; Cao, Y.; Wu, H. B.; Moses, D.; Heeger, A. J. *Adv. Funct. Mater.* **2003**, *13*, 25-29.

(76) Wu, W. C.; Yeh, H. C.; Chan, L. H.; Chen, C. T. *Adv. Mater.* **2002**, *14*, 1072.

(77) Aubouy, L.; Gerbier, P.; Guerin, C.; Huby, N.; Hirsch, L.; Vignau, L. *Synth. Met.* **2007**, *157*, 91-97.

(78) Huang, C.; Zhen, C. G.; Su, S. P.; Loh, K. P.; Chen, Z. K. *Org. Lett.* **2005**, *7*, 391-394.

Chapter 2. Tuning the electronic properties of polyhedral oligomeric silsesquioxanes

2.1. Introduction

Today, various types of nanoscale building blocks, such as carbon nanotubes,[1,2] CdS nanowires,[3,4] fullerenes,[5,6] and polyhedral oligomeric silsesquioxanes (POSS) cages[7,8] can be produced reliably with high definition. These building blocks serve as the basis for the molecular engineering of new materials and devices with unique properties and functions.[9] Among these designed materials, derivatives of POSS have been widely used as end-cappers[10,11] or pendant units[12,13] to suppress aggregation in conjugated polymers in order to enhance the performance of organic light-emitting diodes (OLEDs). Recently, Sellinger *et al.* have demonstrated that appropriately functionalized POSS can be directly used in OLEDs as highly efficient emitters and hole-transport materials.[14,15] However, there are some problems regarding the use of POSS derivatives as semiconductors in organic electronics. Foremost, the energy gaps between highest occupied molecular orbital (HOMO) and lowest unoccupied molecular orbital (LUMO) of POSS and its derivatives are normally too large to allow for semiconductor behavior, because the silica core is not a traditional π-conjugated structure. A possible way to tune the energy level of frontier orbitals is by functionalizing the POSS cube with organic groups, thereby creating hybrid organic-inorganic building blocks. The tunability of the energy gap is

essential for multicolor electroluminescence and photovoltaic applications. However, the interactions between the silica core and the functional groups and their effect on the electronic structure of the hybrid molecules are not well understood. Therefore, theoretical studies of POSS compounds to clarify how the functional groups affect the optical or electrical properties of these compounds are important in view of guiding the molecular design and synthesis of new nano-scale building blocks for applications in organic electronics.

First-principles studies of POSS systems are computationally intensive because of the size of the molecules in question. As a first endeavor, we therefore investigate the functionalized derivatives of the most commonly used POSS system, i.e., the cube-shaped $H_8Si_8O_{12}$ (POSS-T8). Density functional theory (DFT) and time-dependent density functional theory (TDDFT)[16,17] were utilized to study the ground and excited electronic states of these molecules to obtain an accurate and computationally economical way of modeling electron correlation.[18,19]

2.2. Molecular Design and Computational Details

In this study, POSS-T8 served as the starting configuration, to which we attached different functional groups in order to tune the frontier orbitals of the POSS compounds, and to achieve organic-inorganic nano-composites with controllable energy gaps, carrier transport properties and exciton binding energies. These functional groups included 4-cyanophenyl (Cy), which generally acts as an electron-withdrawing group, and 4-carbazolephenyl (Car), an electron-donating group. These species were attached to the outside corners of the POSS cube, covalently bonded to silicon, to form Cy-POSS-T8 and

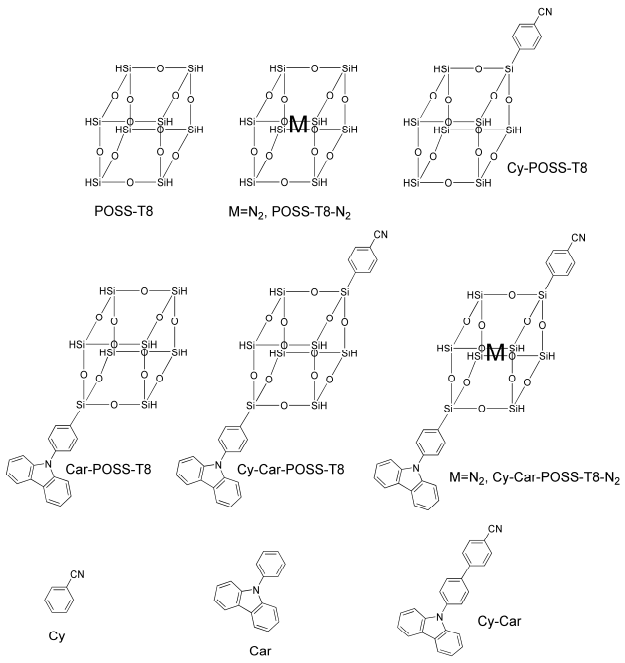

Figure 2.1. Molecular structures of POSS-T8, its derivatives, and the individual organic functional groups. Cyanophenyl (Cy) is electron-withdrawing group while carbazolephenyl (Car) is electron-donating group. The combinations of the these groups and POSS-T8 cage are used to study how the functionalization affect the electronic properties such as energy level of frontier orbitals, reorganization energy, and exciton binding energy.

Car-POSS-T8 molecules, respectively. Furthermore, we inserted a conjugated system, such as a N_2 molecule, into the center of the POSS cube to influence the electronic structures of the cage and to probe the chemical environment inside the cube. We examined the electronic structures of hybrid molecules resulting from various combinations of these species, including POSS-T8-N_2, Cy-POSS-T8, Car-POSS-T8, Cy-Car-POSS-T8, and Cy-Car-POSS-T8-N_2, a configuration with the electron-withdrawing and electron-donating groups attached to the silicon atoms on opposite sides of the body diagonal with insertion of N_2 inside the cage. The structures of these molecules are shown in Figure 2.1, including the organic counterparts without the cage.

Calculations on the above molecules were performed using Gaussian03.[20] Pre-optimizations of the molecules were carried out using PM3 semi-empirical quantum chemistry model.[21] The resulting molecular configurations were used as the starting

atomic coordinates for further optimization in the DFT framework. We chose B3LYP as the exchange-correlation functional.[22] B3LYP is a Hartree-Fock-DFT hybrid where the exchange energy is explicitly calculated using a Hartree-Fock approach. The molecular geometries were optimized in the Cartesian coordinate system without any symmetry (maximum degrees of freedom) using 6-31G* contracted Gaussian basis set with polarization functions.[23,24] The convergence criteria used in the Berny optimization method[25] required the maximum force, RMS force, maximum displacement, and RMS displacement to be less than 4.5×10^{-4}, 3.0×10^{-4}, 1.8×10^{-3}, 1.2×10^{-3} au, respectively (default values). TDDFT calculations were based on the optimized geometries at the same approximation level, i.e., B3LYP/6-31G*.

2.3. Results and Discussion

2.3.1. Ground State Geometries and Frontier Orbitals

POSS-T8 has been widely investigated experimentally and theoretically. Ample experimental data and first-principles calculation results are available to test the reliability of the methodology used in this work. A comparison of the calculation results from this work and other theoretical results and experimental data is presented in Table 2.1.

The optimized bond lengths and angles are in good agreement with the experimental data and calculation results using other methods. Specifically, the bond length of Si-O and Si-H are slightly longer than the experimental data obtained from X-ray diffraction and neutron diffraction. The reason may be that in our calculations, the molecule is

relaxed in vacuum, whereas the experimental data are obtained for the condensed solid state. Differences of bond lengths of Si-O between our calculations and the experimental data are all less than 1.5%. For Si-H bonds, the difference is about 1.0% when compared with neutron diffraction results. For the Si-O-Si bond angle, the difference between the calculations and experiment is less than 1.2%, and those for the O-Si-O or O-Si-H angles are negligibly small.

Table 2.1. Selected geometry parameters of POSS-T8

Methods	Bond length(Å)		Angle(°)			Reference
	Si-O	Si-H	Si-O-Si	O-Si-O	O-Si-H	
DFT B3LYP/6-31G*	1.643-1.644	1.465	146.1-149.3	109.5-109.8	109.3-109.4	This work
HF 6-31G(d)	1.630	1.457	149.0	109.0	----	Ref.[26]
DFT B3LYP/ 6-31G**	1.640	1.460	148.2	109.6	109.3	Ref.[27]
X-ray diffraction	1.619	1.450	147.5	109.6	109.5	Ref.[28]
Neutron diffraction	1.623-1.626	1.459-1.463	147.25-147.45	109.14-109.53	109.07-109.77	Ref.[29]

The two nitrogen atoms in POSS-T8-N_2 are located in the center of the cage, and are aligned with a mirror plane containing the two oxygen atoms (Figure 2.2 (A)). The resulting orientation of nitrogen atoms inside the cage is consistent with a previous high-level *ab initio* results.[30] Due to the orientation of N_2 inside the cage, there are two different isomers for Cy-Car-POSS-T8-N_2 (Figure 2.2 (B) and (C)): one where the angle between the line connecting the functionalized silicon atoms and the orientation of nitrogen molecules is 35.3° (Cy-Car-POSS-T8-N_2-Para), the other one where the angle

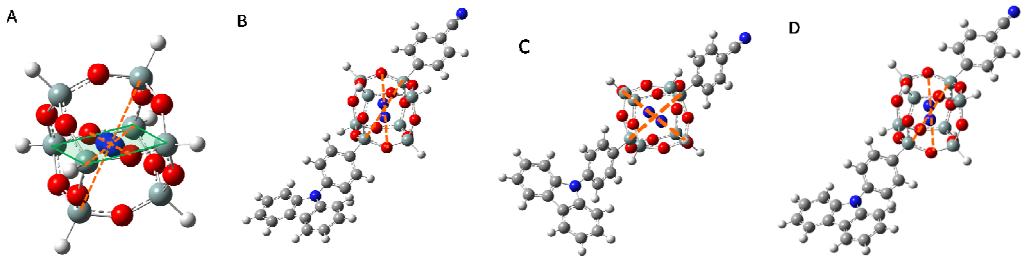

Figure 2.2. (A) Optimized structures of POSS-T8-N_2 (B) Optimized structure of Cy-Car-POSS-T8-N_2-Para. (C) Optimized structure of Cy-Car-POSS-T8-N_2-Perp. C (black), H (white), O (red), N (blue), Si (gray). The two nitrogen atoms in POSS-T8-N_2 are located in the center of the cage, and are aligned with two oxygen atoms in a mirror plane (the green plane) containing the two oxygen atoms. The angle between the line connecting the silicon atoms which are functionalized and the orientation of nitrogen molecules is 35.3° for Cy-Car-POSS-T8-N2-Para and 87.6° for Cy-Car-POSS-T8-N2-Perp.

described is 87.6° (Cy-Car-POSS-T8-N_2-Perp). In the transition state (Figure 2.2 (D)) between the two isomers, the angle is 34.6°. Cy-Car-POSS-T8-N_2-Perp is only 2.36 meV more stable than Cy-Car-POSS-T8-N_2-Para. The energy barrier from Cy-Car-POSS-T8-N_2-Perp to Cy-Car-POSS-T8-N_2-Para is only 2.68 meV, which is much smaller than the thermal energy at room temperature. Therefore, Cy-Car-POSS-T8-N_2 can switch easily between the two isomers at room temperature.

The silica core is found to be quite rigid, as is revealed by comparing the distance between two silicon atoms along body diagonal before and after functionalization. In POSS-T8 this distance is 5.473 Å. In the hybrid molecules, the spacing between the diagonally opposed silicon atoms, to which an organic group is attached in at least one or both cases, are all larger than that in POSS-T8, but the differences are less than 2.7% (Table 2.2). The rigidity of the inorganic core in the derivatives is likely to invoke three-dimensional arrangement of these building blocks in an extended structure. This may

affect the π-π stacking between planar conjugated organic fragments attached to the core in solid state, because the organic groups can only assume limited orientations relative to the cube.

Table 2.2. Distance between the silicon atoms on body diagonal

	POSS-T8	POSS-T8-N_2	Cy-POSS-T8	Car-POSS-T8	Cy-Car-POSS-T8	Cy-Car-POSS-T8-N_2-Para	Cy-Car-POSS-T8-N_2-Perp
Distance (Å)	5.473	5.586 [a] 5.483 [b]	5.481	5.492	5.500	5.623	5.512
Deformation (Å)	----	0.113 [a] 0.01 [b]	0.008	0.019	0.027	0.15	0.039
Deformation (%)	----	2.1 [a] 0.18 [b]	0.15	0.35	0.49	2.7	0.70

[a] for the silicon atoms in the mirror plane. [b] for the silicon atoms out of the mirror plane.

The distance between the two nitrogen atoms inside the cage in POSS-T8-N_2 is 1.0954 Å, which is a little shorter than the bond length of 1.1055 Å in an isolated nitrogen molecule, evaluated in the same approximation level. This implies that the two nitrogen atoms are as strongly bonded to each other as in the free N_2 molecule. The bonded nature of the two nitrogen atoms inside the cage preserves some electronic properties of nitrogen molecule, which will be explained below. In Cy-Car-POSS-T8-N_2-Para and Cy-Car-POSS-T8-N_2-Perp, the distance of the two nitrogen atoms inside the cage is 1.0951 Å and 1.0950 Å, almost the same as in POSS-T8-N_2. The difference in bonding energy of the nitrogen atoms in the two isomers of Cy-Car-POSS-T8-N_2 and POSS-T8-N_2 is as small as 4.6×10^{-4} eV, as calculated from B3LYP/6-31G*.

The spatial arrangement of all the frontier orbitals were determined for the ground state optimized geometries corresponding to the singlet spin state for POSS-T8 and its derivatives. The calculated HOMO-LUMO energies of those molecules are shown in Figure 2.3.

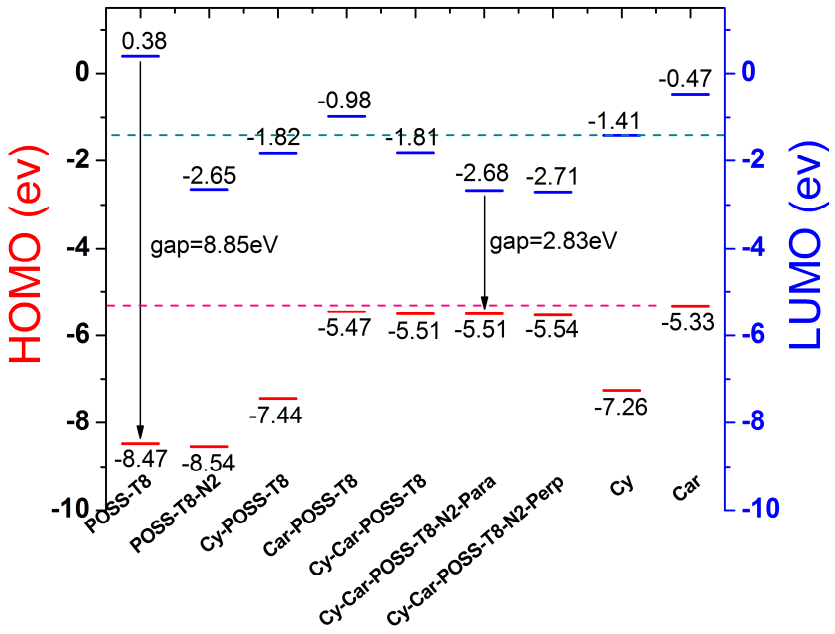

Figure 2.3. Calculated HOMO and LUMO of POSS-T8 and its derivatives at the approximation level of B3LYP/6-31G*. The HOMO LUMO gap reduces from ultraviolet for POSS to visible light for the two isomers of Cy-Car-POSS-T8-N_2. The HOMO of the derivatives have Car group is very similar to that of Car. The HOMO LUMO gap of Cy-POSS-T8 and Car-POSS-T8 are lower than those of Cy and Car, respectively, indicating POSS cage is partially conjugated. The LUMO of Cy-POSS-T8 and Car-POSS-T8 are lower than those of Cy and Car, respectively, indicating the electron-withdrawing characteristic of POSS cage.

The HOMO energy is –8.47 eV and LUMO energy is 0.38 eV for POSS-T8. The HOMO and LUMO gap is 8.85 eV, which well matches the value of 8.0 eV estimated from the absorption spectrum. [33] The HOMO of POSS-T8 originates from the atomic orbitals (AOs) of lone-pair electrons on oxygen atoms, which is also in agreement with the previous reports.[34,35]

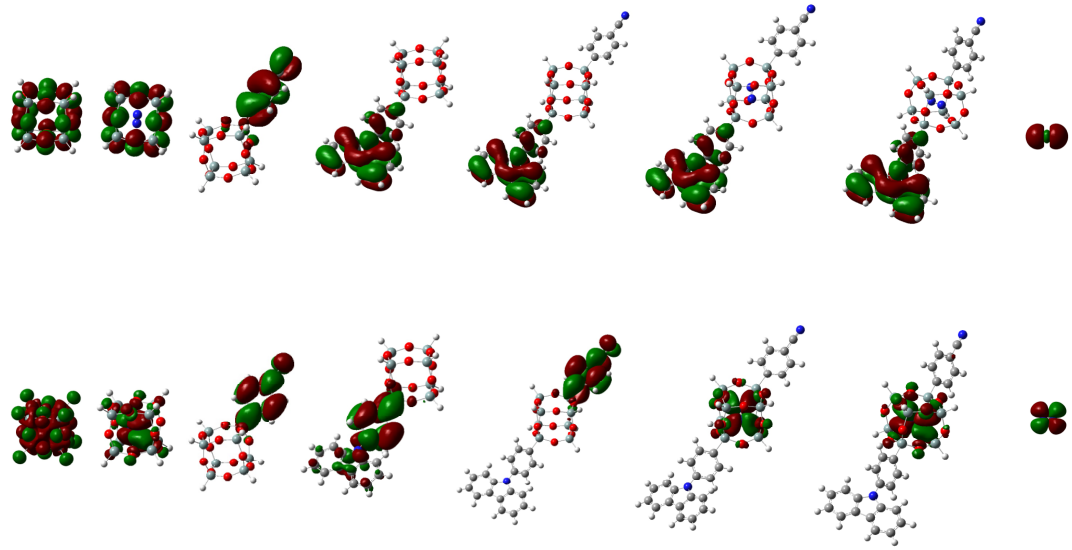

Figure 2.4. Electron density isocontours (0.02 au). Top: HOMO, bottom: LUMO. From left to right: POSS-T8, POSS-T8-N_2, Cy-POSS-T8, Car-POSS-T8, Cy-Car-POSS-T8, Cy-Car-POSS-T8-N_2-Para, Cy-Car-POSS-T8-N_2-Perp, N_2. HOMO of the derivatives with electron donating group all localizes on Car group. LUMO of Cy-POSS-T8 and Cy-Car-POSS-T8 localizes on Cy group but HOMO of the isomers of Cy-Car-POSS-T8-N_2 localizes on the nitrogen molecules, as POSS-T8-N_2.

By comparing the HOMO and LUMO of POSS-T8 and Cy-POSS-T8, we can see that functionalization of one corner of the cage with the 4-cyanophenyl electron-withdrawing group changes the HOMO energy by about 1 eV, from –8.47 eV to –7.44 eV, and changes the LUMO energy more dramatically, from 0.38 eV to –1.82 eV. The electron density of the LUMO of Cy-POSS-T8 is mainly localized on the 4-cyanophenyl group

(Figure 2.4). For Cy-Car-POSS-T8, the value of LUMO is similar to that for Cy-POSS-T8, and the principal contribution remains from cyanophenyl group.

On the other hand, the HOMO can be effectively tuned by the introduction of an electron-donating group. The HOMO energies of Car-POSS-T8, Cy-Car-POSS-T8, and the isomers of Cy-Car-POSS-T8-N_2 are almost the same (~ –5.5 eV). From Figure 2.4, we can see that all these HOMO are localized in the 4-carbazolephenyl electron-donating group, and share a similar electron density surface.

The HOMO of POSS-T8-N_2 is very similar to that of POSS-T8, i.e., the electron density is mostly localized on the oxygen atoms. In contrast, the LUMO of the POSS-T8-N_2 is completely different from that of POSS-T8. In the latter case, the electron density is distributed across all atoms, while the LUMO of POSS-T8-N_2 partially resides on the oxygen atoms, but for the most part resides on the nitrogen atoms inside the cage. By comparing the frontier orbitals of nitrogen molecule and POSS-T8-N_2, it is clear that the LUMO of POSS-T8-N_2 mainly consists of the nitrogen π orbital confined to the inside of the cage. As indicated above, the strong covalent bonding between the two nitrogen atoms causes them to preserve the properties of the individual nitrogen molecule instead of a loosely attached atomic cluster. The value of LUMO of POSS-T8-N_2 is 3.03 eV lower than that of POSS-T8, reducing the HOMO-LUMO gap from 8.85 eV for POSS-T8 to 5.89 eV for POSS-T8-N_2.

If the electron-donating and withdrawing groups are both attached to the cage to form Cy-Car-POSS-T8, the HOMO and LUMO are localized on these two groups, respectively, and the HOMO-LUMO gap reduces to 3.70 eV, which corresponds to the energy of near

violet light. Finally, inserting N_2 inside the cage to form isomers of Cy-Car-POSS-T8-N_2 does not change the HOMO but changes the LUMO to localize mainly on the nitrogen atoms inside the cage, as in the case of POSS-T8-N_2. The HOMO-LUMO gap is further reduced to ~ 2.84 eV, which falls into the range of visible spectrum.

The silsesquioxane cage is normally considered an insulator. Recently, based on experimental results, Sulaiman et al. suggest that the cage core can interact with the conjugation groups attached to the corner electronically.[36] Our calculations directly confirm the above statement by comparing the HOMO and LUMO energy gap of the Cy group taken individually with that of the Cy-POSS-T8 hybrid molecule, or similarly, those of Car and Car-POSS-T8. The HOMO-LUMO gap of Cy-POSS-T8 is lower than that of Cy by 0.23 eV, while the HOMO-LUMO gap of Car-POSS-T8 is, again, lower than that of Car by 0.37 eV. The silica cage in these molecules can therefore not simply be regarded as a non-conjugated moiety. These organic-inorganic skeletons are at least partially conjugated. We also find that the LUMO of Cy-POSS-T8 is lower than that of Cy by 0.41 eV, and the LUMO of Car-POSS-T8 is lower than that of Car by 0.51 eV. The fact that the LUMO energy levels of organic semiconductor groups are more negative as POSS derivatives than by themselves reduces the electron injection barrier, indicating that the silica core serves the role as electron acceptor, consistent with the experimental findings by Feher *et al.*.[37]

2.3.2. Reorganization Energy

Although the unique rigid structures of POSS derivatives may make them good emitters for OLEDs, the organic-inorganic partially conjugated skeleton of these

molecules might not perform well with regard to carrier conductivity, which is essential for organic electronics.

For organic materials, the conductivity mechanism is normally explained by hopping models. As described in Chapter 1, two main models for the hopping mechanism are often used in the literature. One is expressed by the Miller-Abrahams equation and is valid for weak electron-phonon interactions and at low temperature (far below room temperature).[38] The other one is Marcus' theory, which is applicable in the case of large electron-phonon coupling and at higher temperature.[39] Since organic molecules possess intrinsic intermolecular and intramolecular vibrational modes that are much stronger than usual electron-phonon coupling in inorganic crystals,[40] Marcus' theory is more widely used in organic materials research.

Based on Marcus' theory, the conductivity of amorphous organic materials depends on the electron (or hole) transfer reactions between two adjacent molecules (hopping sites), represented by M_1 and M_2

$$M_1^{+/-} + M_2 \rightarrow M_1 + M_2^{+/-}, \tag{2.1}$$

for which the hopping rate can be described by Marcus' electron transfer equation:

$$k_{et} = \frac{2\pi}{\hbar} \frac{H_{da}^2}{\sqrt{4\pi\lambda kT}} \exp(-\frac{(\Delta G + \lambda)^2}{4\lambda kT}), \tag{2.2}$$

where λ is the reorganization energy, k is Boltzmann's constant, H_{da} is the charge-transfer integral, ΔG is the free energy change for the electron transfer reaction, and T is temperature. In the case that the hopping process occurs between identical molecules, ΔG is zero. The charge transfer integral, H_{da}, is determined by the overlap of wavefunction between adjacent molecules, which is determined by the relative spatial overlap and patterns of wavefunction.[41] In amorphous organic semiconductors, molecular packing is random. As a result, the hopping rate in the path of carriers samples a distribution of inter-molecular distances and orbital overlaps and will likely converge towards similar values within a few hops for molecules possess similar structures and electron density. Therefore, within a particular family of molecules, H_{da} can be expected to constitute a less variable quantity than the reorganization energy, which represents the activation barrier originated from the configuration adjustment of molecules during the charge transfer. The reorganization energy λ consists of inner reorganization energy and external polarization due to the solvent effects of the surrounding medium. Here we only consider inner reorganization energy since the external reorganization energy has been

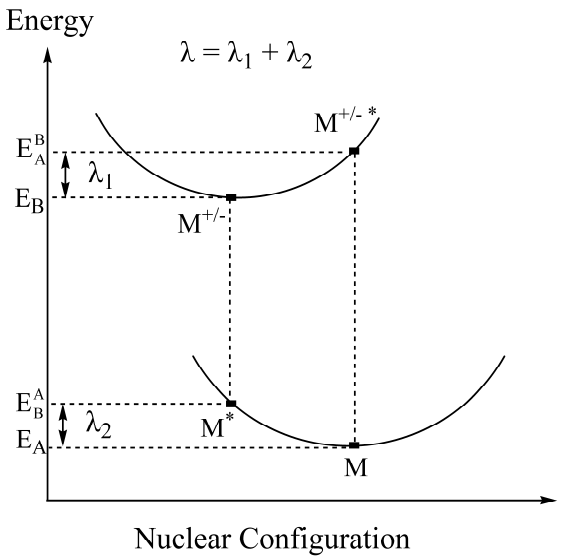

Figure 2.5. Schematic illustration of the configuration adjustment during the self-exchange charge transfer and the calculation of the internal reorganization energy.

demonstrated to be negligible small compared with inner reorganization energy in crystal environment.[42,43] The inner reorganization energies are obtained by comparing the energies in the charged and uncharged optimized configurations, for both the neutral and ionized states, as illustrated in Figure 2.5. Accordingly, $\lambda = E_A^B - E_B + E_B^A - E_A$, where E_A^B is the energy of the ion in the optimized uncharged geometry, E_B is the energy of the ion in the optimized charged geometry, E_B^A is the energy of the neutral molecule in the optimized charged geometry, and E_A is the energy of the neutral molecule in the optimized uncharged geometry.

Since the reorganization energy represents the energy barrier of charge transport induced by the reconfiguration of the molecules, the conductivity of organic

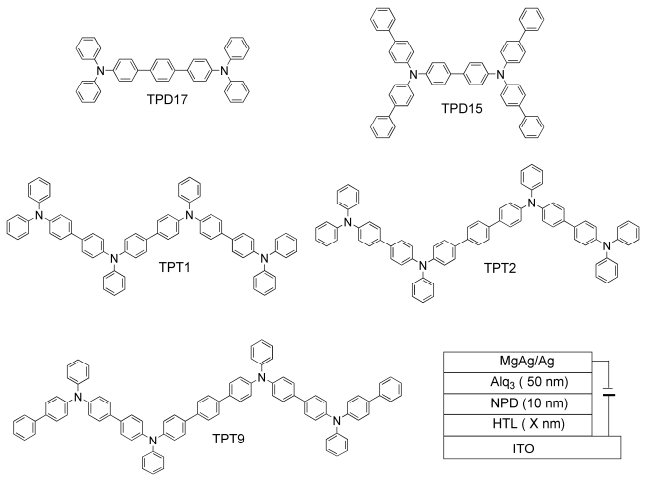

Figure 2.6. Molecular structures of hole transport materials and device configuration. Alq_3 is electron transporting and emitting material. NPD is used to compensate for the interface differences between Alq_3 and HTL materials. X = 50 (thin film) or 300 (thick film). Due to different conductivities of the HTL materials, the increase of driving voltage of device from using thin film to using thick film at constant current of 1 mA/cm^2 varies.

semiconductors is expected to be correlated to λ. Recently, Aonuma *et al.* designed a series of hole transport materials for thick film OLEDs based on polyphenylamines, some of which are shown in Figure 2.6.[44] The driving voltage increases (ΔV) if the HTL thickness changes from 50 nm to 300 nm, while maintaining the current density constant at 1 mA/cm^2. Their results are reproduced in Table 2.3, with ΔV ranging from about 0.4 V to 2 V.

Table 2.3. Driving voltage change due to HTL thickness increasing from 50nm to 300nm while keeping current density at 1mA/cm^2

	TPD17	TPD15	TPT1	TPT2	TPT9
Driving voltage change ΔV(V)	1.85	1.41	0.96	0.60	0.37
Reorganization energy λ(eV)	0.205	0.181	0.158	0.130	0.119

We note that the wavefunction patterns of these polyphenylamines examined here are very similar, with positive and negative lobes of atomic orbitals alternating along the chains of benzene rings (Figure 2.7). In amorphous organic semiconductors, stacking of molecules follows no particular order. Thus, while the degree of wavefunction overlap may vary locally, it can be considered statistically similar across the whole conducting path for the members of this polyphenylamine family. Hence, we expect little variation in the average charge transfer integrals. Based on Marcus electron transfer theory, the conductivity should mainly be determined by the reorganization energy. Indeed, we found that the driving voltage change (ΔV) for these devices increases with the reorganization energy of the HTL materials (Figure 2.8). Smaller reorganization energy corresponds to higher conductivity in these HTL materials. The correlation between ΔV

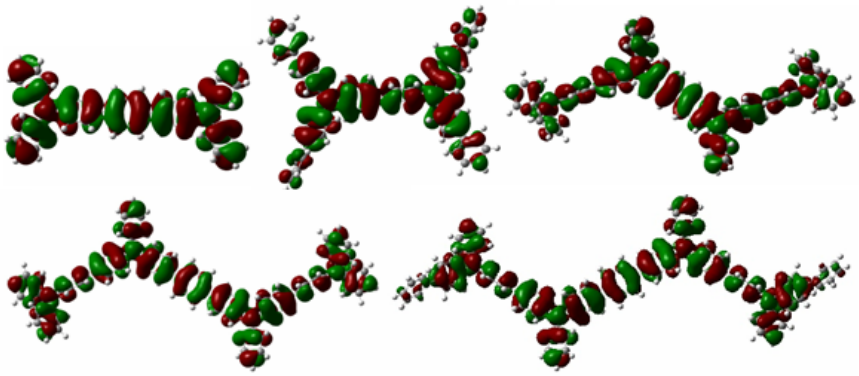

Figure 2.7. Electron density isocontours (0.01 au) of HOMO. Top: TPD17, TPD15, TPT1; bottom: TPT2, TPT9. The wavefunction patterns of these molecules are very similar, with positive and negative lobes of atomic orbitals alternating along the chains of benzene rings.

and λ (calculated at the level of B3LYP 6-31G*/6-31G*) indicates that the reorganization energy can serve as a useful if not determinant screening criterion in selecting organic materials with good conductivity. Keeping this in mind, we will discuss the charge transport properties in terms of reorganization energy of POSS and its derivatives.

To select suitable basis sets for calculating reorganization energies for POSS and the derivatives, we carried out exploratory calculations on Cy and Cy-

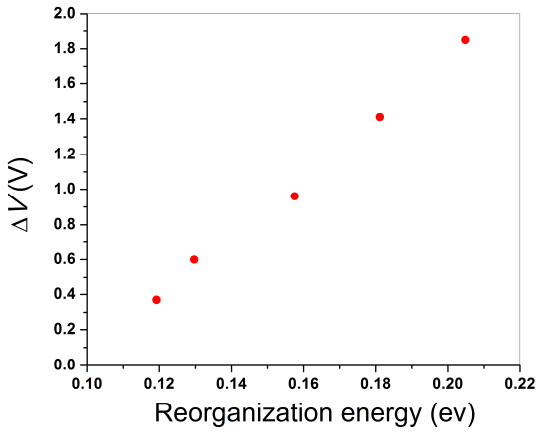

Figure 2.8. Correlation between measured ΔV and calculated λ of HTL materials. Smaller reorganization energy corresponds to higher conductivity in these HTL materials. The reorganization energy can serve as a useful if not determining screening criterion in selecting organic materials with good conductivity

POSS-T8 using various basis sets, and benchmarked the results against those obtained with very large basis sets such as 6-311++G(3df,3pd) for both geometry optimizations and single point energy calculations. (Figure 2.9).

Accordingly, calculations using the 6-31G* basis set for both the geometry optimization and the single point energy calculations yield reorganization energies that

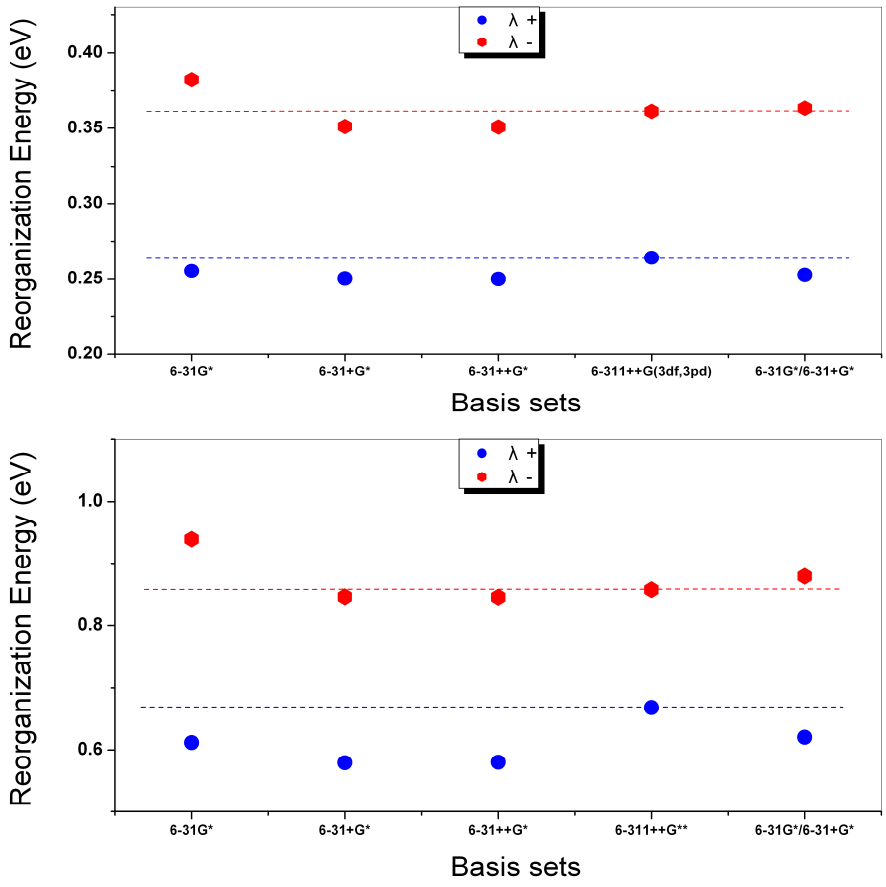

Figure 2.9. Reorganization energies of Cy (up) and Cy-POSS-T8 (down) calculated using different basis sets in B3LYP. 6-31G*/6-31+G* means that single point energy calculations are carried out using the 6-31+G* basis set on the geometry optimized using the 6-31G* basis set. The dashed horizontal lines are indicate the λ_+ and λ_- levels obtained for the 6-311++G(3df,3pd) basis set (for Cy) and 6-311++G** basis set (for Cy-POSS-T8), as a trustworthy reference.

deviate from these reference values by no more than 0.021 eV for Cy and 0.081 eV for Cy-POSS-T8, which is acceptable judged against the spread in the data reported in the current literature. Using the 6-31+G* basis set for single point energy calculations on geometries optimized in the 6-31G* set, reduces the deviations to less than 0.012 eV for Cy and less than 0.048 eV for Cy-POSS-T8. This improvement may be justified weighed against the additional computational cost, but it does not affect the trend in our data. We also use the polarizable continuum solvent model (PCM) with B3LYP/6-31+G* to assess the effect of environment on the reorganization energy of Cy. We found that, λ_+ and λ_- for Cy calculated using the PCM is 0.221 eV and 0.376 eV, compared to 0.253 and 0.363. Embedding the molecule into a polarizable continuum (liquid Cy, dielectric constant = 25.2 [45]) yields results that are not much different from those for the molecule in vacuum. The calculated reorganization energies for electron transfer (λ_-) and for hole transfer (λ_+) are listed in Table 2.4 for both calculation approaches for the molecules in vacuum.

Table 2.4. Reorganization energies of POSS derivatives [a]

	Cy-POSS-T8	Cy	Car-POSS-T8	Car	Cy-Car-POSS-T8	Cy-Car	Cy-Car-POSS-T8-N_2-Para	Cy-Car-POSS-T8-N_2-Perp
λ_-(eV)	0.939 (0.879)	0.383 (0.363	0.829 (0.756)	0.370 (0.256)	0.454 (0.441)	0.515 (0.499)	3.16 (3.04)	2.90 (2.79)
λ_+(eV)	0.612 (0.621)	0.255 (0.253	0.206 (0.204)	0.098 (0.100)	0.208 (0.210)	0.102 (0.104)	0.245 (0.229)	0.213 (0.207)

[a] Data not in parentheses are obtained from single point energy calculations using 6-31G* based on geometries optimized in 6-31G*. Data in parentheses are obtained from single point energy calculations using 6-31+G* based on geometries optimized in 6-31G*.

The data in Table 2.4 reveal the following insights: first, the λ_- values are larger than λ_+ for all compounds. If we only consider the activation energies for carrier hopping and neglect the charge transfer integral, these compounds are expected to be better hole than electron transporters. For compounds with the carbazole moiety, this is consistent with the well-known fact that this molecular group is a good hole transporter. However, it is surprising that even for Cy and Cy-POSS-T8, λ_- values are larger than λ_+, because they are expected to be an electron transporter due to the electron-withdrawing characteristic of the cyanophenyl group. Second, the reorganization energies of the functionalized POSS compounds are generally larger than the corresponding organic groups by themselves, except that λ_- for Cy-Car-POSS-T8 is slightly smaller than that of Cy-Car. This general trend suggests that the energy associated with the silica cage reconfiguration in these molecules during the carrier hopping process may be quite large. Based on the comparison of reorganization energies, these organic-inorganic hybrid composites are not good carrier transporters compared to the organic groups alone, assuming that the difference of the charge transfer integral is negligible.

We are particularly interested in the charge transport properties of the isomers of Cy-Car-POSS-T8-N_2 because of their tremendously large λ_-. Since the HOMO of neutral isomers of Cy-Car-POSS-T8-N_2 is mainly localized on the π orbitals of the nitrogen atoms inside the cage, electrons entering this molecule will prefer to be localized around the nitrogen atoms. This will induce reconfiguration of the nitrogen atoms and the rigid cage around them. Indeed, the distance between the two nitrogen atoms changes from 1.0950 Å to 1.1609 Å. The difference in bonding energy of the nitrogen atoms in the

neutral and negatively charged molecules is 0.20 eV, as calculated using B3LYP/6-31G*. In contrast, the distance between the two nitrogen atoms inside the cage in a positively charged molecule is 1.0950 Å, nearly identical to the value for neutral isomers of Cy-Car-POSS-T8-N_2, where it is 1.0951 Å. (see Appendix A)

Based on Equation (2), if we disregard the difference in charge transfer integrals for electron and hole transport, the relative hopping rate of holes versus electrons of isomers of Cy-Car-POSS-T8-N_2 is about 10^{12}~10^{13}. In fact, the LUMO of Cy-Car-POSS-T8-N_2 isomers is mostly located inside the cage, which hinders the wavefunction overlap of the LUMO of neighboring molecules. This leads to a small charge transfer integral for electron transport compared to that for hole transport. The hole/electron hopping rate ratio is expected to be even larger if charge transfer integrals are considered. Based on our predictions, Cy-Car-POSS-T8-N_2 isomers might be used as electron-blocking materials due to the large electron transfer barrier. Electron and hole blocking materials are widely used in organic light-emitting diodes to enhance the quantum efficiencies.[46,47] Normally, materials with deep HOMO (high ionization potential) can be used as a hole-blocking layer, while materials with high-lying LUMO (low electron affinity) can be used as an electron blocking layer.[48] For these materials, the blocking effects are due to high charge injection barriers. Conversely, Cy-Car-POSS-T8-N_2 isomers would possibly be charge blocking materials whose electron blocking effect was due to charge transport barriers rather than charge injection barrier. Actually, some POSS derivatives with molecules or atom clusters inside the cage have been synthesized recently, reported by the literature.[65] Hence, this new type of charge blocking material is possible to be synthesized and tested in the near future.

2.3.3. Exciton Binding Energy

The exciton binding energy (E_b) is another important quantity that determines the opto-electronic properties in organic materials and devices.[49] It is directly related to the charge separation in organic solar cells and hence, it is an important factor for the efficiency of the cells.[50] It also affects the quantum efficiency of OLEDs[51] because the emissive singlet fraction of excitons in organic light-emitting diodes depends on the exciton binding energy.[52,53] Normally, the intermolecular interactions in amorphous organic solids are not as strong as that in inorganic crystalline semiconductors, so the exciton is Frenkel type (the exciton is localized in a single molecule) in organic materials, while it is Wannier-Mott type in inorganic materials.[54] A recent time-resolved spectroscopy investigation revealed that the primary exciton generated from polycrystalline pentacene is Frenkel type, before this excited state delocalizes to excimers.[55] Hence, calculation from gas phase molecules results in a reasonable approximation for E_b of organic materials.

An exciton can be modeled as a two-electron system: one electron is excited into a higher-energy orbital while leaving a hole in a partially filled lower-energy orbital.[56] Since the exciton binding energy mainly originates from the Coulombic interactions between the electron and hole,[49] the spatial distribution of the density of electrons in the LUMO and that of holes in the HOMO should be decisive. Therefore, a simple way to lower the exciton binding energy is to separate the LUMO and HOMO in space as far as possible. In organic molecules, the HOMO is mainly localized in electron-donating groups and the LUMO in electron-withdrawing groups, as indicated in section **2.3.1**.

Based on the above analysis, the exciton binding energy of Cy-Car-POSS-T8 is expected to be lowest of the POSS derivatives, given that the HOMO and LUMO are well separated (Figure 2.4).

Experimentally determined exciton binding energies for organic semiconductors typically range from 0.1 eV to 1.5 eV, and can vary for the same compound due to variations in experimental conditions reported by different research groups. The estimation of E_b from theory can also be done using different approaches, which has been discussed before.[57] Here, we will start from the common description of the exciton binding energy in which E_b can be taken as the difference between the electronic and optical bandgap energies.[58] For molecules with localized wavefunctions, the electronic bandgap is approximated as energy difference of the HOMO and LUMO, while the optical gap is taken as the first excitation energy.[57] Based on this procedure, the exciton binding energy of PPV has been calculated (at the approximation level of B3LYP/6-31G*) to be 0.35 eV, which is in agreement with experimental data of 0.4 ± 0.1.[59,60]

Today, there are no reliable density functionals available to describe charge transfer systems properly, especially for the properties related to excited states such as excited state geometry, excitation energy and oscillator strength, as pointed out by Wu *et al.*[61] and Magyar *et al.*.[62] B3LYP normally overestimates while BHandHLYP underestimate charge transfer phenomena.[61,62] To select suitable functionals for our donor-acceptor system, the best approach is to compare the calculation results with experiment results. Unfortunately, there are no experimental data available for our donor-acceptor systems until now. But there are some experimental data accessible for N-(4-cyanophenyl)-

carbazole (CBN),[63,64] a compound analogous to Cy-Car. The first absorption band due to charge transfer state of CBN in CH_2Cl_2 is around 3.67 eV.[63,64] Combined with and without polarizable continuum solvent (CH_2Cl_2) model (PCM), the first excitation energy and oscillator strength were calculated and listed in Table 2.5.

Table 2.5. First excitation energy and oscillator strength of CBN calculated using different functionals and basis sets

	B3LYP/ 6-31G*		B3LYP/ 6-31+G*		B3LYP/ 6-311++G**		BHandHLYP/ 6-31G*	
	no PCM	PCM	no PCM	PCM	no PCM	PCM	no PCM	PCM
Excitation energy (eV)	3.52	3.44	3.41	3.34	3.42	3.36	4.41	4.36
Oscillator strength	0.217	0.259	0.186	0.222	0.181	0.208	0.308	0.385

The result is consistent with Wu's findings that the excitation energy is red-shifted using B3LYP while it is blue-shifted using BHandHLYP.[61] However, in the case of CBN, it seems that the performance of B3LYP/6-31G* without PCM is the best when compared with experimental data. And adding diffusion functions does not increase the accuracy when compared with experimental data. The exciton binding energy calculated in vacuum and in CH_2Cl_2 in PCM for CBN is 0.540 eV and 0.580 eV, respectively, not much different from each other. For consistency, we will keep on using B3LYP/6-31G* for our systems. The calculated exciton binding energies of the POSS and POSS derivatives are listed in Table 2.6.

Table 2.6. Exciton binding energy (E_b) of POSS derivatives

2.3.4.	POSS-T8	POSS-T8-N_2	Cy-POSS-T8	Cy	Car-POSS-T8	Car	Cy-Car-POSS-T8	Cy-Car	Cy-Car-POSS-T8-N_2-Para	Cy-Car-POSS-T8-N_2-Perp
E_b (eV)	0.987	1.01	0.611	0.678	0.618	0.643	0.181	0.426	0.305	0.303

The calculated exciton binding energy for Cy-Car-POSS-T8 is much smaller than that for Cy-Car, because the POSS core separates the electron-donating group and the electron-withdrawing group, which are where the HOMO and LUMO localized. We also notice that E_b of the isomers of Cy-Car-POSS-T8-N_2 is larger than Cy-Car-POSS-T8. A possible reason is that the LUMO for the isomers of Cy-Car-POSS-T8-N_2 is localized on the nitrogen atoms inside the POSS cage rather than in the cyanophenyl group. Thus the distance between the HOMO and LUMO orbitals is shortened. It seems that E_b depends on the spatial distribution of HOMO and LUMO rather than on molecular size, since the two molecules in this case have the same spatial extents. To solidify this speculation, we further compared E_b for molecules (I) with different dimensional sizes but similar HOMO and LUMO distributions, and (II) with similar size but different HOMO and LUMO distributions.

For (I), we design the molecules with the cyanophenyl and carbazolephenyl groups attached to the opposite corners of the POSS cube along the body-diagonal, i.e., at a fixed distance, while attaching polyphenyl moieties with different lengths to another pair of diagonally opposed corners of the POSS cube (Figure 2.10). The number of benzene ring

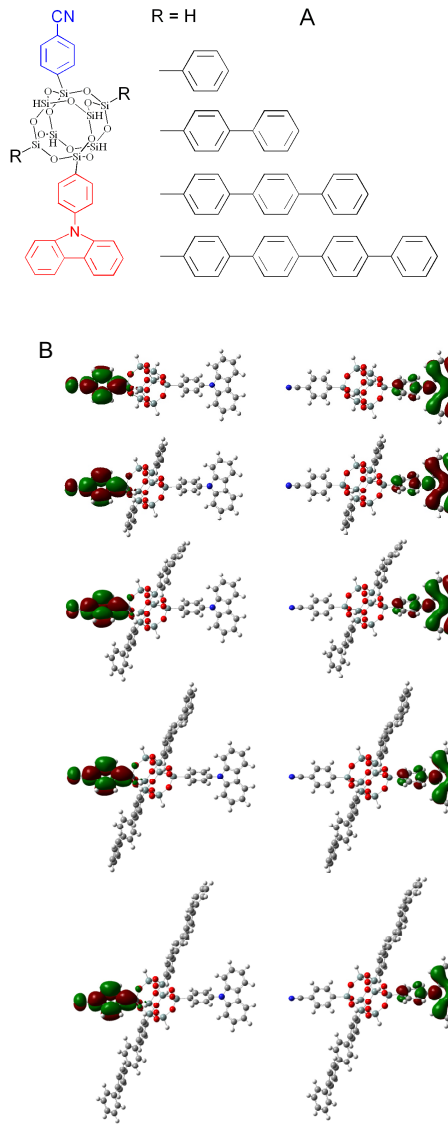

Figure 2.10. (A) Molecular structures of POSS derivatives with a fixed electron-donating group and electro-withdrawing group attached to the POSS cage while increasing the length of the side groups. Exciton binding energies for these molecules are all equal to 0.181 eV. (B) Electron iso-density contours (0.02 au), left: LUMO, right: HOMO.

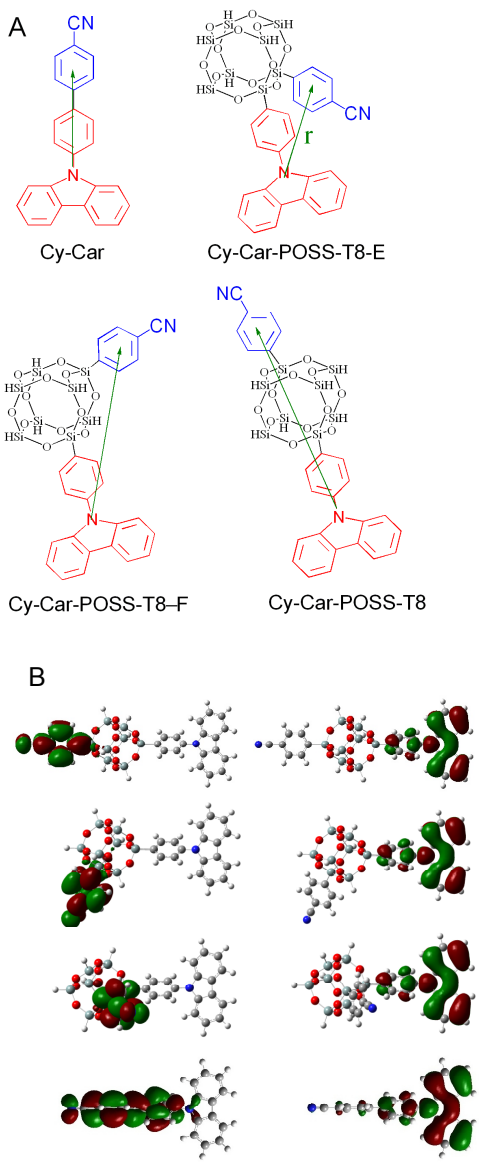

Figure 2.11. (A) Molecular structures of POSS derivatives with electron-donating group and electron-withdrawing group attached to the POSS cage in different positions. The green arrows indicate the spatial separation between HOMO and LUMO. (B) Electron iso-density contours (0.02 au), left: LUMO, right: HOMO.

in the polyphenyl moieties is varied from 0 to 4. Accordingly, the molecule lengths range from 5.7 Å to 43 Å, measured along the polyphenyl moieties. The distribution of the HOMO and LUMO are similar for all these molecules, i.e., the HOMO is mainly localized in carbazolephenyl group and the LUMO in cyanophenyl group. Our calculated E_b for all these molecules are identical to that of Cy-Car-POSS-T8, which is consistent with our conjecture.

For (II), we attached the cyanophenyl group and carbazolephenyl groups to different silicon atoms along body-diagonal (Cy-Car-POSS-T8), face-diagonal (Cy-Car-POSS-T8-F), or the same edge of the cube (Cy-Car-POSS-T8-E), so that the distance between the electron donating and withdrawing functional groups varies (Figure 2.11). For this series of molecules, we found that E_b is closely correlated with the spacing between those two types of organic functional groups in the molecules (Table 2.7).

Table 2.7. Exciton binding energy (E_b) of POSS derivatives with the functional groups attached at various positions in POSS cage

	Cy-Car-POSS-T8	Cy-Car-POSS-T8-F	Cy-Car-POSS-T8-E	Cy-Car
E_b (eV)	0.181	0.218	0.294	0.426

Further analysis shows that E_b is proportional to the reciprocal of the distance between electron donating and withdrawing groups, where this distance was measured from the nitrogen atom in the carbazole group and the center of the benzene ring in the cyanophenyl group (Fig. 2.12), which represent the spatial separation of HUMO and LUMO. This proportionality originates from the fact that the HOMO and LUMO mainly occupy a small space in carbazolephenyl and cyanophenyl groups and are well separated

so that the interaction between the electron in LUMO and the hole in HOMO can be estimated as the electrostatic potential energy between two point-like particles,

$$U_E = \frac{1}{4\pi\varepsilon_0\varepsilon_r}\frac{q_1 q_2}{r} \tag{2.3}$$

where ε_0 is electric constant, ε_r is dielectric constant, q_1 and q_2 are the charge of two particles and r is the distance between the two particles. For diffusive or severely overlapping HOMO and LUMO (as in the case of Cy-POSS-T8 or Car-POSS-T8), the proportionality between E_b and r does not hold because the point-like approximation is no longer accurate. In these cases, the interaction of electron and hole in HOMO and LUMO does not simply depend on the molecule length any more, nor does the exciton binding energy.

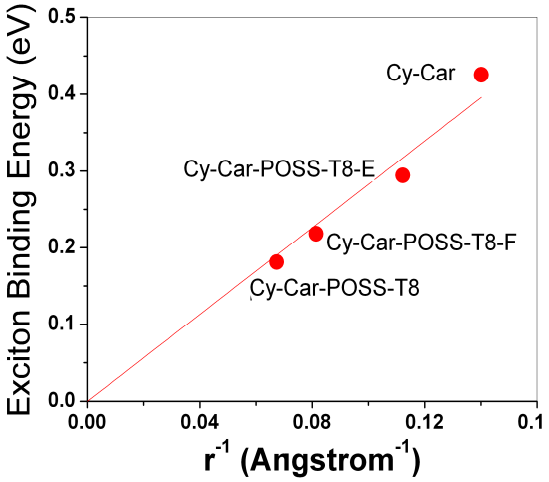

Figure 2.12. Correlation between the exciton binding energies and the spatial separation of HOMO and LUMO. The red line is a linear fit according to equation (2.3).

2.4. Conclusions

Based on studying the structure and electronic properties of POSS-T8 and its functionalized derivatives using DFT and TDDFT calculations, we can report the following findings:

1. The inorganic core of the POSS-T8 is quite rigid. The deformation of the POSS core upon functionalizing the corners of the cube with organic groups and/or by inserting N_2 molecule inside the cage is very small. The rigidity of the POSS cube may affect the aggregation of planar organic conjugated fragments. (Further discussion on this point will be presented in Chapter 3)

2. The POSS cage is partially conjugated and serves the role as electron acceptor. The energy gap of POSS-T8 can be tuned through functionalization. The HOMO and LUMO can be independently controlled by attaching organic functional groups or inserted inorganic atomic clusters, which provides the flexibility to design molecules with targeted properties and for specific applications. The energy range of the HOMO-LUMO gap can be tuned to include visible spectrum, indicating a potential application of POSS compounds for OLEDs and organic solar cells.

3. The reorganization energies of POSS derivatives are generally larger than those of the organic functional groups taken by themselves, implying that the hybrid organic-inorganic molecules exhibit poorer carrier transport properties than their organic counterparts. Unlike commonly used carrier blocking materials due to a carrier injection barrier, isomers of Cy-Car-POSS-T8-N_2 may be used as electron blocking material due to its large electron transport barrier.

4. The exciton binding energy for Cy-Car-POSS-T8 is quite small compared with Cy-Car because the POSS cage separates the electron-donating and electron-withdrawing groups where the HOMO and LUMO are localized. Further study of the correlation

between the exciton binding energy and molecular structures indicates that E_b is closely related to the spatial separation between HOMO and LUMO.

Although this investigation focuses on a specific POSS system, the calculation results and the design principles are expected to be applicable in a broader context for organic molecular materials and organic-inorganic hybrid structures that are useful for organic electronics.

2.5. References

(1) Ebbesen, T. W.; Ajayan, P. M. *Nature* **1992**, *358*, 220-222.

(2) Jarillo-Herrero, P.; van Dam, J. A.; Kouwenhoven, L. P. *Nature* **2006**, *439*, 953-956.

(3) Routkevitch, D.; Bigioni, T.; Moskovits, M.; Xu, J. M. *J. Phys. Chem.* **1996**, *100*, 14037-14047.

(4) Liang, Y. Q.; Zhen, C. G.; Zou, D. C.; Xu, D. S. *J. Am. Chem. Soc.* **2004**, *126*, 16338-16339.

(5) Adams, G. B.; Sankey, O. F.; Page, J. B.; Okeeffe, M.; Drabold, D. A. *Science* **1992**, *256*, 1792-1795.

(6) Scott, L. T.; Boorum, M. M.; McMahon, B. J.; Hagen, S.; Mack, J.; Blank, J.; Wegner, H.; de Meijere, A. *Science* **2002**, *295*, 1500-1503.

(7) Lichtenhan, J. D. *Comments Inorg. Chem.* **1995**, *17*, 115-130.

(8) Sellinger, A.; Laine, R. M. *Chem. Mater.* **1996**, *8*, 1592-1593.

(9) Lamm, M. H.; Chen, T.; Glotzer, S. C. *Nano Lett.* **2003**, *3*, 989-994.

(10) Xiao, S.; Nguyen, M.; Gong, X.; Cao, Y.; Wu, H. B.; Moses, D.; Heeger, A. J. *Adv. Funct. Mater.* **2003**, *13*, 25-29.

(11) Fenenko, L.; Nakanishi, Y.; Tokito, S.; Konno, A. *Jap. J. Appl. Phys., Part 1* **2006**, *45*, 550-554.

(12) Lee, J.; Cho, H. J.; Jung, B. J.; Cho, N. S.; Shim, H. K. *Macromolecules* **2004**, *37*, 8523-8529.

(13) Chou, C. H.; Hsu, S. L.; Dinakaran, K.; Chiu, M. Y.; Wei, K. H. *Macromolecules* **2005**, *38*, 745-751.

(14) Lo, M. Y.; Zhen, C. G.; Lauters, M.; Jabbour, G. E.; Sellinger, A. *J. Am. Chem. Soc.* **2007**, *129*, 5808-5809.

(15) Sellinger, A.; Tamaki, R.; Laine, R. M.; Ueno, K.; Tanabe, H.; Williams, E.; Jabbour, G. E. *Chem. Comm.* **2005**, 3700-3702.

(16) Runge, E.; Gross, E. K. U. *Phys. Rev. Lett.* **1984**, *52*, 997-1000.

(17) Jamorski, C.; Casida, M. E.; Salahub, D. R. *J. Chem. Phys.* **1996**, *104*, 5134-5147.

(18) Amekraz, B.; Tortajada, J.; Morizur, J. P.; Gonzalez, A. I.; Mo, O.; Yanez, M.; Leito, I.; Maria, P. C.; Gal, J. F. *New J. Chem.* **1996**, *20*, 1011-1021.

(19) Goldstein, E.; Beno, B.; Houk, K. N. *J. Am. Chem. Soc.* **1996**, *118*, 6036-6043.

(20) *al.,* F. M. J. *e*. **2004**,

(21) Stewart, J. J. P. *J. Comput. Chem.* **1989**, *10*, 209-220.

(22) Becke, A. D. *J. Chem. Phys.* **1993**, *98*, 5648-5652.

(23) Hehre, W. J.; Ditchfie, R.; Pople, J. A. *J. Chem. Phys.* **1972**, *56*, 2257-2261.

(24) Francl, M. M.; Pietro, W. J.; Hehre, W. J.; Binkley, J. S.; Gordon, M. S.; Defrees, D. J.; Pople, J. A. *J. Chem. Phys.* **1982**, *77*, 3654-3665.

(25) Schlegel, H. B. *J. Comput. Chem.* **1982**, *3*, 214-218.

(26) Earley, C. W. *J. Phys. Chem.* **1994**, *98*, 8693-8698.

(27) Mattori, M.; Mogi, K.; Sakai, Y.; Isobe, T. *J. Phys. Chem. A* **2000**, *104*, 10868-10872.

(28) Larsson, K. *Arkiv Kemi* **1960**, *16*, 215-219.

(29) Tomroos, K. W. *Acta Crystallogr., Sec. C* **1994**, *50*, 1646-1648.

(30) Tejerina, B.; Gordon, M. S. *J. Phys. Chem. B* **2002**, *106*, 11764-11770.

(31) Wu, W. C.; Yeh, H. C.; Chan, L. H.; Chen, C. T. *Adv. Mater.* **2002**, *14*, 1072.

(32) Aubouy, L.; Gerbier, P.; Guerin, C.; Huby, N.; Hirsch, L.; Vignau, L. *Synth. Met.* **2007**, *157*, 91-97.

(33) Azinovic, D.; Cai, J.; Eggs, C.; Konig, H.; Marsmann, H. C.; Veprek, S. *J. Lumin.* **2002**, *97*, 40-50.

(34) Lin, T. T.; He, C. B.; Xiao, Y. *J. Phys. Chem. B* **2003**, *107*, 13788-13792.

(35) Calzaferri, G.; Hoffmann, R. *J. Chem. Soc., Dalton Trans.* **1991**, 917-928.

(36) Sulaiman, S.; Bhaskar, A.; Zhang, J.; Guda, R.; Goodson, T.; Laine, R. M. *Chem. Mater.* **2008**, *20*, 5563-5573.

(37) Feher, F. J.; Budzichowski, T. A. *J. Organomet. Chem.* **1989**, *379*, 33-40.

(38) Miller, A.; Abrahams, E. *Phys. Rev.* **1960**, *120*, 745-755.

(39) Marcus, R. A.; Sutin, N. *Biochim. Biophys. Acta* **1985**, *811*, 265-322.

(40) Coropceanu, V.; Cornil, J.; da Silva, D. A.; Olivier, Y.; Silbey, R.; Bredas, J. L. *Chem. Rev.* **2007**, *107*, 926-952.

(41) Bredas, J. L.; Calbert, J. P.; da Silva, D. A.; Cornil, J. *Proc. Natl. Acad. Sci. U.S.A.* **2002**, *99*, 5804-5809.

(42) Norton, J. E.; Bredas, J. L. *J. Am. Chem. Soc.* **2008**, *130*, 12377-12384.

(43) McMahon, D. P.; Troisi, A. *J. Phys. Chem. Lett.* **2010**, *1*, 941-946.

(44) Aonuma, M.; Oyamada, T.; Sasabe, H.; Miki, T.; Adachi, C. *Appl. Phys. Lett.* **2007**, *90*, 183503.

(45) Ballistreri, F. P.; Fortuna, C. G.; Musumarra, G.; Pavone, D.; Scire, S. *Arkivoc* **2002**, 54-64.

(46) Tsutsui, T.; Aminaka, E.; Tokuhisa, H. *Synth. Met.* **1997**, *85*, 1201-1204.

(47) Kulkarni, A. P.; Tonzola, C. J.; Babel, A.; Jenekhe, S. A. *Chem. Mater.* **2004**, *16*, 4556-4573.

(48) Adamovich, V. I.; Cordero, S. R.; Djurovich, P. I.; Tamayo, A.; Thompson, M. E.; D'Andrade, B. W.; Forrest, S. R. *Org. Electron.* **2003**, *4*, 77-87.

(49) Franceschetti, A.; Zunger, A. *Phys. Rev. Lett.* **1997**, *78*, 915-918.

(50) Gregg, B. A. *J. Phys. Chem. B* **2003**, *107*, 4688-4698.

(51) Cao, Y.; Parker, I. D.; Yu, G.; Zhang, C.; Heeger, A. J. *Nature* **1999**, *397*, 414-417.

(52) Karabunarliev, S.; Bittner, E. R. *Phys. Rev. Lett.* **2003**, *90*, 057402.

(53) Chen, L. P.; Zhu, L. Y.; Shuai, Z. G. *J. Phys. Chem. A* **2006**, *110*, 13349-13354.

(54) Roslyak, O.; Birman, J. L. *Phys. Rev. B* **2007**, *75*, 245309.

(55) Marciniak, H.; Fiebig, M.; Huth, M.; Schiefer, S.; Nickel, B.; Selmaier, F.; Lochbrunner, S. *Phys. Rev. Lett.* **2007**, *99*, 176402.

(56) Baldo, M.; Segal, M. *Phys. Status Solidi A* **2004**, *201*, 1205-1214.

(57) Sun, M. T.; Kjellberg, P.; Beenken, W. J. D.; Pullerits, T. *Chem. Phys.* **2006**, *327*, 474-484.

(58) Scholes, G. D.; Rumbles, G. *Nat. Mater.* **2006**, *5*, 683-696.

(59) Kemerink, M.; Alvarado, S. F.; Muller, P.; Koenraad, P. M.; Salemink, H. W. M.; Wolter, J. H.; Janssen, R. A. J. *Phys. Rev. B* **2004**, *70*,

(60) Marks, R. N.; Halls, J. J. M.; Bradley, D. D. C.; Friend, R. H.; AB, H. *J Phys.-Conden. Mat.* **1994**, *6*, 1379-1394.

(61) Wu, C.; Tretiak, S.; Chernyak, V. Y. *Chem. Phys. Lett.* **2007**, *433*, 305-311.

(62) Magyar, R. J.; Tretiak, S. *J. Chem. Theory Comput.* **2007**, *3*, 976-987.

(63) Nie, D. B.; Bian, Z. Q.; Yu, A. C.; Chen, Z. Q.; Liu, Z. E.; Huang, C. H. *Chem. Phys.* **2008**, *348*, 181-186.

(64) Rettig, W.; Zander, M. *Chem. Phys. Lett.* **1982**, *87*, 229-234.

(65) Lu, C. H.; Chang, F. C. *Chem. Phys. Lett.* **1982**, *87*, 229-234.

Chapter 3. Computational design of dipentacene POSS nanocomposite with very high charge mobilities

3.1. Introduction

Charge mobility is a very important parameter in determining the performance of organic optoelectronic devices.[1] Balanced electron and hole mobilities are required to achieve high efficiency in organic light-emitting diodes (OLEDs).[2] Organic materials with high carrier mobility (small series resistance) are desirable to enhance the fill factor of organic solar cells.[3,4] Therefore, controlling mobility in organic materials is highly desired for practical applications. In this work, we will describe our efforts using theoretical model to design organic-inorganic hybrid molecules with very high charge mobility based on pentacene and polyhedral oligomeric silsesquioxanes (POSS).

Polyacenes including pentacene are known to exhibit very high charge mobilities.[5] Recently, Jurchescu *et. al.* achieved hole mobility of 11.2 cm^2/Vs at room temperature in ultrapure pentacene crystals.[6] However, pentacene molecules arrange in a herringbone structure in single crystals, in which the neighboring molecules form a V-shaped pattern rather than a parallel configuration. This precludes adequate wavefunction overlap between molecules and consequently affects the charge hopping between the molecules. From the point of view of molecular engineering, if we can control the orientation of pentacene to be parallel and thereby achieve larger wavefunction overlap between

adjacent molecules, we can improve the charge mobility. In our previous theoretical study on POSS and its functionalized derivatives, we noticed that for individual molecules, functional organic groups attached to the POSS cage can only adopt certain orientations due to its rigidity and three-dimensional structure.[7] A previous theoretical study in our group also reveals that for crystals of functionalized POSS derivatives, the organic functional groups tend to aggregate to form organic phases while the POSS cages tend to aggregate to form inorganic phases, as identified with molecular dynamics simulation.[8] Therefore, by attaching pentacene to the rigid POSS cage to form organic-inorganic hybrid molecules we are potentially able to control the orientation of pentacene segments. Indeed, as shown below, the simulation results indicate that the orientation of molecules in the crystals of dipentacene POSS hybrid material results in pentacene groups that are parallel to each other and the hole mobility can be as high as 415 cm^2/Vs at 300K, one order of magnitude higher than that in its purely organic counterpart, crystalline pentacene.

3.2. Methodology

3.2.1. Electronic properties of individual molecules

Calculations on the molecules were performed using Gaussian03.[9] Pre-optimizations of the molecules were carried out using AM1 semi-empirical quantum chemistry model.[10] The resulting molecular configurations were used as the starting atomic coordinates for further optimization in the DFT framework. We chose B3LYP as the exchange-correlation functional, which is a Hartree-Fock-DFT hybrid where the exchange energy is calculated explicitly using a Hartree-Fock approach.[11] The molecular geometries were

optimized in the Cartesian coordinate system without any symmetry (maximum degrees of freedom) using the 6-31G* contracted Gaussian basis set with polarization functions.[12]

3.2.2. Crystal structures

The identification of the most probable crystal structures for the various candidate building blocks was accomplished using Polymorph, a part of the Accelrys' Materials Studio suite of programs. These structure optimization simulations were based on the COMPASS force field,[13] which provided the expediency required for sampling large numbers of trial structures. Possible stable crystalline structures were identified as those with the lowest total energies. Subsequently, SIESTA was used to further relax these structures towards their ground state configurations, using split-valence double-zeta basis set with the Perdew–Burke–Ernzerhof functional. The exchange-correlation energy was evaluated in the generalized gradient approximation (GGA). Once the most probable configuration was determined by relaxing these initial structures with DFT total energy minimization procedures, the charge transfer integral between the dimers in the most probable crystal structure were then calculated in Gaussian03 at the same approximation level as for the individual molecules, i.e., B3LYP/6-31G*.

3.2.3. Charge transport

Charge transport can be simulated using band or hopping models for organic semiconductors. Recently, a study of the transport properties in polyacenes based on a tight-binding band model with electron-phonon scattering under a constant time approximation revealed a mean free path of charge carriers comparable or even shorter

than the lattice constant at high temperatures, indicating a localized picture within organic semiconductors.[14] The band model fails due to the weak interaction between organic molecules, which are held together by van der Waals forces. Instead, the charge transport mechanism is more accurately described by hopping models, in which holes and electrons hop between discontinuous localized electronic states.[15] We simulated hopping processes based on Marcus' electron transfer theory, which has been used by Kwiatkowski *et. al.*.[16] According to Marcus' theory, the conductivity depends on the electron (or hole) transfer reactions between two adjacent molecules (hopping sites), [17] represented by M_1 and M_2

$$M_1^{\pm} + M_2^0 \rightarrow M_1^0 + M_2^{\pm} \tag{3.1}$$

The hopping rate can be described by Marcus' electron transfer equation:

$$W = \frac{2\pi}{\hbar} \frac{V^2}{\sqrt{4\pi\lambda kT}} \exp(-\frac{(\Delta G + \lambda)^2}{4\lambda kT}) \tag{3.2}$$

where k is Boltzmann's constant, λ is the reorganization energy, V is the charge-transfer integral, ΔG is the free energy change for the electron transfer reaction, and T is temperature. The charge transfer integral, V, is determined by the overlap of wavefunction between adjacent molecules, which is determined by the relative spatial overlap and patterns of the wavefunctions.[18]

The free energy change when an the electron (hole) hops from molecule i to j is defined as:

$$\Delta G = E_j(M_j^{\mp 1}, M_{l\neq j}^0) - E_i(M_i^{\mp 1}, M_{l\neq i}^0) \pm e\vec{r}_{ij} \cdot \vec{F} \tag{3.3}$$

where the energy $E_j(M_j^{\mp 1}, M_{l\neq j}^0)$ is the electrostatic interaction energy of the system in which molecule *j* is anion (cation) and the others are neutral, *e* is unit charge, $\vec{r}_{ij}$ is the vector between the centers of the hopping sites, and $\vec{F}$ is the electric field. For simplicity, we assume that a charge that occupies molecule *j* is re-distributed over orbitals associated with this molecule, but atomic charges in the atoms of other molecules are not affected. If the energy of the system in which all the molecules are neutral is chosen as the reference state, then

$$E_j(M_j^{\mp 1}, M_{l\neq j}^0) = \frac{1}{4\pi\varepsilon_0}\left(\sum_{m,n\in j, m<n} \frac{(q_{jm}^{\mp 1} - q_{jm}^0)(q_{jm}^{\mp 1} - q_{jn}^0)}{\varepsilon_{jm,jn} r_{jm,jn}} + \sum_{m\in jk} \sum_{l\neq j} \frac{(q_{jm}^{\mp 1} - q_{jm}^0) q_{lk}^0}{\varepsilon_{jm,lk} r_{jm,lk}} \right) \tag{3.4}$$

where ε_0 is electric constant. $q_{jm}^{\mp 1}$ is atomic charge of atom *m* in molecule *j* in which a charge is localized. The atomic charge is taken as Mulliken charge calculated from individual molecules. $r_{jm,lk}$ is the distance between atom *m* in molecule *j* and atom *k* in molecule *l*, and $\varepsilon_{jm,lk}$ is distance-dependent dielectric constant, [19]

$$\varepsilon_{jm,lk} = \varepsilon_b - (\varepsilon_b - 1)e^{-sr_{jm,lk}}(1 + sr_{jm,lk} + (sr_{jm,lk})^2/2) \tag{3.5}$$

where ε_b is the bulk dielectric constant (set to be 3.0 for organic semiconductors here) and the parameter *s* is set to be 0.3 $Å^{-1}$.[19]

Once the hopping rates between the dimers are determined using equation (3.2), a kinetic Monte-Carlo algorithm is used to simulate the charge transport in the organic

crystals. We create the system with periodic boundary conditions. Initially, the charge is randomly localized in one molecule *i*. The hopping rates for the charge from molecule *i* to all its neighbours are calculated using equation (3.2). The hopping probability for the charge to molecule *j* is

$$P_{i\to j} = W_{i\to j} \Big/ \sum_{j'} W_{i\to j'} \tag{3.6}$$

After determining the next position for the charge, the Monte-Carlo simulation time is increased by $1 \Big/ \sum_{j'} W_{i\to j'}$ and the hopping distance along the electric field is recorded. The simulation continues until the total hopping distance along the electric field is equal or larger to a pre-set value (corresponding to the distance between two electrode in time-of-flight experiments). Then the mobility is evaluated as

$$\mu = \frac{r_{tot} / t_{tot}}{F} \tag{3.7}$$

where r_{tot} is the total hopping distance along the electric field and t_{tot} is the total hopping time.

3.3. Results and discussion

3.3.1. Ground state geometry and electronic structure

In optimized dipentacene POSS, the two pentacene segments attached to the POSS cage are parallel to each other and lie in the same plane, at a maximum separation (Figure 3.1). The length of the hybrid molecule is 3.54 nm, making it suitable as nanoscale building block. The POSS cage is very rigid even after functionalization by organic

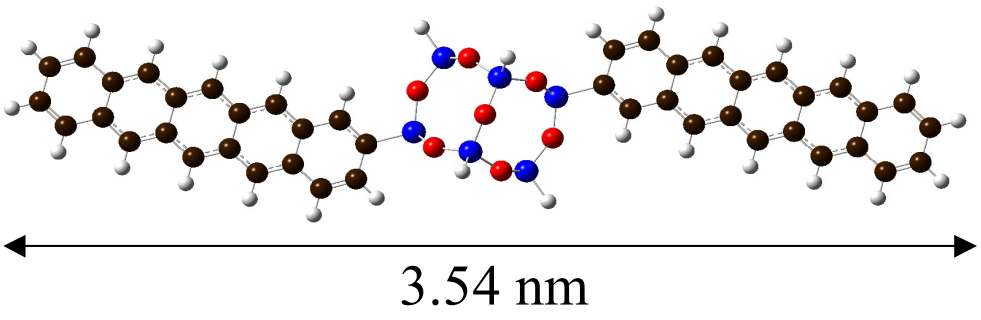

Figure 3.1. Optimized molecular structure of dipentacene POSS at the approximation level of B3LYP/6-31G*. The rigidity and three-dimensional structure of POSS cage force pentacene segments to only adopt certain directions.

groups.[11] In the cases here, the deformation of the cage after functionalization by acenes can be measured by the change in the distance between two silicon atoms along the body diagonal before and after attaching the pentacene segments. In POSS, this distance is 5.473 Å, while in the hybrid molecules it is 5.517 Å, i.e., only 0.8% larger.

Comparing the electron density isosurfaces of dipentacene POSS and pentacene (Figure 3.2), we can see that the frontier orbitals of the hybrid molecule are mainly

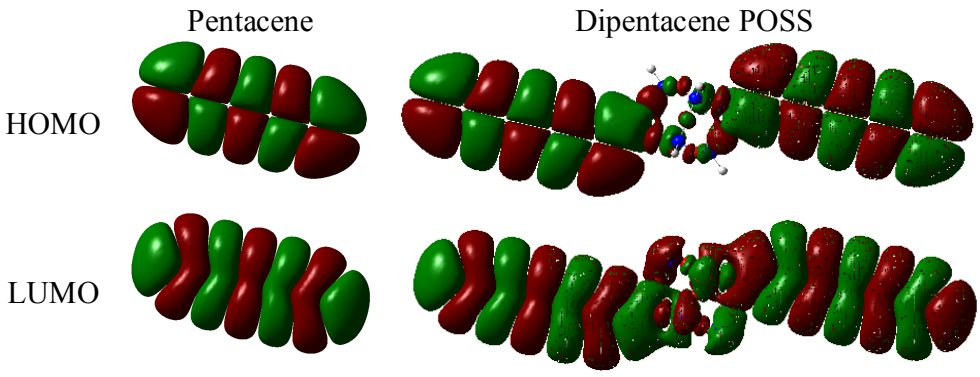

Figure 3.2. Electron density isocontours (0.0005 au) of pentacene and dipentacene POSS. The frontier orbitals mainly localize on pentacene segments and partially on POSS cage. POSS cage makes more contribution to LUMO than to HOMO, indicating its electron accepting property.

located on pentacene. On the other hand, we also notice contributions from the POSS cages, i.e., the frontier orbitals extend inside the cage. The POSS cage makes more of a contribution to the lowest unoccupied molecular orbitals (LUMO) than to the highest occupied molecular orbitals (HOMO). This is consistent with our previous finding that the POSS cage is partially conjugated and serves as electron acceptor (Chapter 2). Hence, we can expect the electronic properties of the hybrid molecule be dominated by the pentacene segments but influenced by the POSS core. Indeed, HOMO (-4.72 eV) and LUMO (-2.52 eV) of the hybrid molecule are close to the HOMO (-4.60 eV) and LUMO (-2.38 eV) of pentacene. The HOMO-LUMO gap (2.20 eV) of the hybrid molecule is much smaller than POSS (8.85 eV) and very close to that of the pentacene (2.22 eV). We also notice that the LUMO of the hybrid molecule is lower than that of pentacene due to the electron accepting ability of POSS core (Chapter 2).

3.3.2. Reorganization energy

According to Marcus' electron transfer equation, the reorganization energy plays an important role during the charge transfer process. The reorganization energy, λ, represents the activation barrier due to the configurational adjustment of molecules during charge transfer. λ consists of both the inner reorganization energy and the external polarization of the surrounding medium. Here we only consider the inner reorganization energy, since the external reorganization energy has been demonstrated to be negligibly small compared with the inner reorganization energy.[20,21] The inner reorganization energies are obtained by comparing the energies of the charged and uncharged optimized configurations, for both the neutral and ionized states. Accordingly,

$\lambda = E_A^B - E_B + E_B^A - E_A$, where E_A^B is the energy of the ion in the optimized uncharged geometry, E_B is the energy of the ion in the optimized charged geometry, E_B^A is the energy of the neutral molecule in the optimized charged geometry, and E_A is the energy of the neutral molecule in the optimized uncharged geometry. The calculated reorganization energy for hole transfer (λ_+) is 0.071 eV in the hybrid molecule, compared to λ_+ of 0.089 eV for pentacene. The calculated reorganization energy for hole transport in pentacene at the is close to the experimental value of 0.099 eV.[22]

The reorganization energies of the dipentacene POSS are smaller than those of pentacene. This suggests that the organic-inorganic hybrid material has a lower activation energy for structural reconfiguration during charge transfer. To investigate the origin of the lower reorganization energies of dipentacene POSS, we examined the geometric deformation of the hybrid molecule and pentacene during charge transfer. The changes in bond length of these two molecules indicate that the deformation of pentacene by itself is larger than that of dipentacene POSS (Figure 3.3 and Appendix A).

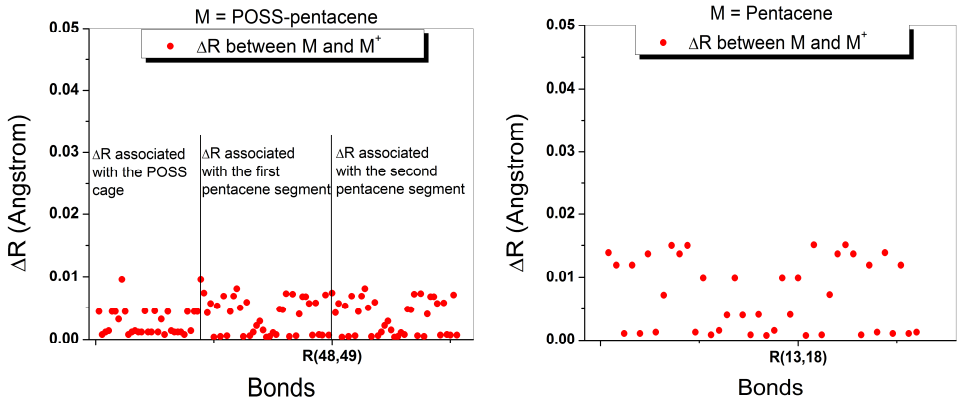

Figure 3.3. Deformation of dipentacene POSS and pentacene during hole transport. The smaller deformation of dipentacene POSS compared to pentacene leads to smaller reorganization energy.

All bond deformations in dipentacene POSS are less than 0.01 Å while around half of the changes in bond length of pentacene are in the range of 0.01 ~ 0.017 Å. We notice that the deformations associated with the POSS cage in dipentacene POSS are smaller than those associated with the pentacene segments, which implies that the rigidity of the cage is maintained during charge transfer. We also notice that the deformations associated with the two pentacene segments are highly symmetric, indicating that the wavefunction distribution on the molecule may be symmetric even during charge transfer.

3.3.3. Crystal structure and charge transfer integral

The charge transfer integral strongly depends on the molecular packing and the pattern of the molecular wavefunctions.[18] The π - π orbital overlap between hopping couples is highly desired for good intermolecular charge transfer.[1] Hence, the parallel face-to-face configurations of conjugated segments are preferred in organic solids for high carrier mobility.

To determine the geometric configuration of the hopping couples in the crystals, we explored the most probable crystalline structures by searching for the most stable stacking configurations as characterized by the lowest energies. The search for the lowest-energy configurations was conducted using the Polymorph from Accelrys, in which a large number of crystalline packing configurations are generated via Monte-Carlo method, followed by geometry optimization of these structures based on a smart energy minimization algorithm. In the process, duplicate structures that the algorithm converges on are eliminated. The lowest-energy crystal structure is considered the most likely polymorph. As a final step, the stability of this structure is verified using SIESTA,

in which the Parrinello-Raman algorithm is used to control the size and shape of the simulation box.

Figure 3.4 and Figure 3.5 show the most probable crystal structures of dipentacene POSS. The lowest energy and highest density structure was found for the crystal structure with P $\bar{1}$ symmetry, while P21/c was a close second in terms of these attributes. Both have two molecules per unit cell, as does the pentacene crystal.[23] The structure with Pbca symmetry has higher energy, indicating that it may not be as stable as those with P $\bar{1}$ or P21/c symmetry. The predicted crystal information is listed in Table 3.1.

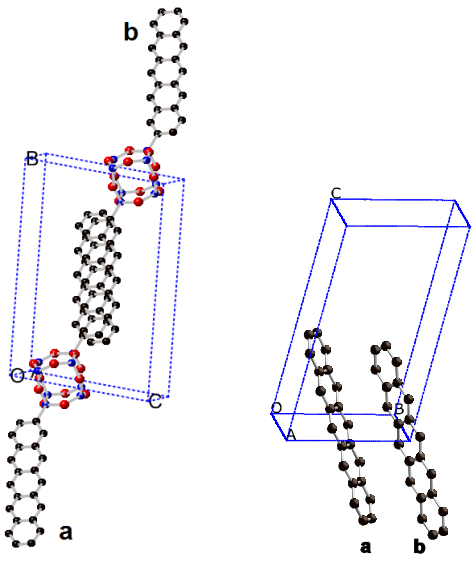

Figure 3.4. (Left) The most possible crystal structure of dipentacene POSS. (Right) Crystal structure of pentacene. There are two molecules in one unit cell of dipentacene POSS crystal. Unlike the two molecules formed a V-shape in pentacene, the pentacene segments in the two molecules in dipentacene POSS crystal structure form parallel configuration, which may have larger wavefunction overlap.

Due to procedural inaccuracies in the calculations, discrepancies between predicted and experimental structures may be expected. However, the three structures predicted to have the lowest energies are all characterized by paralleled packing of the pentacene segments, in contrast to the herringbone stacking in pure crystalline pentacene. This provides an enhanced π - π orbital overlap, and as a

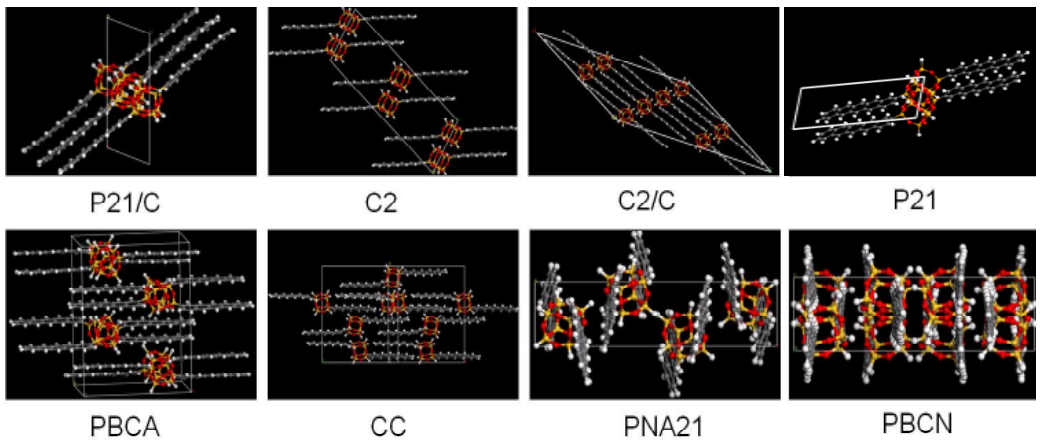

Figure 3.5. Other possible crystal structures of dipentacene POSS. Note that in most of the structures the pentacene segments adopt parallel configuration.

consequence, in this new hybrid material, one may expect comparable or even higher charge mobility than in pentacene.

Table 3.1. Properties of predicted most possible crystal structures of dipentacene POSS

Space group	$P\bar{1}$	P21c	Pbca
a	7.2103	20.1273	7.1066
b	20.3716	29.4681	78.9321
c	16.6646	7.1877	14.8107
α	107.55	90	90
β	118.397	69.7388	90
γ	67.171	90	90
Density g/cc	1.6530	1.6233	1.5629
vdW*	-68.7875	-76.7005	-71.0240
Electrostatic*	-759.0595	-761.2701	-762.4897
E_{Tot} [a]	-34.2801	-31.8428	-26.3488

[a] Energy Unit: $Kcal^{-1}mol^{-1}$asymmetry $cell^{-1}$.

We calculated the charge transfer integrals for the hopping couples of nearest neighboring pentacene fragments in the dipentacene POSS crystal of $P\bar{1}$ and nearest neighboring pentacene molecules in *ab* plane of pentacene crystal (from experiment[23]) using a direct method.[24] In this method, electronic coupling can be described by $H_{da} = \left\langle \phi_{HOMO}^{0,site1} \middle| F \middle| \phi_{HOMO}^{0,site2} \right\rangle$. $\phi_{HOMO}^{0,site1}$ and $\phi_{HOMO}^{0,site2}$ are the HOMOs of two individual molecules. *F* is the Fock matrix for the hopping couple, with the density matrix constructed from non-interacting molecular orbitals. In practice, $F=SC\ \varepsilon\ C^{-1}$, where *S* is the overlap matrix of the dimer, and orbital *C* and eigenvalue ε are obtained by diagonalizing the zeroth-order Fock matrix without any SCF iteration.[24] The results are listed in Table 3.2.

Table 3.2. Calculation results of charge transfer integrals

Pentacene					
Hopping couples		Hopping direction			H_{da} (meV)
M_1	M_2	OA	OB	OC	
a	a	1	0	0	53.20 (49.7)
b	b	1	0	0	57.97 (51.0)
a	b	0	0	0	-85.04 (74.4)
a	b	1	0	0	135.68
a	b	0	1	0	135.70 (130.1)
a	b	1	1	0	-85.02
Dipentacene POSS					
Hopping couples		Hopping direction			H_{da} (meV)
M_1	M_2	OA	OB	OC	
a	a	0	1	0	30.89
a	a	1	1	0	-31.88
a	b	0	1	1	-205.46
a	b	1	1	1	-49.18
b	b	0	1	0	144.49
b	a	1	1	0	-14.96
b	b	1	1	0	-146.49
b	a	2	1	0	-3.48

Data in parenthesis are from reference.[25]

The calculated charge transfer integrals for dimers in pentacene are comparable to those reported by Troisi and Orlandi.[25] By comparing charge transfer integrals for pentacene and dipentacene POSS, we find that the charge transfer integrals for hole hopping in dipentacene POSS are larger than those of pure pentacene. Combining the calculated result that the reorganization energy for dipentacene POSS is smaller than that for pentacene, we expect that the hole mobility in dipentacene POSS is comparable or even higher than that in pentacene.

3.3.4. Site energy difference

Energy of site *i* is defined as the energy of the system with an electron or hole localized in molecule *i* while all other molecules are neutral. Site energy difference between site *i* and site *j* corresponds to the free energy change of the system when electron or hole hops from *i* to *j* without external electric field (see equation (3.3)).

For energy convergence of the long-range electrostatic interaction calculations, there are two popular methods: cutoff and Particle Mesh Ewald (PME).[26] For our purpose it was important to choose a computationally efficient technique with the cutoff method, which has been demonstrated for some cases to be sufficiently accurate.[26] In our approach towards calculating the site energy, we use a distance-dependent dielectric constant that increases with distance between two particles. Therefore, at larger distances, the contribution to the site energy difference is smaller. Furthermore, what we are primarily concerned with is the site energy difference during charge hopping: the interaction of the charge with the atoms at long-range will not change too much, so that the site energy difference will converge at some cutoff distance (Figure 3.6).

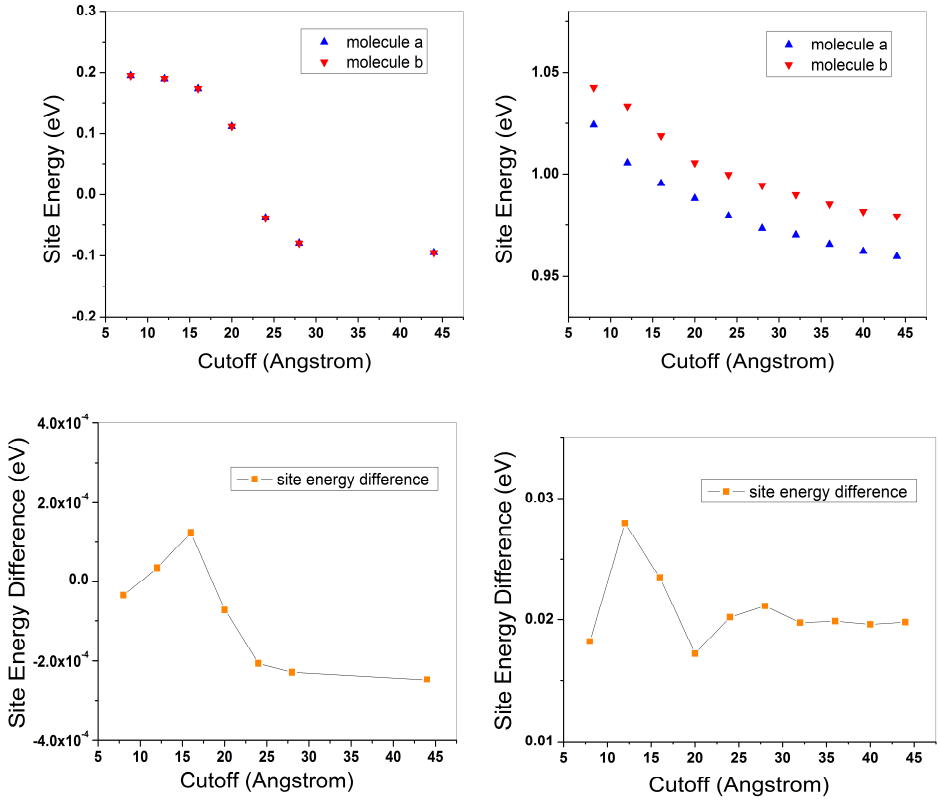

Figure 3.6. Site energy and site energy difference when a hole localizes on different molecules in POSS-pentacene crystal (left) or in pentacene crystal (right).

The site energy difference between the two molecules in dipentacene POSS unit cell is 2×10^{-4} eV, two orders of magnitude lower than in pentacene (2×10^{-2} eV). Therefore, in crystalline pentacene, the free energy change during charge hopping is not as sensitive to the direction of the external electric field as in the dipentacene POSS crystal, *i.e.*, the hopping direction is not mainly controlled by the electric field in pentacene crystal. In contrast, the site energy difference in dipentacene POSS is so small that free energy change during charge transport is almost entirely determined by external electric field. As a consequence, since the charge hopping path favors the direction of the negative free energy gradient, in dipentacene POSS this direction is defined by the external electric

field, if electronic coupling is spatially isotropic. This may result in a more efficient hopping path along the electric field, leading to higher measured charge mobility. The large site energy difference between the two molecules in pentacene originates from the herringbone structure in which the two molecules are surrounded by molecules with different orientation. Conversely, the orientation of the two molecules in dipentacene POSS unit cell is almost the same, i.e., the long axes of the inorganic cage and the organic fragments in molecules are parallel, respectively.

3.3.5. Transport properties

The pentacene crystal is characterized by a layered structure, i.e., in the crystallographic b-direction organic layers containing pentacene are separated by inorganic layers, occupied by POSS cages (Fig. 3.7). The charge mobility within the layers is larger than that between layers due to larger wavefunction overlap between molecules in the same layers. Here, we

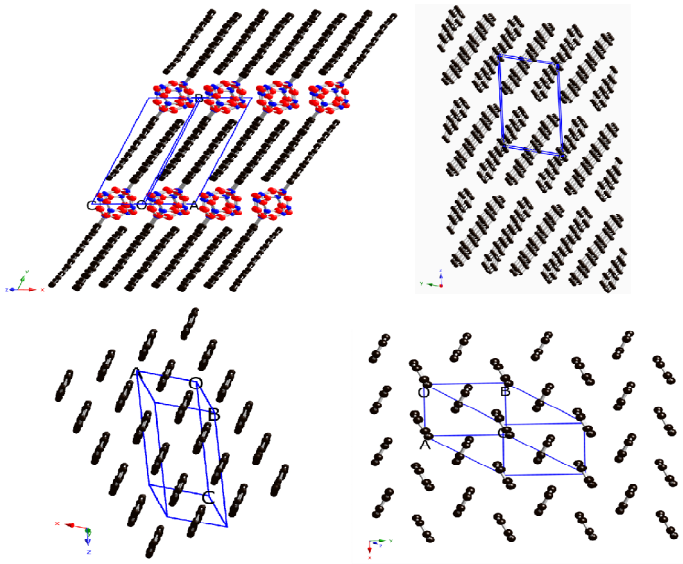

Figure 3.7. Layered structure in dipentacene POSS crystal (left up), layered structure in pentacene crystal (right up), one pentacene layer in dipentacene POSS crystal (left down), and one pentacene layer in pentacene crystal (right down). Up, hydrogen atoms are omitted. Down, only carbon atoms are displayed.

compare hole transport under an electric field in the OA and OB directions of the *ab* plane in pentacene crystal, and the OA and OC directions (in the layer formed by pentacene segments) in dipentacene POSS crystal.

Before we evaluate the hole transport of dipentacene POSS, we test our hopping model by comparing the simulated results with experiment data of pentacene crystal (Figure 3.8). The experimental hole mobility of single crystal pentacene is determined from space-charge-limited current (SCLC) measurements.[6] The mobility was determined from the trap-free region of the space-charge-limited current regime, where the electric field is around 2×10^5 V/m.[6] Therefore, our simulation was under an applied electric field to mimic the experimental condition. The comparison between simulated and experimental data is as follows: (1) the simulated result is higher than the experimental result. Note that our calculation is based on single crystals without any impurity of defect. The mobility obtained from simulation can be considered an upper limit. (2) The temperature dependence of the mobility of pentacene obtained from simulation is similar to the one

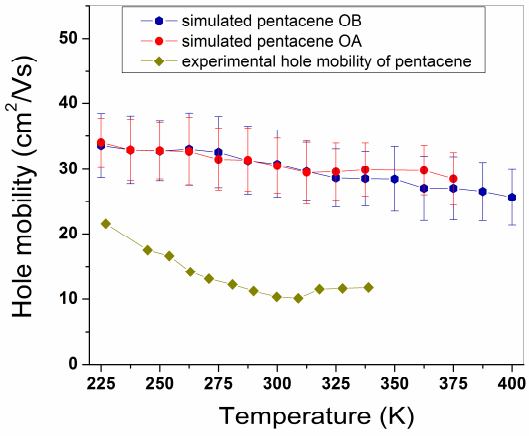

Figure 3.8. Comparison of the simulation result from hopping model and experimental data of hole mobility of pentacene. The trend of mobility vs. temperature in simulation is similar to experiment. At 300 K, simulated mobility is around 31 cm^2/Vs, higher than the experimental value of 11.2 cm^2/Vs. This is reasonable as there are no defects or impurities in crystal in simulation.

observed experimentally. Both the simulated and experimental hole mobility have a minimum at around 310 K. At temperatures lower than room temperature, the experimental hole mobility increases faster than simulation results. At higher temperatures, both experimental and simulated hole mobilities increase slightly and/or stay flat.

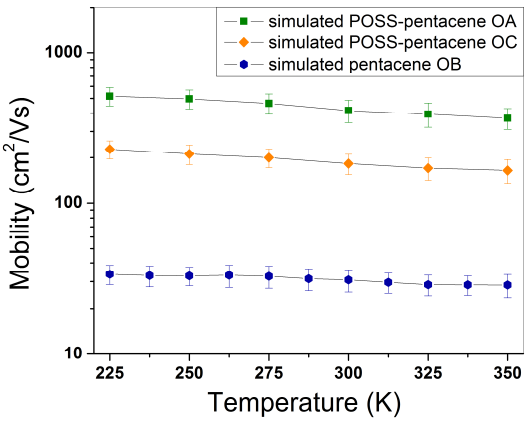

Figure 3.9. Comparison of the simulated hole mobility in dipentacene POSS crystal. At 300 K, simulated mobility along OA direction in dipentacene POSS crystal is 415 cm^2/Vs, one order of magnitude higher than that of 31 cm^2/Vs in pentacene crystal.

The simulation results for dipentacene POSS crystal are very promising. The hole mobility in the dipentacene POSS single crystal is one order of magnitude larger than that of pentacene, reaching as high as 415 cm^2/Vs at 300 K along the OA direction (Figure 3.9).

Examples of hopping paths in pentacene and dipentacene POSS are shown in Figure 3.10. The hops are roundabout locally, appearing to be random at short distances, but on a larger scale the hopping paths follow certain overall directions. The total number of hopping steps we considered to establish hole transport properties in pentacene and dipentacene POSS are2.1×10^7 and 8.6×10^6, respectively. This corresponds to a charge migration distance of over 10 μm along external electric field. Note that the migration

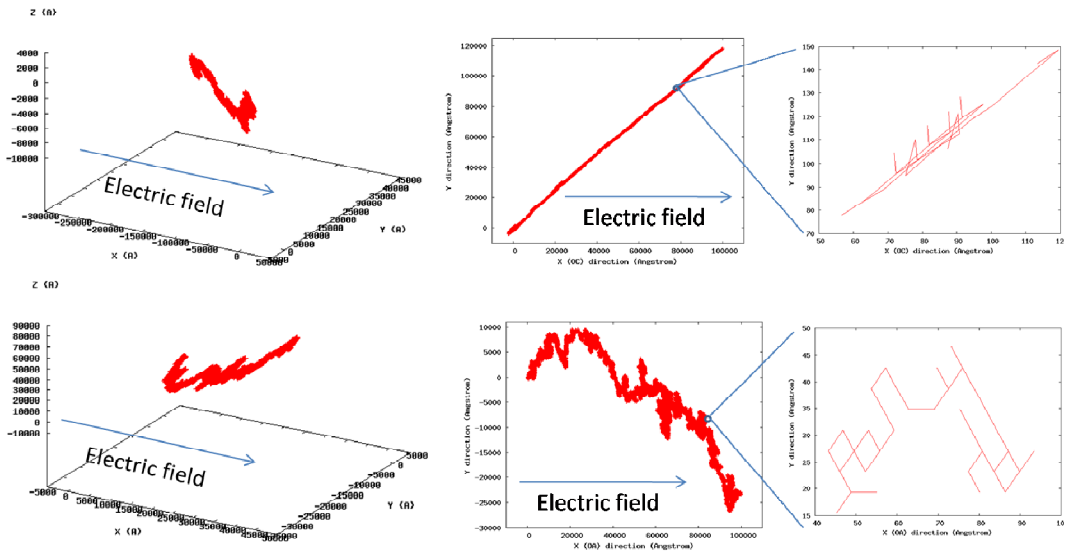

Figure 3.10. Examples of hopping paths in dipentacene POSS (top) and pentacene (bottom). The electric field is along OC direction in dipentacene POSS and OA direction in pentacene. (Left) the hopping path in 3D. (Top center) the projection of hopping path on OA-OC plane in dipentacene POSS. (Bottom center) the projection of hopping path on OA-OB plane in pentacene. (Right) the roundabout nature of hopping in small scale.

paths are on average not parallel to the applied electric field. This is because the charge carriers are energetically pre-disposed to stay within the layers formed by laterally adjacent pentacene groups. In other words, charges prefer to jump laterally from pentacene to pentacene as opposed to along the axial direction from end to end of adjacent pentacene groups, whether in pure pentacene or in dipentacene POSS. However, jumps along the axial direction do occur; they are just significantly less frequent.

As discussed above, the possible reasons for higher mobility of dipentacene POSS crystal over pentacene crystal is the parallel configuration of the pentacene segments. To confirm this conjecture, we carried out simulations for hole mobility along OC direction

in a pentacene stack with the same configuration as the pentacene segments in the crystal structure of dipentacene POSS without the POSS cages (Figure 3.11). The site energy difference in this pentacene stack is 6×10^{-4} eV, somewhat higher than in dipentacene POSS but still much lower than in the natural crystalline structure of pure pentacene. The largest charge integral of the hopping dimers in the pentacene stack is 306 meV, compared to 205 meV for dipentacene POSS and 136 meV for pure crystalline pentacene. Indeed, the mobility along the OC direction in such a configuration is comparable to dipentacene POSS (Figure 3.12) and much higher than that in pentacene crystal.

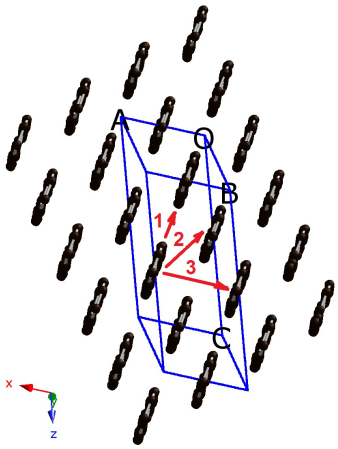

Figure 3.11. Pentacene molecules in the same configuration as the pentacene segments in dipentacene POSS crystal. The OA, OB, OC directions are the same as in dipentacene POSS crystal. The charge transfer integrals for hopping path 1, 2, and 3 are 1.8 meV, 306 meV, and 0.78 meV, respectively.

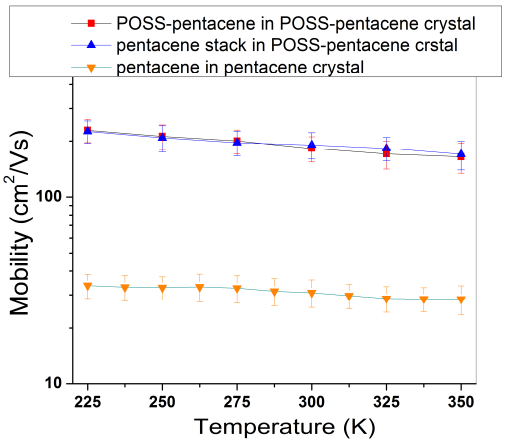

Figure 3.12. Hole mobility in pentacene stack in the configuration as pentacene segments in dipentacene POSS crystal along OC direction. For comparison, hole mobility in dipentacene POSS along OC direction and hole mobility in pentacene crystal along OB direction are also presented.

To further investigate the effect of the three important parameters of site energy difference, charge transfer integral and reorganization energy on hole mobility, hole transport in structures with various combination of these parameters were simulated

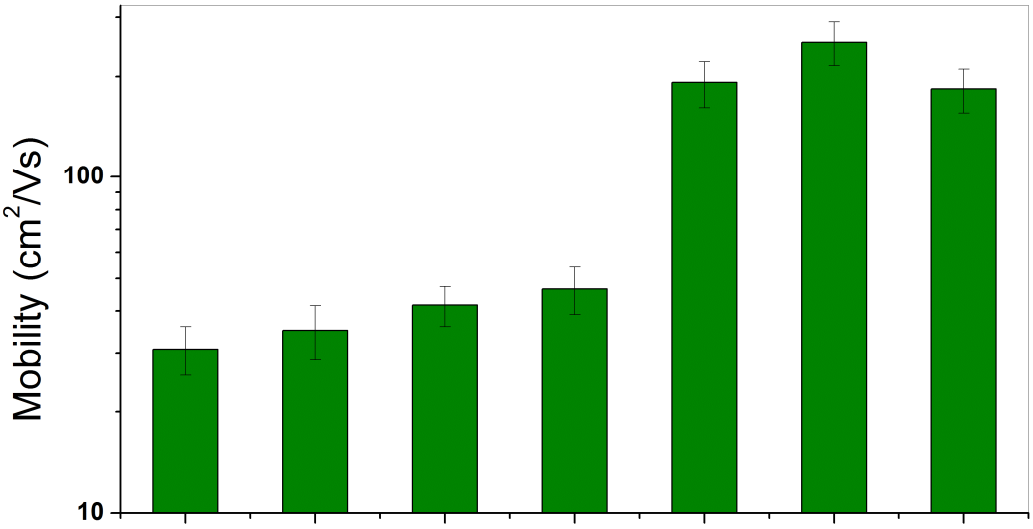

Site energy difference(eV)	2×10^{-2}	2×10^{-4}	2×10^{-2}	2×10^{-4}	6×10^{-4}	6×10^{-4}	2×10^{-4}
Reorganization energy (eV)	0.089	0.089	0.071	0.071	0.089	0.071	0.071
Charge transfer integrals	Pentacene crystal	Pentacene crystal	Pentacene crystal	Pentacene crystal	Pentacene stack	Pentacene stack	Dipentacene POSS crystal

Figure 3.13. Hole mobility in various combination of site energy difference, reorganization energy and charge transfer integral. The site energy difference of the two molecules is 2×10^{-2} eV, 6×10^{-4} eV, and 2×10^{-4} eV in pentacene crystal unit cell, pentacene stack unit cell, and dipentacene POSS unit cell, respectively. The reorganization energy is 0.089 eV and 0.071 eV for pentacene and dipentacene POSS. The largest charge transfer integral of the hopping dimmers is 136 meV, 306meV, and 205 meV in pentacene crystal, pentacene stack, and dipentacene POSS. Smaller site energy difference and reorganization energy result in higher mobility but the most important contribution to the enhanced mobility is from larger charge transfer integral due to parallel configuration of pentacene segments.

(Figure 3.13). The results in Figure 3.13 clearly point out that, compared to values in pure crystalline pentacene, in dipentacene POSS the site energy difference is smaller, the reorganization energy is smaller, and the charge transfer integrals are larger, all of which contribute to the higher overall hole mobility. The most important contribution originates from higher charge transfer integrals due to the parallel configuration of pentacene segments. The POSS cages in the hybrid molecules do not make direct significant contributions to the high charge mobility. However, its rigidity and three-dimensional structure restricts the orientation of the functional groups. In the case of dipentacene POSS, the pentacene segments adopt a parallel configuration such that the charge transfer integrals are larger than those in the herringbone packing of pristine crystalline pentacene.

3.4. Conclusions

We designed hybrid molecules by functionalizing a POSS cage with pentacene. The electronic structure and properties of the dipentacene POSS molecule are similar to those of pentacene. The possible crystal structures of the hybrid materials are investigated by combining molecular dynamics and density functional theory. The pentacene segments form a parallel configuration in the layered structure of the dipentacene POSS crystal. The simulated hole mobility in dipentacene POSS is about one order of magnitude larger than that in pentacene, reaching 415 cm^2/Vs at 300K. The design principle is to use the rigidity and three-dimensional structure of POSS cage to control the orientation of pentacene segments such that parallel configurations for better wavefunction overlap are adopted. The simulation results for dipentacene POSS shine light on the use of computational materials design at molecular level.

3.5. References

(1) Coropceanu, V.; Cornil, J.; da Silva, D. A.; Olivier, Y.; Silbey, R.; Bredas, J. L. *Chem. Rev.* **2007**, *107*, 926-952.

(2) Yin, S. W.; Yi, Y. P.; Li, Q. X.; Yu, G.; Liu, Y. Q.; Shuai, Z. G. *J. Phys. Chem. A* **2006**, *110*, 7138-7143.

(3) Kim, M. S.; Kim, B. G.; Kim, J. *ACS Appl. Mater. Inter.* **2009**, *1*, 1264-1269.

(4) Chan, C. K.; Zhao, W.; Kahn, A.; Hill, I. G. *Appl. Phys. Lett.* **2009**, *94*,

(5) Shirota, Y.; Kageyama, H. *Chem. Rev.* **2007**, *107*, 953-1010.

(6) Jurchescu, O. D.; Baas, J.; Palstra, T. T. M. *Appl. Phys. Lett.* **2004**, *84*, 3061-3063.

(7) Zhen, C. G.; Becker, U.; Kieffer, J. *J. Phys. Chem. A* **2009**, *113*, 9707-9714.

(8) Zhou, J. H.; Kieffer, J. *J. Phys. Chem. C* **2008**, *112*, 3473-3481.

(9) *al.,* F. M. J. *e*. **2004**,

(10) Stewart, J. J. P. *J. Comput. Chem.* **1989**, *10*, 209-220.

(11) Becke, A. D. *J. Chem. Phys.* **1993**, *98*, 5648-5652.

(12) Francl, M. M.; Pietro, W. J.; Hehre, W. J.; Binkley, J. S.; Gordon, M. S.; Defrees, D. J.; Pople, J. A. *J. Chem. Phys.* **1982**, *77*, 3654-3665.; Hehre, W. J.; Ditchfie, R.; Pople, J. A. *J. Chem. Phys.* **1972**, *56*, 2257-2261.

(13) Sun, H. *J. Phys. Chem. B* **1998**, *102*, 7338-7364.

(14) Cheng, Y. C.; Silbey, R. J.; da Silva, D. A.; Calbert, J. P.; Cornil, J.; Bredas, J. L. *J. Chem. Phys.* **2003**, *118*, 3764-3774.

(15) Wang, L. J.; Nan, G. J.; Yang, X. D.; Peng, Q.; Li, Q. K.; Shuai, Z. G. *Chem. Soc. Rev.* **2010**, *39*, 423-434.

(16) Kwiatkowski, J. J.; Nelson, J.; Li, H.; Bredas, J. L.; Wenzel, W.; Lennartz, C. *Phys. Chem. Chem. Phys.* **2008**, *10*, 1852-1858.

(17) Marcus, R. A.; Sutin, N. *Biochim. Biophys. Acta* **1985**, *811*, 265-322.

(18) Bredas, J. L.; Calbert, J. P.; da Silva, D. A.; Cornil, J. *Proc. Natl. Acad. Sci. U.S.A.* **2002**, *99*, 5804-5809.

(19) Daggett, V.; Kollman, P. A.; Kuntz, I. D. *Biopolymers* **1991**, *31*, 285-304.

(20) Norton, J. E.; Bredas, J. L. *J. Am. Chem. Soc.* **2008**, *130*, 12377-12384.

(21) McMahon, D. P.; Troisi, A. *J. Phys. Chem. Lett.* **2010**, *1*, 941-946.

(22) Coropceanu, V.; Malagoli, M.; da Silva, D. A.; Gruhn, N. E.; Bill, T. G.; Bredas, J. L. *Phys. Rev. Lett.* **2002**, *89*,

(23) Mattheus, C. C.; Dros, A. B.; Baas, J.; Meetsma, A.; de Boer, J. L.; Palstra, T. T. M. *Acta Crystallogr., Sec.C: Cryst.Struct. Commun.* **2001**, *57*, 939-941.

(24) Yang, X. D.; Li, Q. K.; Shuai, Z. G. *Nanotechnology* **2007**, *18*, 424029.

(25) Troisi, A.; Orlandi, G. *J. Phys. Chem. B* **2005**, *109*, 1849-1856.

(26) Varekova, R. S.; Koca, J.; Zhan, C. G. *Int. J. Mol. Sci.* **2004**, *5*, 154-172.

Chapter 4. Material design and device optimization for highly efficient fluorescent blue organic light-emitting diodes

4.1. Introduction

Organic light-emitting diodes (OLEDs) are promising devices for the next generation of flat panel displays and lighting applications.[1-3] High efficiency is required to compete with other technologies such as liquid crystal display and fluorescent tubes. The external quantum efficiency (EQE) of organic light-emitting diodes (OLEDs) can be expressed as:

$$\text{EQE} = \gamma\chi\eta_{pl}\eta_{oc} \tag{4.1}$$

where γ is the recombination efficiency of injected holes and electrons, χ is the fraction of excitons that can potentially radiatively decay due to restriction of multiplicity, η_{pl} is intrinsic photoluminescence (PL) efficiency, and η_{oc} is the light out-coupling factor. Ideally, $\gamma = 1$ if holes and electrons are fully balanced and completely recombine to form excitons. η_{oc} is about 20 ± 2%, which is estimated from ray optics as $\eta_{oc} = 1-(1-1/n^2)^{1/2}$, where n is the refractive index of the organic layers (normally is 1.7 ± 0.1 for organic solids).[4] χ depends on the type of OLEDs, either phosphorescent OLEDs (POLEDs) or fluorescent OLEDs (FOLEDs). The former exploit both triplet and singlet excitons while the latter can only utilize singlet excitons to convert electrical energy to light.[5] According to classical degeneracy statistics, the probability of

generating triplet excitons is 75% while it is 25% for singlet excitons from recombination of injected carriers, assuming the formation cross-sections for triplet and singlet are equal.[6] Therefore, χ for POLEDs is 100% while it is 25% for FOLEDs. Hence, the classical upper EQE limit of FOLEDs is about 5%, whereas that of POLEDs is about 20%. However, there are other advantages that FOLEDs have over POLEDs. First, there are many organic materials that exhibit fluorescence while only very few exhibit phosphorescence around room temperature.[7] Second, the efficiency roll-off at high current density in FOLEDs is less severe than in POLEDs, due to shorter exciton lifetime and less bimolecular quenching.[8-10]

Recent progress in experiments[11,12] and theory[13,14] suggests that the singlet generation probability for conjugated systems can be larger than 25%. Therefore, it is possible for the EQE of FOLEDs to exceed the 5% limit. Actually, to name a few reported occurrences, Wei and Chen has realized sky-blue FOLED with 7.87% EQE by optimizing emitting molecules so as to inhibit intermolecular π-π stacking, which would reduce the efficiency of the OLEDs.[15] Okumoto et al. enhanced the EQE of their doped green FOLEDs from 4.4% to 9.8% by replacing the commonly used electron transporter tris(8-hydroxyquinolinato) aluminium (Alq_3) with 9,10-bis[4-(6-methylbenzothiazol-2-yl)phenyl]anthracene (DBzA).[16] Chen et al. achieved 8% EQE for undoped green FOLED by systematically optimizing the thicknesses of the hole injection layer, hole transporting layer, and electron transporting layer, and by trying various cathodes.[17] The significant implication of these examples and others[18-21] is that it is indeed possible to achieve high efficient FOLEDs through optimization of molecular structures and device configurations. In this chapter, we describe our achievement of a deep blue FOLED with

EQE of 10.7% and CIE coordinates of (0.151, 0.088), which we accomplished by optimizing the molecular structures of emitters, the device design, and the device fabrication process.

The computational materials design described here has been successfully implemented in experiments and has led to the development of new materials that at the time of this writing holds the world record for EQE among blue fluorescent OLEDs. The computational work was carried out at the University of Michigan, while the chemical synthesis, experimental realization and characterization of the device was accomplished in collaboration with a research group at IMRE in Singapore.

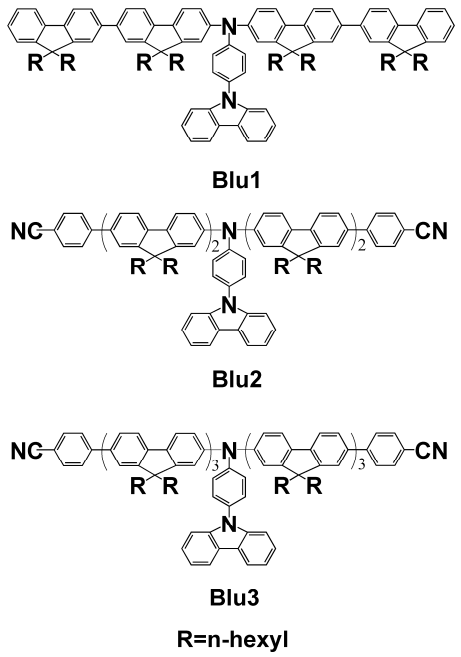

Figure 4.1. Designed molecular structures of the blue emitters. Fluorene oligomers are used as backbone due to their high photoluminescent quantum yield (PLQY), good thermal stability, and excellent solubility. Phenylcarbazole is electron donating group, which is expected to facilitate hole injection and transport. The end-cap group, cyanophenyl, is electron-withdrawing group, which is expected to facilitate electron injection and transport.

4.2. Methods of investigation

4.2.1. Conceptual approach

In Chapter 2 and Chapter 3, we have concluded that electronic properties of molecules are greatly influenced by functional groups. For instance, an electron

donating group can enhance the energy level of the highest occupied orbital (HOMO) and electron withdrawing groups can lower the energy level of the lowest unoccupied orbital (LUMO). Another finding is that the reorganization energy can affect the charge mobility. Keeping these in mind, we analyze an existing molecular design structure of Blu1 and optimized it to molecules Blu2 and Blu3 by adding key functional groups (Figrue 4.1), which were computationally predicted for superior properties related to OLEDs. This approach allows us to identify trends and fundamental knowledge that can serve as general design criteria for OLEDs with improved performance characteristics. Further optimization was also achieved at the device level.

4.2.2. Computational details

We carried out first-principles density functional theory (DFT) and the time-dependent DFT (TDDFT) calculations to determine the electronic structure and carrier properties of the blue emitting molecules. We used the B3LYP exchange-correlation functional[22] and 6-31G* basis set implemented in the Gaussian 03 package.[23] To predict the performance of the various molecular architectures we explored computationally several key properties pertaining to energy conversion in OLEDs have been evaluated as follows:

Carrier injection barriers — The hole and electron injection barriers are determined by comparing the work functions of anode and cathode with the energy level of HOMO and LUMO.

Carrier transport properties — The carrier transport properties are studied in the framework of Marcus' electron transfer model.[24] According to Marcus' model, the

conductivity of amorphous organic materials depends on the electron (or hole) transfer reactions between two adjacent molecules (hopping sites), represented by M_1 and M_2

$$M_1^{+/-} + M_2 \rightarrow M_1 + M_2^{+/-}. \tag{4.2}$$

The corresponding hopping rate can be described by Marcus' equation:

$$k_{et} = \frac{2\pi}{\hbar} \frac{H_{da}^2}{\sqrt{4\pi\lambda kT}} \exp(-\frac{(\Delta G + \lambda)^2}{4\lambda kT}), \tag{4.3}$$

where λ is the reorganization energy, H_{da} the charge-transfer integral, k is Boltzmann's constant, ΔG is the free energy change for the electron transfer reaction, and T is the temperature. The charge transfer integral originates from the overlap of wavefunctions between the hopping sites, which is determined by the relative positions and the spatial wavefunction patterns of the molecules. In amorphous organic solids, H_{da} can be expected to constitute a less variable quantity due to the random packing of molecules. Reorganization energy represents the activation barrier from the configurational adjustment of molecules during charge transfer. The reorganization energy λ consists of inner reorganization energy and external polarization due to the solvent effects of the surrounding medium. Here we only consider inner reorganization energy since the external reorganization energy has been demonstrated to be negligibly small compared with inner reorganization energy.[25,26] The inner reorganization energies are obtained by comparing the energies in charged and uncharged optimized configurations, for both neutral and ionized states, i.e.,

$$\lambda = E_{\pm}^0 - E_{\pm}^{\pm} + E_0^{\pm} - E_0^0 \tag{4.4}$$

where $E_{\pm}^{0}$ is the energy of the ion in the optimized uncharged geometry, $E_{\pm}^{\pm}$ is the energy of the ion in the optimized charged geometry, $E_{0}^{\pm}$ is the energy of the neutral molecule in the optimized charged geometry, and E_{0}^{0} is the energy of the neutral molecule in the optimized uncharged geometry.

Singlet generation fraction — χ of FOLEDs, also referred as singlet generation fraction, is calculated from Shuai's method based on Fermi's golden rule:[27]

$$\chi_S = \sigma_S / (\sigma_S + 3\sigma_T) \tag{4.5}$$

$$\frac{\sigma_S}{\sigma_T} = \frac{E_{bT}}{E_{bS}} \tag{4.6}$$

where $_S$ and $_T$ represent the formation cross sections of singlet and triplet excitons, E_{bS} and E_{bT} are the binding energies of the singlet and triplet excitons, respectively. E_{bS} and E_{bT} are calculated from DFT and TDDFT as[28]

$$E_{bS} = E_g - E_{S1} \tag{4.7}$$

$$E_{bT} = E_g - E_{T1}\ , \tag{4.8}$$

where E_g is HOMO-LUMO energy gap, while E_{S1} and E_{T1} are the excitation energies from the ground state to the lowest excited singlet state and the lowest excited triplet state, respectively. To reduce the computational time, hexyl was replaced by a methyl group in the oligomers. It is known that this does not affect the optical and electronic properties significantly.[29]

4.2.3. Experimental details

Chemicals — The synthesis of the emitters was described in literature.[30] Poly(3,4-ethylenedioxythiophene) (PEDOT) doped with poly(styrenesulfonate) (PSS), was purchased from Bayer, Germany. The host material, poly(9-vinyl carbazole) (PVK) (Mn~ 1000000), was purchased from Aldrich. Another host material, 4,4'-bis(carbazol-9-yl)biphenyl (CBP), and an electron transport and hole blocking material, 1,3,5-tris(phenyl-2-benzimidazolyl)benzene (TPBI), were purchased from Lumtec Corp., Taiwan. All these materials were used without further purification for device fabrication.

Instruments — Nuclear magnetic resonance (NMR) spectra were collected on a Bruker DPX 400 M Hz spectrometer using chloroform-d as a solvent and tetramethylsilane (TMS) as an internal standard. Cyclic voltammetry (CV) experiments were performed on an Autolab potentiostat (model PGSTAT30). All CV measurements were recorded in dichloromethane with 0.1 M tetrabutylammonium hexafluorophosphate as supporting electrolyte (scan rate of 50 mV/s) using a conventional three electrode configuration consisting of a platinum wire working electrode, a gold counter electrode, and a Ag/AgCl in 3 M KCl reference electrode. The measured potentials were converted to SCE (saturated calomel electrode) and the corresponding ionization potential (IP) and electron affinity (EA) values were derived from the onset reduction-oxidation (redox) potentials, based on -4.4 eV as the SCE energy level relative to vacuum (EA = E_{red}-onset + 4.4 eV, IP = E_{ox}-onset + 4.4 eV). The photoluminescent spectra of the solutions and solid films were recorded by a PerkinElmer LS55 fluorescence spectrometer. The plasma treatment on the ITO substrate was done in a Trion Sirns RIE Etch System. Spin-coating of the

hole injection layer and the emitting layer was performed with a CEE 100 spin coater. The thickness of the spin-coating layers was measured by a Tencor P-10 Alpha step profiler. The thickness of thermally evaporated layers of electron injection/hole blocking layer and cathodes was monitored by a quartz crystal microbalance. The current–voltage–luminance (I-V-L) characteristics of the devices were recorded using a Keithley 2420 source meter, Keithley 2400 multimeter, and a silicon photodiode calibrated by Minolta CS-200 Chromameter. Electroluminescent spectra of the devices were recorded with an Ocean Optics USB2000 miniature fiber optic spectrometer. Time-resolved photoluminescence was excited by femtosecond laser pulses (~150 fs) generated from an optical parametric amplifier pumped by a 1 kHz regenerative amplifier, and was recorded by a streak camera system.

Device fabrication and characterization — The emissive layer is spin-coated from solution. Specifically, for undoped devices, the emitting materials were dissolved in toluene at concentration of 10 mg/ml. For doped devices using PVK as host, dopant and PVK were dissolved in ethyl benzoate at a concentration of 5 mg/ml. For devices using CBP as host, dopant and CBP were dissolved in chloroform at a concentration of 5 mg/ml. By controlling the weight ratio of the dopant and host in solution, we can control the concentration of emitter molecules in the host in the final solid devices. All these solutions were stirred in an argon atmosphere overnight in darkness. The thickness of conductive ITO is about 110 nm with resistance of about 20 Ω/square on glass that is used as substrate for OLEDs. ITO substrates were cleaned using detergent, de-ionized water, acetone, ethanol in ultrasonic for 5 minutes, sequentially. To enhance the work function and improve the surface smoothness, the ITO surface was treated in argon-

oxygen plasma for 10 minutes under RIE power of 100 watts with oxygen flow of 30 sccm and argon flow of 30 sccm at pressure of 350 mTorr. PEDOT:PSS was spin-coated to form a hole injection layer of about 50 nm for all the devices, followed by drying at 120C in air for 15 min. The solution containing emitting materials was filtered through a 0.2 micron PTFE filter immediately before spin coating. By varying the spin rate, we can control the thickness of emitting layer in the devices. After spin coating, the substrates with the spin-coated layers were transferred to a chamber under vacuum of 1×10^{-5} Pa. A layer of 30 nm thick TPBI was deposited onto the surface of the emitting layer for electron injection and hole blocking. The cathode was composed of 0.5 nm LiF and 150 nm Al, which were thermally deposited consecutively. All the measurements on devices were carried out in air at room temperature without device encapsulation. The external quantum efficiencies were calculated using I-V-L data and EL spectra of the devices, assuming Lambertian distribution of the EL emission.[31]

4.3. Results

We compare the performance of devices based on different molecular architectures, labeled Blu1, Blu2, and Blu3, of which the second and third are resulted from simulation-based design optimization. The computational results are listed in Table 4.1, and the key device characteristics are summarized in Table 4.2.

Table 4.1. Calculation results of Blu1, Blu2, and Blu3 at B3LYP/6-31G* level

	LUMO (eV)	HOMO (eV)	E_g (eV)	λ_- (eV)	λ_+ (eV)	E_{bS} (eV)	E_{bT} (eV)	χ (%)
Blu1	-1.36 (-2.12)	2.841 (-5.08)	3.44 (2.96)	0.232	0.172	0.418	0.996	43.2
Blu2	-1.86 (-2.31)	2.790 (-5.12)	3.06 (2.81)	0.183	0.147	0.275	0.689	45.5
Blu3	-1.84 (-2.16)	2.808 (-5.05)	3.01 (2.89)	0.154	0.133	0.199	0.628	51.3

Parenthetical data are from experiments: E_g were calculated from the onset of UV-Vis spectra; HOMO values were determined by the onset of CV measurements, and LUMO values were calculated from HOMO values and E_g.

Table 4.2. Summary of device performances of ITO/PEDOT:PSS(50nm)/EML/TPBI(30nm)/LiF(0.5nm)/Al(150nm)

Device	EML	Turn on Voltage [V]	Maximum Current Efficiency[cd/A] and EQE [%] @ I_d [mA/cm^2] [a]	Current Efficiency [cd/A] and EQE (%) @ I_d [mA/cm^2] [a]	Power Efficiency [lm/W] @ 100 cd/m^2	CIE (x, y)
1	Blu1(70nm)	3.4	1.83, 2.00 @ 4.57	0.49, 0.53 @ 113	0.89	(0.151, 0.097)
2	Blu2(87nm)	3.1	9.51, 4.99 @ 16.3	7.62, 4.00 @ 187	4.82	(0.161, 0.314)
3	Blu3(60nm)	3.0	5.11, 4.5 @ 7.99	3.65, 3.21 @ 100	3.56	(0.150, 0.148)
4	Blu2(39nm)	2.9	10.76, 5.80 @ 7.56	8.50, 4.58 @ 99.3	6.42	(0.159, 0.303)
5	Blu2(60nm)	3.0	11.16, 6.12 @ 4.44	8.78, 4.81 @ 113	7.23	(0.148, 0.280)
6	Blu2(100nm)	3.4	6,80, 3.85 @ 14.4	6.33, 3.58 @ 95.7	3.65	(0.144, 0.279)
7	Blu2(60nm) Annealed	3.1	13.27, 7.40 @ 6.39	9.24, 5.16 @ 103	8.55	(0.149, 0.292)
8	PVK:2% Blu2(60nm)	5.5	2.64, 2.71 @ 0.04	1.29, 1.33 @ 95.1	0.70	(0.147, 0.135)
9	CBP:2% Blu2(60nm)	3.9	6.40, 6.88 @ 1.00	4.20, 4.51 @ 104	3.05	(0.147, 0.119)
10	CBP:4% Blu2(60nm)	4.0	8.77, 8.60 @ 1.23	5.67, 5.56 @ 109	4.28	(0.149, 0.132)
11	CBP:6% Blu2(60nm)	3.9	10.08, 9.40 @ 0.69	5.48, 5.11 @ 110	4.29	(0.147, 0.139)
12	CBP:8% Blu2(60nm)	4.2	9.11, 8.07 @ 1.04	6.27, 5.55 @ 99.9	4.34	(0.147, 0.149)
13	CBP:10% Blu2(60nm)	3.9	8,88, 7.26 @ 0.88	6,30, 5.15 @ 96.5	4.51	(0.149, 0.166)
14	CBP:2% Blu3(60nm)	5.5	7.74, 10.7 @ 47.2	6.46, 8.93 @ 122	1.75	(0.151, 0.088)

[a] The first number is current efficiency, the second number is EQE, the third number is current density. I_d, current density.

The starting point, Blu1, consisted of an electron-donating group, 4-carbazolephenyl incorporated into the backbone of oligofluorene to facilitate hole injection and thereby reduce the operating voltage.[32] We fabricated an undoped device using Blu1 as emitting layer (EML) with the configuration: ITO/ PEDOT:PSS/ Blu1 (70nm) / TPBI/ LiF/ Al (Device 1). The turn on voltage, at which the brightness reaches 1 cd/m^2, is 3.4 V, which is acceptable. However, its EQE is not satisfactory. The maximum EQE is only 2.0% at 4.57 mA/cm^2 (84 cd/m^2) and drops to 0.53% at 113 mA/cm^2 (554 cd/m^2).

To understand the reason for the low EQE, we carried out first-principles calculations of Blu1 in vacuum state. The LUMO is calculated to be –1.36 eV while the HOMO is –4.80 eV. The work function of the device anode (ITO/ PEDOT:PSS) is about 4.8 eV. Hence, the injection barrier for hole is expected to be small. The work function of the device cathode (Al) is about 4.1 eV, which creates a high barrier for electron injection even though we use LiF and TPBI to aid electron injection. We also calculate the reorganization energy associated with the charge transport barriers for hole and electron hopping between Blu1 molecules. The reorganization energy for hole hopping, λ_+, is 0.172 eV while the one for electron hopping, λ_-, is 0.232 eV. The higher barriers of injection and transport for electrons compared to those for holes leads to a low balance factor γ, which reduces the EQE. To solve this problem and make injection and transport of electrons easier, we modified the molecular structure of Blu1 by adding electron-withdrawing groups, 4-cyanophenyl, constructing Blu2 and Blu3.

Using the same calculation approach as before, we determined the LUMO of Blu2 and Blu3 to be –1.86 eV and -1.84 eV in vacuum, respectively, which are ~ 0.50 eV lower

than that of Blu1. Experimentally, the LUMO for Blu1, Blu2, and Blu3 are –2.12 eV, –2.31 eV, and -2.16 eV, respectively, as determined from the onset voltage of cyclovoltammetry (CV) measurements and optical gaps. Thus, the calculation results are in qualitative agreement with the experimental results. The lower LUMO is expected to lower the electron injection barrier. The reorganization energies of Blu2 for hole hopping and electron hopping are 0.147 eV and 0.183 eV, respectively. For Blu3, the reorganization energies for hole hopping and electron hopping are 0.133 eV and 0.154 eV. Both λ_+ and λ_- of Blu2 and Blu3 are smaller than those for Blu1, indicating that Blu2 and Blu3 may be a better carrier transporter than Blu1. More importantly, the difference between λ_+ and λ_- for Blu2 and Blu3 is smaller than that for Blu1, which is expected to lead to more balanced carrier transport.

To test our prediction of the charge transport properties of Blu1 and Blu2, we fabricated hole-only and electron-only devices to obtain hole and electron mobility by using the space-charge limited current (SCLC) method[33] with device configurations of ITO/ Blu1 or Blu2 (100nm)/Ag and ITO/Ca(20nm)/Blu1 or Blu2 (100nm)/Ca(20nm)/Ag, for hole-only and electron-only devices, respectively. The mobility were determined by fitting the current to the model of a single carrier SCLC, which is described as

$$J = \frac{9}{8}\varepsilon_0\varepsilon_r\mu_0\frac{V^2}{L^3}, \tag{4.9}$$

where J is the current density, μ_0 is the zero-field mobility, ε_0 is the permittivity of free space, ε_r is the relative permittivity of the material (assumed to be 3 for organic materials), L is the thickness of the organic layer, and V is the applied voltage. The J-V^2 plots for the

devices are shown in Figure 4.2. Hole mobility of Blu1 and Blu2 are found to be 4.1 × 10^{-5} and 5.3 × 10^{-5} cm^2/Vs. Amazingly, we find the electron mobility of Blu2 to be 4.0 × 10^{-7} cm^2/Vs, 36 times larger than that of Blu1, 1.1 × 10^{-8} cm^2/Vs, confirming the importance of the reorganization energy in controlling charge transport, as discussed above. In Chapter 2, we have observed that for organic semiconductors with similar molecular structures, the conductivity is closely related to reorganization energy. Smaller reorganization energy corresponds to higher conductivity if the charger transfer integrals are similar during charge hopping process. Though we cannot quantify the charge transfer integrals in Blu1 and Blu2 films, we can expect H_{da} to constitute a less variable quantity due to the random packing of molecules in amorphous organic solids.

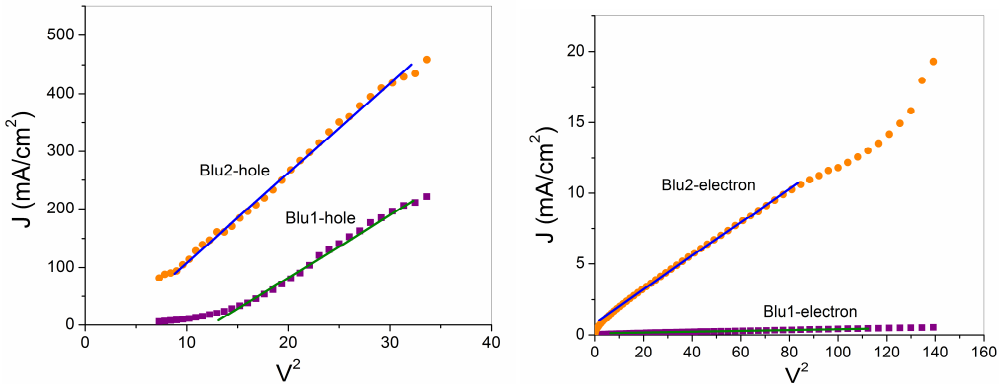

Figure 4.2. J-V^2 characteristics of devices of ITO/Blu1 or Blu2 (100 nm)/Ag (top) and ITO/Ca(20 nm)/Blu1 or Blu2 (100 nm)/Ca(20 nm)/Ag (bottom). The solid lines represent best fits to eq. (9). Hole mobility of Blu1 and Blu2 are found to be 4.1 × 10^{-5} and 5.3 × 10^{-5} cm^2/Vs. Electron mobility of Blu1 and Blu2 are 1.1 × 10^{-8} cm^2/Vs and 4.0 × 10^{-7} cm^2/Vs.

Comparing our calculation results for these blue emitters, we anticipate a higher balance factor for Device 2, which contains an 87 nm thin film of Blu2 as emitting layer,

and Device 3, which contains a 60 nm thin film of Blu3 as emitting layer, in a configuration similar to that of Device 1.

As expected, the performances of Device 2 and Device 3 are much better than Device 1. Not only is the EQE of Device 2 and Device 3 higher, but the efficiency roll-off is also improved with respect to Device 1 (Figure 4.3). Device 2 shows a maximum EQE of 4.99% at 16.3 mA/cm^2 (1552 cd/m^2) and drop to 4.00% at high current density of 187 mA/cm^2 (14243 cd/m^2). The performance of Device 3 is also better than Device 1. The maximum EQE is 4.50% at 7.99 mA/cm^2 (408 cd/m^2) and drop to 3.21% at 100 mA/cm^2 (3661 cd/m^2). In contrast, the efficiency of Device 1 began to drop off severely at about 10 mA/cm^2. The efficiency roll-off at high current density originates from exciton quenching or unbalance of carriers in the emitting layer.[8] The better efficiency roll-off of Device 2 and Device 3 at high current density indicates that quenching of excitons is small and balanced charge injection and transport in the emitting layer of Blu2

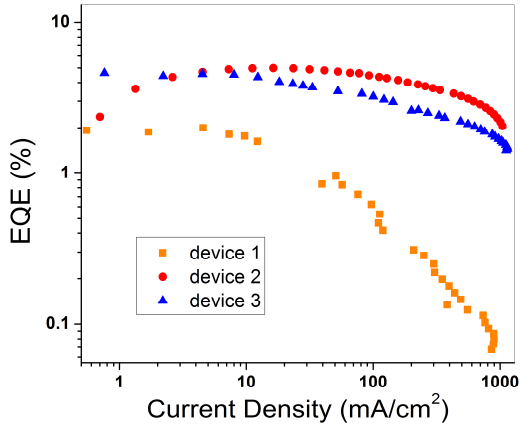

Figure 4.3. Comparison of EQE of Device 1 (EML = 70 nm Blu1), 2 (EML = 87 nm Blu2), and 3 (EML = 60 nm Blu3), as a function of current density with device configuration of ITO/PEDOT:PSS(50nm)/ EML/ TPBI(30nm)/ LiF(0.5nm)/ Al(150nm). The better efficiency roll-off for Device 2 and 3 indicates quenching of excitons at high current density is small and hole/electorn in the emitting layer of Blu2 and Blu3 are balanced even at high electric field.

and Blu3 prevail even at high electric field. Therefore, the optimized molecular structure of the emitters leads to higher EQE and better device performance at high current density.

The power efficiency of Device 2 (4.82 lm/W) and Device 3 (3.56 lm/W) are much larger than Device 1 (0.89 lm/W) at 100 cd/m^2 (Table 4.2). This is not only because the EQE of Device 2 (3.70%) and Device 3 (4.44%) are larger than that of Device 1 (1.92%) but also the driving voltage of Device 2 (4.6 V) and Device 3 (4.5 V) are lower than that of Device 1 (6.2 V) at 100 cd/m^2. This is reasonable since the reorganization energies of Blu2 and Blu3 are much smaller than those of Blu1, for both hole and electron hopping. During the hopping process, holes and electrons experience smaller energy barriers in Blu2 and Blu3 than in Blu1. Therefore, driving voltages for Device 2 and Device 3 are lower than that for Device 1. Since the performance of Blu2 is better than Blu1 and Blu3, we focus on device optimization for Blu2 in the following discussion.

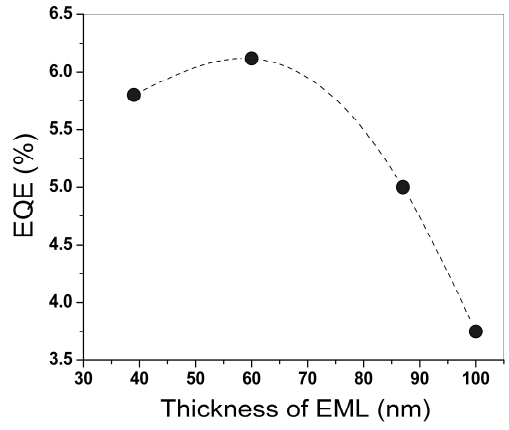

Figure 4.4. The correlation between EQE and thickness of undoped devices using Blu2 as emitting layer. Device configuration is ITO/PEDOT:PSS(50nm)/ EML (Blu2 = 39nm, 60nm, 87nm, 100nm)/ TPBI(30nm)/ LiF(0.5nm)/ Al(150nm).

Further improvement of the device performance could be achieved by varying thickness of EML. We fabricated devices with 39 nm (Device 4), 60 nm (Device 5), and 100 nm (Device 6) EML thickness. The quantum efficiency strongly depends on this thickness (Figure 4.4). The best performance comes from Device 5 with a

maximum EQE of 6.12% at 4.44 mA/cm^2 (496 cd/m^2) and drops to 4.81% at high current density of 113 mA/cm^2 (9950 cd/m^2). It is possible that the variation of efficiency in devices with EML of different thickness is due to the variation of diffusion of carriers inside EML. [34] For thinner EML, a significant fraction of injected holes diffuse out of the EML without recombining with electrons, thus reducing the recombination efficiency and the overall EQE. [34] For thicker emitting layer, part of holes will be trapped in the EML far from the electron rich region and undergo non-radiative recombination.[34] A similar analysis applies to electrons injected from electron transport layer. The dependence of EQE on thickness indicates that the overlap region where electrons and holes can recombine efficiently is about 60 nm in thickness.

The stability of Blu2 is also very encouraging. For comparison, Device 7 with 60 nm spin-coated Blu2 layers was annealed at 120 C (T_g = 101.7 C) in air for 2 hours before depositing TPBI. The EL spectrum of the annealed device is almost the same as the unannealed one (Figure 4.5), indicating the emitting material is very stable to oxidation and attack by moisture, which is important to prevent degradation in applications demanding long term operation. Actually, the device efficiency is even higher with the thermal aging treatment compared with Device 5,

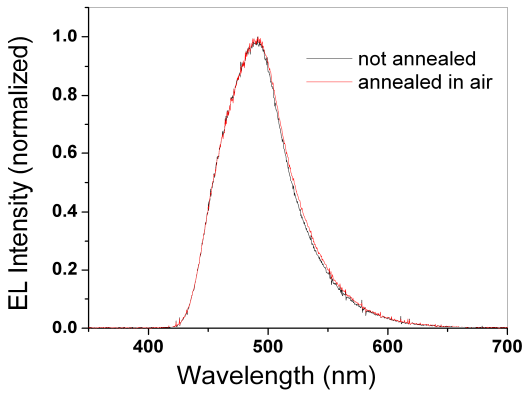

Figure 4.5. The EL spectrums of Device 5 and Device 7 comprising EML unannealed (black) and annealed in air at 120C for 2 hours (red). The same EL spectrums for annealed and unannealed device indicates very good stability against oxygen and moisture in air.

which contains an unannealed EML. The maximum EQE of Device 6 is 7.40% at 6.39 mA/cm^2 (848 cd/m^2) and drops to 5.16% at 103 mA/cm^2 (9493 cd/m^2). A possible reason for the better performance of Device 7 is that the annealing reduces the morphology defects such as pinholes in the emitting layer, as uniformity of the organic layers is essential for organic light-emitting diodes.[35] Indeed, the surface morphology study using atomic force microscopy (AFM) of the annealed and unannealed EML before deposition of TPBI reveals that the annealing treatment can improve the uniformity of the films (Figure 4.6), reducing the surface roughness amplitude from 6.79 nm to 3.11 nm.

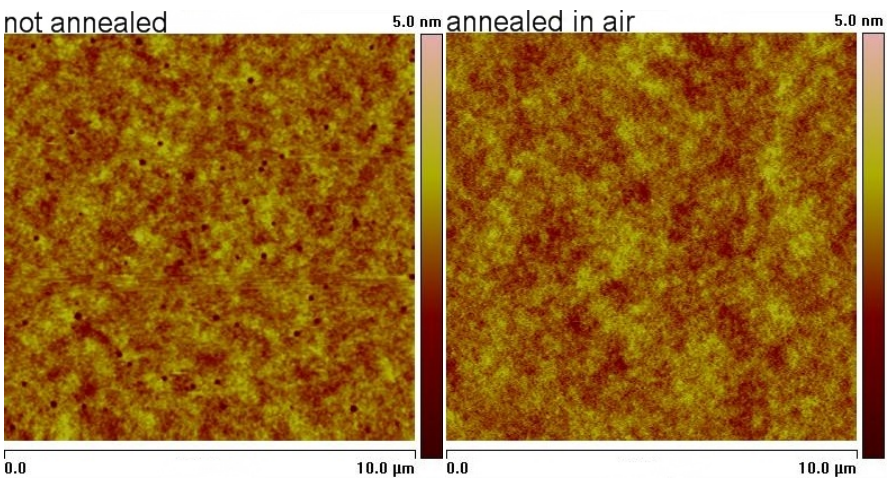

Figure 4.6. The surface morphology of EML before deposition of TPBI. Top: unannealed EML with a surface roughness amplitude of 6.79 nm. Bottom: EML annealed in air at 120C for 2 hours with a surface roughness amplitude of 3.11 nm. Thermal treatment reduces the surface roughness, and makes contribution to higher device performances.

Although the efficiency of Device 7 is quite high, the color of the emission is sky-blue with CIE coordinate (0.149, 0.292), which falls out of the range of pure blue color with CIE $x + y < 0.30$. The emission peak is at 493 nm and is significantly red-shifted compared to the PL emission of the molecule in dilute toluene solution at concentration

of 2 × 10^{-6} mol/l, which is at 437 nm. The difference between PL emission from a dilute solution and EL emission from the solid state under an electric field implies that the interaction between emitting molecules in the solid state is strong. To further improve the performance of the device, especially to bring its color into the pure blue range, we created EML materials that consist of 2% (w/w) Blu2 doped into an appropriate host material, designed to reduce the interactions between the emitting molecules, while preserving the overall configuration of Device 7. We tested two materials as host: polymeric PVK for Device 8 and small molecular CBP for Device 9. There is good overlap between the PL spectra of the chosen hosts and the absorption of the dopant (Figure 4.7). Therefore, the Förster energy transfer from host to dopant is expected to be efficient.

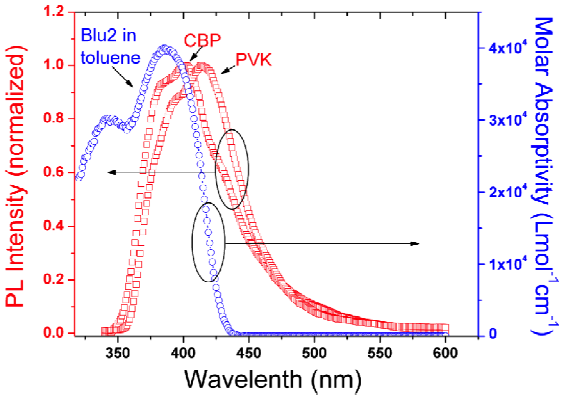

Figure 4.7. The absorption spectrum of Blu2 in toluene and photoluminescence spectra of CBP and PVK films. CBP film was thermally deposited and PVK film was spin-coated from ethyl benzoate. The good spectrum overlapping between hosts and dopant ensure efficient energy transfer from hosts to dopant.

The emission from Device 8 is in the range of pure blue with CIE coordinate (0.147, 0.135), and the maximum EQE is 2.71%. The turn on voltage is 5.5 V, much higher than Device 7 using non-doped Blu2 as emitting layer. Compared to Device 8, the performance of Device 9 is much better. The CIE coordinate of the emission is (0.147, 0.119), within the range of pure blue. The maximum EQE is 6.88% at 1.0 mA/cm^2 (64 cd/m^2) and drops to 4.51% at 104 mA/cm^2 (4389 cd/m^2). The poor performance of the

device using PVK as host material compared the one using CBP may have several underlying reasons. First, consider the spectral overlap integral (J), which determines the efficiency of energy transfer from host to dopant. It can be calculated as[36]

$$J = \frac{\int_0^\infty \lambda^4 f_D(\lambda)\varepsilon_a(\lambda)d\lambda}{\int_0^\infty f_D(\lambda)d\lambda} \tag{4.10}$$

where f_D is the normalized PL spectrum of donors (PVK or CBP) and ε_a is the molar extinction coefficient of the acceptor (Blu2). The calculated spectral overlap integral between CBP and Blu2 is 5.15×10^{14} L mol^{-1}cm^{-1}nm^{-4}, 11.4% larger than between PVK and Blu2, which is 4.63×10^{14} L mol^{-1}cm^{-1}nm^{-4}. The second reason is the poor electron injection and transport capability of PVK due to its low electron affinity (EA) and its poor electron mobility. Third, the exciton lifetime of PVK is orders of magnitude shorter than that of CBP such that the excitons generated in the PVK host cannot completely transfer to the dopant molecules before they decay to their ground state.[37]

The efficiency of doped Device 9 is a little lower than that of undoped Device 7. This is probably due to the incomplete transfer of the excitation energy from the host to the dopant. To find ways for improving the efficiency of the doped devices, we investigated the energy transfer efficiency as a function of doping concentration of Blu2 in CBP. Based on Förster's formulation, the critical distance R_0 at which 50% of the excitation energy is transferred from the donor to acceptor is

$$R_0 = \left(\frac{9(\ln 10)\kappa^2 Q_d J}{128\pi^5 n^4 N_A} \right)^{\frac{1}{6}} \tag{4.11}$$

where κ^2 is the orientation factor determined by the angle between donor and acceptor dipoles, Q_d the PL efficiency of the donor in the absence of acceptor, J spectral overlap integral, n the refractive index of the medium containing donor and acceptor, and N_A Avogadro's number. In the host-dopant system, κ^2 equals 2/3, assuming the host and dopant molecules are oriented randomly, Q_d is 0.61 for CBP,[38] J is calculated as reported above, and n is about 1.8 for CBP.[39] We obtain R_0 = 34.8 Å. In a simplified model, if we assume that every dopant molecule is surrounded isotropically by host molecules to form a sphere, we can define the critical dopant concentration C_0 for which a 50% excitation energy transfer is expected from the surface of the sphere, as the reciprocal of the volume of a sphere of radius R_0, i.e., expressed as a mass fraction,

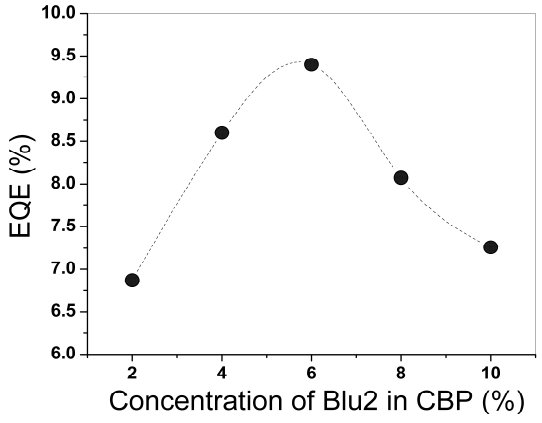

Figure 4.8. The maximum EQE as a function of doping concentration of Blu2 in CBP host.

$$C_0 = \frac{m_{dopant}}{\frac{4}{3}\pi R_0^3 \rho_{host}} \tag{4.12}$$

where m_{dopant} is the mass of a dopant molecule, and ρ the density of the host (about 1.3 g/cm^3 for CBP[40]). Using the calculated R_0, we find C_0 = 1.3%. For efficient energy transfer from CBP to Blu2, the doping concentration should not be less than C_0. We prepared EML layers with doping concentrations of 4%, 6%, 8%, and 10% for Devices 10 through 13, respectively. The corresponding CIE coordinates are (0.149, 0.132),

(0.147, 0.139), (0.147, 0.149), and (0.149, 0.166). All the emissions are in range of, or very close to, pure blue color. The best device performance comes from Device 10 with doping concentration of 6% (Figure 4.8), which shows the highest maximum EQE of 9.40% at 0.69 mA/cm^2 (69 cd/m^2) and still maintains 5.11% at 110 mA/cm^2 (6055 cd/m^2).

As expected, increasing the doping concentration from 2% to 6% enhances the EQE of these devices due to a more efficient energy transfer from the host to the dopants. However, further increase of the doping concentration induces a lower EQE. The decline in EQE may come from non-radiative quenching due to the aggregation of dopant molecules at high doping concentrations.[41] Indeed, we observe that the component of the spectra at long wavelengths increases significantly as the doping concentration exceeds 6% (Figure 4.9), which is a signal of aggregation of the emitting molecules.[42]

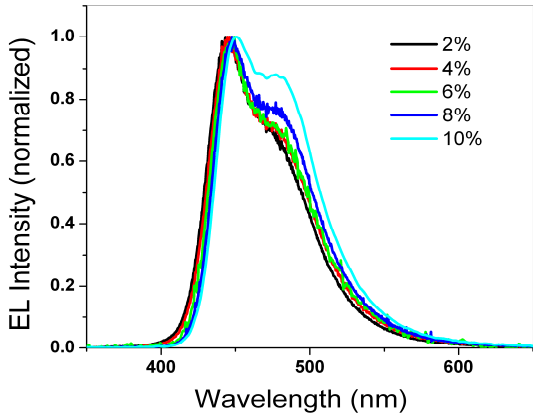

Figure 4.9. EL spectra of devices with different doping concentration of Blu2 in CBP host. The incearsing component of the spectra in long wavelength with larger doping concentration indicates the aggregation of emitting molecules.

We also used CBP as host for Blu3. By using the method described above, we determined the spectral overlap integral between CBP and Blu3 as 2.47 × 10^{15} L $mol^{-1}cm^{-1}nm^{-4}$, nearly 5 times of that between CBP and Blu2, which is mainly due to higher molar absorptivity (Figure 4.10). The critical distance R_0 between CBP and Blu3 is 45.1 Å and the critical dopant concentration C_0 is 2.2%. By doping 2% Blu3 in CBP host as emitting layer, we get Device 14, which has very good performance. The maximum EQE is 10.7% at 47.2 mA/cm2 (3650 cd/m2), and maintains as 8.93% at

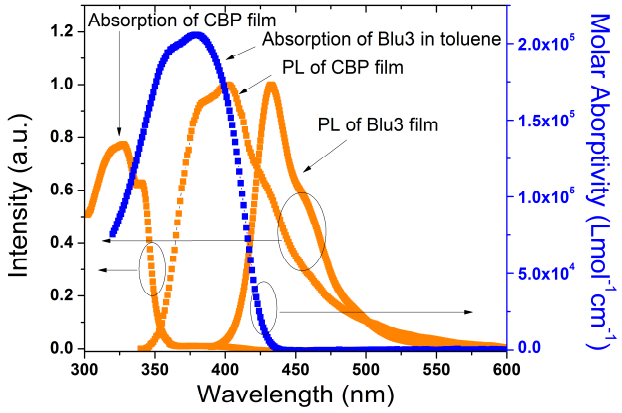

Figure 4.10. The absorption and photoluminescence spectrum of Blu3 and CBP.

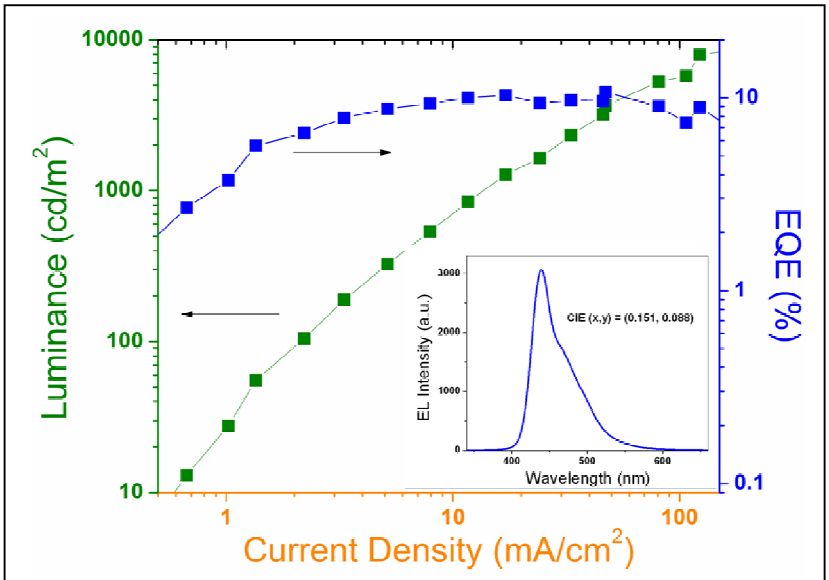

Figure 4.11. The performance and EL spectrum of Device 14 with configuration of ITO /PEDOT:PSS(50nm)/2% Blu3 in CBP (60nm) /TPBI(30nm) /LiF(0.5nm) /Al(150nm).

123 mA/cm2 (7928 cd/m2). The CIE coordinate of the emission is (0.151, 0.088), in the deep blue region (Figure 4.11).

4.4. Discussion

Some of the EQEs of the devices are much higher than the 5% limit for fluorescent OLEDs. Note that we have reproduced the EQE of 1.2% (3.9 cd/A) from controlled OLED with configuration of ITO/NPB(40nm)/Alq(50nm)/LiF(0.5nm)/Al(150nm), using the same ITO glass substrates and the same equipments for processing and measuring the present blue OLEDs. The value is in line with reported Alq_3-based OLEDs. We also fabricated an electrophosphorescent device using bis(2-phenylpyridine)(acetylacetonate)iridium(III) ($Ir(ppy)_2(acac)$) doped in CBP at concentration of 10% to replace the blue emitters as emitting layer in the same configuration as the blue devices. The EQE of the electrophosphorescent device is determined to be 11.3%, which is consistent with reported values.[43] Therefore the high EQE of the blue devices are not due to the refractive index of the organic materials or ITO glass substrates used. To understand the origin of the high EQE of our devices, especially device 14, we need to examine the factors in equation (4.1).

4.4.1. PL efficiency

We determined η_{pl} for thin films of 2% Blu3 doped in CBP host using an integrating sphere.[38] The PL efficiency of this solid thin films is 95 ± 5%.

4.4.2. Out-coupling efficiency

Numerical simulation shows that the out-coupling efficiency strongly depends on the orientation of emitting dipoles in OLEDs.[44] Long linear-shape and planar molecules prefer horizontally oriented in thin films while small bulky molecules such as Alq_3 and CBP are randomly oriented (corresponding 66.7% parallel dipole component and 33.3% perpendicular dipole component).[45,46] Molecular orientation also depends on fabrication conditions such as substrate and temperature.[47] Furthermore, the orientation of the dopant molecules are not determined by the orientation of the host molecules.[46] Therefore, it is better to determine the dipole orientation in the exact configuration and working conditions of device. Since the angular emission profile depends on dipole orientation, we can compare the measured angular emission of our Device 14 with optical modeling to determine the dipole orientation and out-coupling efficiency.

The optical modeling is based on CPS theory[48] solved by dyadic Green's functions.[49] The MATLAB code is from the authors of reference[49] and modified specifically for Device 14. In the simulation, we assumed a linear exciton distribution in the emitting layer, *i.e.*, the exciton density is zero at the interface of EML/PEDOT:PSS and linearly increase to maximum at the interface of EML/TPBI. The assumption is based on the theory that due to the hole and exciton blocking effect of TPBI, excitons are mainly formed at the interface of EML/TPBI and diffuse to the EML layer. The measured emission profile and the simulated profile are shown in Figure 4.12. The best fit between experimental and simulated achieved for 50±5% parallel dipole component, corresponding to which the out-coupling efficiency is 18±2%.

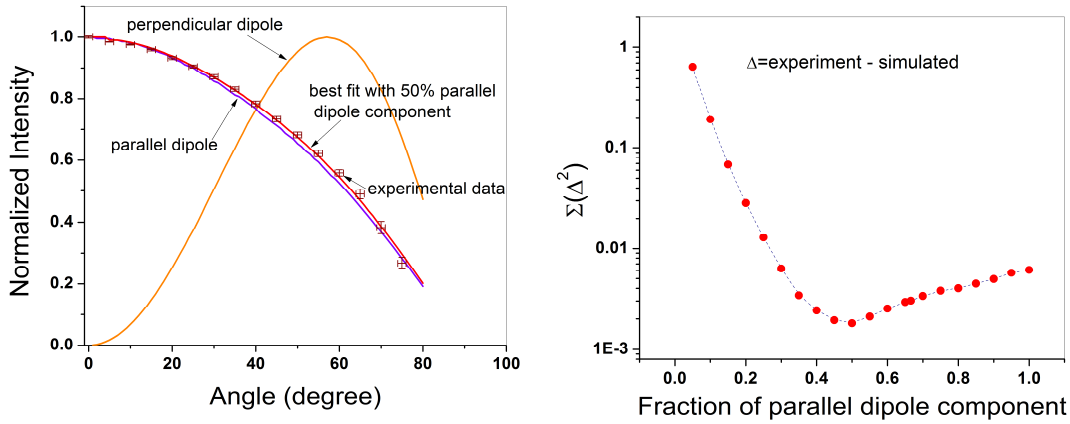

Figure 4.12. (Left) Comparison between the measured and simulated emission profile for ITO/PEDOT:PSS(50nm)/2% Blu3 in CBP/(60nm)/TPBI(30nm)/LiF(0.5nm)/Al(150nm). (Right) The fitting residue as a function of parallel dipole component fraction. The best fit is from simulated emission profile based on 50% parallel dipole component, which corresponding to out-coupling efficiency of 18%.

4.4.3. Singlet generation fraction

The other important factor, χ, is the singlet exciton generation fraction in FOLEDs. The singlet exciton can be generated directly from the recombination of injected carriers or from Triplet-Triplet (T-T) annihilation:[50]

$$^{3}\mathrm{Blu3}^{*} + {}^{3}\mathrm{Blu3}^{*} \rightarrow {}^{1}\mathrm{Blu3}^{*} + \mathrm{Blu3} \qquad (13)$$

This process will generate two singlet excitons out of every ten triplet excitons, assuming the generation probability of triplet excitons is 75% and 25% for singlet excitons from T-T annihilation.[51] If the fraction of singlet excitons generated from triplet-triplet annihilation is non-negligible among the all singlet excitons, the luminance

will increase more than linearly with increasing current density, because the singlet exciton formation through T-T annihilation is second-order with respect to the concentration of $^{3}Blu3^{*}$, which is linear to the current density.[52] For our Device 14, the luminance increases linearly with increasing current density at low current injection and less than linearly at higher current injection, as shown in Figure 4.11. Therefore, the T-T annihilation does not make a significant contribution, if any, to the high EQE of our devices.

To further verify the fluorescent nature of the emission, we carried out time-resolved photoluminescence measurement at room temperature. The PL spectrum of doped Blu3 in CBP film is very similar to the EL spectrum of Device 14. Therefore, the emitting species and mechanisms of PL and EL are similar. The life time of the 454 nm PL emission excited by 325 nm femtosecond laser pulses (~150 fs) is 0.15 ns (Figure 4.13), indicating that the emission is fluorescent rather than phosphorescent.

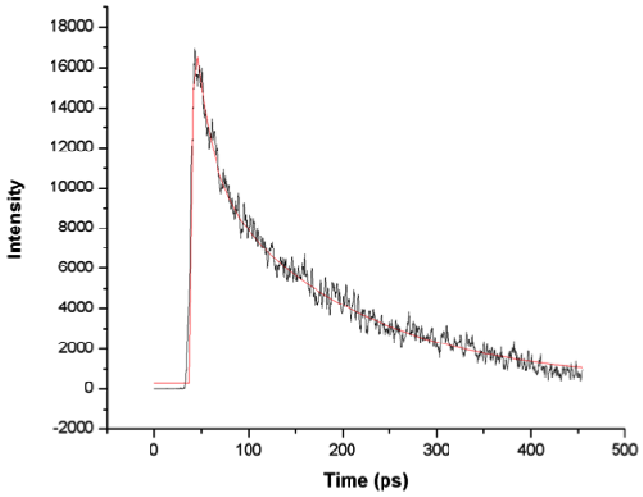

Figure 4.13. Time-resolved intensity of 454 nm PL emission from thin film of Blu3 doped in CBP with fitting. Lifetime of the emission is 0.15 ns, indicating the fluorescent nature of the emission.

According to classical statistics, the singlet exciton fraction generated from direct recombination is 25%, assuming the formation cross-section of singlet and triplet excitons is comparable., A recent theoretical study indicates that this assumption may not be correct.[13,53] The formation cross-section ratio of singlet to triplet excitons for some oligomers and polymers lies between 2 to 5, as determined by photoinduced absorption and magnetic resonance experiments[12] and equation-of-motion coupled cluster theoretical study.[54] Accordingly, the singlet generation fraction is about 40%-62.5%.

To investigate the singlet generation fraction in small molecular FOLEDs, we conducted a survey of the literature published during the period of year 1989 to year 2010. We collected all the data from the journal papers which satisfy the following criteria: (1) the emission is from small molecular fluorescent materials; (2) PL efficiency measured from solid thin film of emitting layer is provided; (3) EQE of the devices is provided; (4) devices are fabricated on planar glass substrates without any out-coupling techniques. If we assumed the recombination

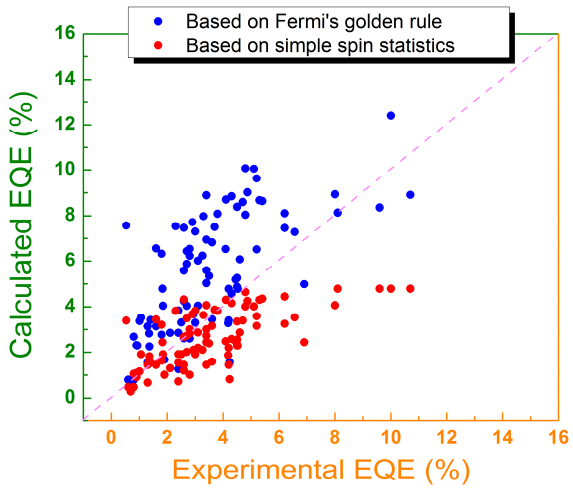

Figure 4.14. Comparison of calculated EQE and experimental EQE. The singlet generation fraction calculated from Shuai's method based on Fermi's golden rule and from simple spin statistic (25%) are used. Recombination efficiency is assumed to be 100% and out-coupling efficiency is assumed to be 20% for the calculation. Most of the calculated EQE with singlet generation fraction of 25% are smaller than the experimental EQE.

efficiency is 100%, out-coupling efficiency is 20% (estimated from ray optics), and used the PL efficiency from experiments, we can calculate the possible maximum EQE from equation (4.1). The comparison of the calculated EQE and experimental EQE is shown in Figure 4.14. If the singlet generation fraction is 25% as stated in simple spin statistics, most (60 out of 87 samples) of the calculated EQE are smaller than experimental EQE, which means recombination efficiency is larger than 100%. This is unreasonable. In contrast, using the singlet generation fraction calculated from Shuai's method, most of the calculated EQE are larger than experimental data.

In this survey, we use 20% as the out-coupling efficiency as estimated from ray optics for common glass ITO flat substrate based devices, which may not be true for some devices. For the devices in which the emitting dipole orientation prefer parallel orientation, the out-coupling efficiency can be as high as 35%, as simulated from the CPS model. However, we indeed notice that the Alq_3 based devices can achieve EQEs as high as 3.1% after device optimization without any out-coupling technique.[55] The orientation of emitting dipoles in Alq_3 films are randomly distributed,[45,46] corresponding to an out-coupling of about 20% simulated from CPS model. The highest PL efficiency of Alq_3 solid film in the literature is 40%.[56] If the singlet generation fraction is 25%, the maximum EQE of Alq_3 based devices is 2.0% if recombination efficiency can reach 100% after device optimization. Contradicting this, many experimental EQE for Alq_3 devices are larger than 2.0%.[55,57,58] More reasonably, singlet generation fraction of Alq3 is 43% estimated from Shuai's method. If the PL efficiency is 40%, out-coupling efficiency is 20%, and the recombination efficiency is 100%, the maximum EQE of Alq3 based devices can be as high as 3.4%.

Using Shuai's method,[54] we obtained 51% of χ for Blu3 and 42% for CBP. The exciton formation can be formed either on host molecules or directly on dopant molecules.[2,59] Therefore, for doped devices, χ is in the range of 42-51%. For Device 14, based on the measured PL efficiency (95 ± 5%), the calculated χ (42-51%), and out-coupling efficiency (18 ± 2%), the EQE is projected to be 8.5 ± 1.7%, assuming γ, the recombination efficiency, can reach unity after optimization of device configurations and fabrication process. The maximum EQE of devices 14 is 10.7%, which is very close to the projected range, indicating that our analysis is reasonable.

4.5. Conclusions

We have achieved EQE as high as 7.4% and 10.7% for undoped and doped blue fluorescent OLEDs, respectively, through optimizing both the molecular structures of emitters and the device configurations. The former was achieved through systematic analyses and predictive design using DFT and TDDFT calculations. The latter was realized by further optimizing EML thickness, thermal treatments, and doping strategy. Optical modeling based on CPS theory was used to study the out-coupling efficiency of the devices. The analysis on the high EQE supports that the singlet generation fraction can be much higher than 25%, which is from simple spin statistics. Our results exceed the traditional 5% limit for fluorescent OLEDs but agree with recent experimental and theoretical studies. Our efforts clearly indicate that fluorescent materials have a bright future for highly efficient and stable OLEDs for flat-panel display and lighting applications.

4.6. References

(1) Tang, C. W.; Vanslyke, S. A. *Appl. Phys. Lett.* **1987**, *51*, 913-915.

(2) Sun, Y. R.; Giebink, N. C.; Kanno, H.; Ma, B. W.; Thompson, M. E.; Forrest, S. R. *Nature* **2006**, *440*, 908-912.

(3) Reineke, S.; Lindner, F.; Schwartz, G.; Seidler, N.; Walzer, K.; Lussem, B.; Leo, K. *Nature* **2009**, *459*, 234-U116.

(4) Saleh; B. E. A.; Teich; M. C. *Fundamentals of Photonics*; Wiley: New York, 1991;

(5) Baldo, M.; Segal, M. *Phys. Stat. Sol. A* **2004**, *201*, 1205-1214.

(6) Friend, R. H.; Gymer, R. W.; Holmes, A. B.; Burroughes, J. H.; Marks, R. N.; Taliani, C.; Bradley, D. D. C.; Dos Santos, D. A.; Bredas, J. L.; Logdlund, M.; Salaneck, W. R. *Nature* **1999**, *397*, 121-128.

(7) Baldo, M. A.; Thompson, M. E.; Forrest, S. R. *Nature* **2000**, *403*, 750-753.

(8) Giebink, N. C.; Forrest, S. R. *Phys. Rev. B* **2008**, *77*,

(9) Baldo, M. A.; Adachi, C.; Forrest, S. R. *Phys. Rev. B* **2000**, *62*, 10967-10977.

(10) Staroske, W.; Pfeiffer, M.; Leo, K.; Hoffmann, M. *Phys. Rev. Lett.* **2007**, *98*,

(11) Cao, Y.; Parker, I. D.; Yu, G.; Zhang, C.; Heeger, A. J. *Nature* **1999**, *397*, 414-417.

(12) Wohlgenannt, M.; Tandon, K.; Mazumdar, S.; Ramasesha, S.; Vardeny, Z. V. *Nature* **2001**, *409*, 494-497.

(13) Shuai, Z.; Beljonne, D.; Silbey, R. J.; Bredas, J. L. *Phys. Rev. Lett.* **2000**, *84*, 131-134.

(14) Karabunarliev, S.; Bittner, E. R. *Phys. Rev. Lett.* **2003**, *90*,

(15) Wei, Y.; Chen, C. T. *J. Am. Chem. Soc.* **2007**, *129*, 7478.

(16) Okumoto, K.; Kanno, H.; Hamaa, Y.; Takahashi, H.; Shibata, K. *Appl. Phys. Lett.* **2006**, *89*,

(17) Chen, H. Y.; Lam, W. Y.; Luo, J. D.; Ho, Y. L.; Tang, B. Z.; Zhu, D. B.; Wong, M.; Kwok, H. S. *Appl. Phys. Lett.* **2002**, *81*, 574-576.

(18) Lin, S. L.; Chan, L. H.; Lee, R. H.; Yen, M. Y.; Kuo, W. J.; Chen, C. T.; Jeng, R. J. *Adv. Mater.* **2008**, *20*, 3947.

(19) Kim, S. K.; Yang, B.; Ma, Y.; Lee, J. H.; Park, J. W. *J. Mater. Chem.* **2008**, *18*, 3376-3384.

(20) Lyu, Y. Y.; Kwak, J.; Kwon, O.; Lee, S. H.; Kim, D.; Lee, C.; Char, K. *Adv. Mater.* **2008**, *20*, 2720.

(21) Liao, C. H.; Lee, M. T.; Tsai, C. H.; Chen, C. H. *Appl. Phys. Lett.* **2005**, *86*,

(22) Becke, A. D. *J. Chem. Phys.* **1993**, *98*, 5648-5652.

(23) *al.,* F. M. J. *e*. **2004**,

(24) Marcus, R. A.; Sutin, N. *Biochim. Biophys. Acta* **1985**, *811*, 265-322.

(25) Norton, J. E.; Bredas, J. L. *J. Am. Chem. Soc.* **2008**, *130*, 12377-12384.

(26) McMahon, D. P.; Troisi, A. *J. Phys. Chem. Lett.* **2010**, *1*, 941-946.

(27) Yin, S. W.; Chen, L. P.; Xuan, P. F.; Chen, K. Q.; Shuai, Z. *J. Phys. Chem. B* **2004**, *108*, 9608-9613.

(28) Sun, M. T.; Kjellberg, P.; Beenken, W. J. D.; Pullerits, T. *Chem. Phys.* **2006**, *327*, 474-484.

(29) Sancho-Garcia, J. C.; Foden, C. L.; Grizzi, I.; Greczynski, G.; de Jong, M. P.; Salaneck, W. R.; Bredas, J. L.; Cornil, J. *J. Phys. Chem. B* **2004**, *108*, 5594-5599.

(30) Zhen, C. G.; Chen, Z. K.; Liu, Q. D.; Dai, Y. F.; Shin, R. Y. C.; Chang, S. Y.; Kieffer, J. *Adv. Mater.* **2009**, *21*, 24225.

(31) OBrien, D.; Bleyer, A.; Lidzey, D. G.; Bradley, D. D. C.; Tsutsui, T. *J. Appl. Phys.* **1997**, *82*, 2662-2670.

(32) Zhu, L. H.; Tang, H. Q.; Harima, Y.; Kunugi, Y.; Yamashita, K.; Ohshita, J.; Kunai, A. *Thin Solid Films* **2001**, *396*, 213-218.

(33) Lampert, M. A.; Mark, P. **1970**,

(34) Burrows, P. E.; Shen, Z.; Bulovic, V.; McCarty, D. M.; Forrest, S. R.; Cronin, J. A.; Thompson, M. E. *J. Appl. Phys.* **1996**, *79*, 7991-8006.

(35) Sato, Y.; Kanai, H. *Mol. Cryst. Liq. Cryst.* **1994**, *252*, 435-442.

(36) Cheung, H. C. **1991**, *Vol. 2*, 129.

(37) Chang, S. C.; He, G.; Chen, F. C.; Guo, T. F.; Yang, Y. *Appl. Phys. Lett.* **2001**, *79*, 2088-2090.

(38) Kawamura, Y.; Sasabe, H.; Adachi, C. *Jpn. J. Appl. Phys.* **2004**, *43*, 7729-7730.

(39) Liu, Z. T.; Kwong, C. Y.; Cheung, C. H.; Djurisic, A. B.; Chan, Y.; Chui, P. C. *Synth. Met.* **2005**, *150*, 159-163.

(40) D'Andrade, B. W.; Baldo, M. A.; Adachi, C.; Brooks, J.; Thompson, M. E.; Forrest, S. R. *Appl. Phys. Lett.* **2001**, *79*, 1045-1047.

(41) Chen, C. H.; Shi, J.; Tang, C. W. *Macromol. Symp.* **1998**, *125*, 1-48.

(42) Baldo, M. A.; Soos, Z. G.; Forrest, S. R. *Chem. Phys. Lett.* **2001**, *347*, 297-303.

(43) Lamansky, S.; Djurovich, P.; Murphy, D.; Abdel-Razzaq, F.; Lee, H. E.; Adachi, C.; Burrows, P. E.; Forrest, S. R.; Thompson, M. E. *J. Am. Chem. Soc.* **2001**, *123*, 4304-4312.

(44) Kim, J. S.; Ho, P. K. H.; Greenham, N. C.; Friend, R. H. *J. Appl. Phys.* **2000**, *88*, 1073-1081.

(45) Yokoyama, D.; Sakaguchi, A.; Suzuki, M.; Adachi, C. *Appl. Phys. Lett.* **2008**, *93*,

(46) Yokoyama, D.; Sakaguchi, A.; Suzuki, M.; Adachi, C. *Org. Electron.* **2009**, *10*, 127-137.

(47) Yokoyama, D.; Setoguchi, Y.; Sakaguchi, A.; Suzuki, M.; Adachi, C. *Adv. Funct. Mater.* **2010**, *20*, 386-391.

(48) Chance, R. R.; Prock, A.; Silbey, R. *J. Chem. Phys.* **1974**, *60*, 2744-2748.

(49) Celebi, K.; Heidel, T. D.; Baldo, M. A. *Opt. Exp.* **2007**, *15*, 1762-1772.

(50) Pope, M.; Swenberg, C. E. **1982**,

(51) Kondakov, D. Y. *J. SID* **2009**, *17*, 137-144.

(52) Ganzorig, C.; Fujihira, M. *Appl. Phys. Lett.* **2002**, *81*, 3137-3139.

(53) Kobrak, M. N.; Bittner, E. R. *Phys. Rev. B* **2000**, *62*, 11473-11486.

(54) Chen, L. P.; Zhu, L. Y.; Shuai, Z. G. *J. Phys. Chem. A* **2006**, *110*, 13349-13354.

(55) Li, W. X.; Jones, R. A.; Allen, S. C.; Heikenfeld, J. C.; Steckl, A. J. *J. Disp. Technol.* **2006**, *2*, 143-152.

(56) Liao, S. H.; Shiu, J. R.; Liu, S. W.; Yeh, S. J.; Chen, Y. H.; Chen, C. T.; Chow, T. J.; Wu, C. I. *J. Am. Chem. Soc.* **2009**, *131*, 763-777.

(57) Qiu, Y.; Gao, Y. D.; Wei, P.; Wang, L. D. *Appl. Phys. Lett.* **2002**, *80*, 2628-2630.

(58) Deng, Z. B.; Ding, X. M.; Lee, S. T.; Gambling, W. A. *Appl. Phys. Lett.* **1999**, *74*, 2227-2229.

(59) Murata, H.; Merritt, C. D.; Kafafi, Z. H. *IEEE J. Sel. Top. Quantum Electron.* **1998**, *4*, 119-124.

Chapter 5. Summary and outlook

In this work, we used computational methods to tune the electronic properties of organic-inorganic hybrid materials, developed a multi-scale hopping model to investigate charge transport in organic semiconductors, and designed a series of highly efficient blue fluorescent materials for organic light emitting diodes (OLEDs).

The nanoscale inorganic skeleton of polyhedral oligomeric silsesquioxanes (POSS), combined with organic functional groups, was selected to construct new organic-inorganic hybrid materials due to its demonstrated thermal and mechanical stability. Geometry and electronic properties such as frontier orbitals distribution and energy level, HOMO-LUMO gap, reorganization energy, exciton binding energy were thoroughly studied in Chapter 2. The electronic properties of the hybrid materials are mainly controlled by the organic functional groups. The frontier orbitals localize in the organic segments, and the energy levels of the HOMO and LUMO are mainly determined by the electron donating and electron withdrawing groups. The HOMO-LUMO energy gap narrows to values corresponding to visible light for the hybrid molecules, indicating the potential applications in organic optoelectronic devices such as OLEDs and organic solar cells.

The rigid and stable three-dimensional structure of the POSS cage, as reflected by the small deformation after functionalization of organic groups, provides the possibility to

control the orientation and stacking configuration of organic molecules. Furthermore, molecular dynamic simulation revealed that the functional organic groups tend to aggregate to form organic phases. (Zhou, J. H.; Kieffer, J. *J. Phys. Chem. C* **2008**, *112*, 3473-3481.) Based on these simulation results, we designed dipentacene POSS hybrid molecules, in which two pentacene segments are attached to the POSS cage along the diagonal direction. The purpose of the design is to change the pentacene packing from the herringbone pattern that is characteristic of pure crystalline pentacene, *i.e.*, the neighboring molecules form V-shape dimers, into a configuration that better facilitates electron and/or hole transfer between molecules. We expect the pentacene segments to form a continuous phase in which the pentacene segments are aligned in parallel to achieve larger π-π stacking. To characterize the charge transport in the designed hybrid material, we developed a hopping model based on Marcus' electron transfer theory in which the charge transfer integral, reorganization energy and energy disorder (energy difference between hopping sites) control the charge hopping rate. A larger charge transfer integral, smaller reorganization energy and smaller energy disorder are preferred for higher charge transfer. Molecular dynamics simulations were used to predict the possible crystal structure of the hybrid material. Quantum chemistry calculations were used to estimate reorganization energy, energy disorder and the charge transfer integral between the molecules. The Kinetic Monte Carlo method was used to simulate the hopping path in crystal. To test this multi-scale model, we simulate the hole mobility in pentacene single crystal and compare results with experimental data. The simulation results are in agreement with the experimental data, confirming the reliability of the model. Molecular dynamics simulations of dipentacene POSS indicate that the pentacene

segments prefer to adopt parallel configuration in the predicted single crystal. In the dipentacene POSS crystal, in comparison to pristine crystalline pentacene, the charge transfer integrals between the hopping couples are larger, reorganization energy is smaller, and the energy of disorder is two orders of magnitude lower. The hole mobility of dipentacene POSS can achieve as high as 415 cm^2/Vs compared to 31 cm^2/Vs in pentacene at room temperature in this hopping model, confirming the succeed of the material design based on computation and modeling.

One possible extension of this work is to use the hopping model to simulate the charge transport in amorphous or polycrystalline organic materials that are widely used in organic electronic devices processed from vacuum deposition, vapor deposition, coating or injecting from solutions. Simulated hole mobility on amorphous pentacene based on this model is around 10^{-1} cm^2/Vs, one order of magnitude lower than the highest reported experimental results. The possible reason for the discrepancy between simulation and experiment is that the pentacene used in experiment is not really amorphous but polycrystalline with domain sizes in the range of 100 nm to several microns. (Brauer, B. et. al. *Chem. Mater.* **2010**, *22*, 3693-3697.) Our hopping model can access the dependence of charge mobility on domain size, temperature, and electric field (intensity and direction). Combining recording with the hopping process, we can investigate the factors limiting the charge mobility. Consequently, we can provide solutions to change the charge mobility by controlling the experiment conditions or designing new materials.

In Chapter 2 and Chapter 3, we showed that the properties of organic materials can be tailored through molecular design. If we know the desirable properties for certain

applications, we can design materials to achieve better performance for the applications. In Chapter 4, we applied the materials design based on computation to OLEDs, as an illustrative example.

To achieve efficient OLEDs, we need to maximize the formation of excitons that will decay to give photons. High formation efficiency of excitons requires balanced electron and hole injection and transport, which are mainly dependent on electronic properties of frontier orbitals. From Chapter 2, we know that the electronic properties of frontier orbitals especially HOMO and LUMO are mainly determined by electron donating groups and electron withdrawing groups. Therefore, we attached such groups to fluorene oligomer backbone, in order to achieve materials with a suitable band gap, low barrier for both hole injection and electron injection, as well as balanced hole and electron transport. The device performances based on these designed materials are very promising. Optimization of the device configurations further enhanced the external quantum efficiency to record breaking value of 10.7%, which far exceed the traditional efficiency upper limit of 5% if the singlet generation fraction is 25%. However, the literature survey on the journal papers published in the last two decades indicates that the singlet generation fraction may be larger than 25%. Using a model developed from Fermi's golden rule, we found that the singlet generation fraction of most of the organic emitters for OLEDs is in the range of 40% - 70%. This result clearly indicates that fluorescent materials can make more important contributions to highly efficient and stable OLEDs for flat-panel display and lighting applications than previously thought possible.

The successful materials design for OLEDs suggests that we can prescreen and optimize molecular structures before synthesis in the lab, to avoid iterative and costly Edisonian approaches. Extensions of this work can be applied to materials design for other applications such as organic photovoltaics, dye-sensitized solar cells, chemical sensing devices, and so on. General rules should include: (1) identification of properties-performance relationships; (2) material design to obtain the suitable properties; (3) experimental implementation; (4) optimization or re-design of materials based on the feedback from experimental results; (5) repetition of (3) and (4) until the target device performances are achieved.

Appendix A. Bond length changes between optimized neutral and charged geometries of POSS derivatives

C (black), H (white), O (red), N (blue), Si (gray).

Cy-POSS-T8

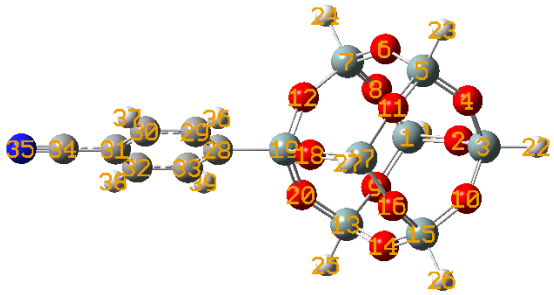

Bonds	R(0)/Å	R(-)/Å	R(+)/Å	|R(-)-R(0)| /Å	|R(+)-R(0)| /Å
R(1,2)	1.6432	1.6511	1.6359	0.0079	0.0073
R(1,8)	1.6438	1.6379	1.6507	0.0059	0.0069
R(1,9)	1.6434	1.6377	1.6501	0.0057	0.0067
R(1,21)	1.4645	1.4689	1.461	0.0044	0.0035
R(2,3)	1.6438	1.642	1.6457	0.0018	0.0019
R(3,4)	1.6438	1.642	1.6456	0.0018	0.0018
R(3,10)	1.6431	1.6414	1.645	0.0017	0.0019
R(3,22)	1.4645	1.4689	1.4608	0.0044	0.0037

R(4,5)	1.6432	1.6511	1.6359	0.0079	0.0073
R(5,6)	1.6438	1.6379	1.6507	0.0059	0.0069
R(5,11)	1.6434	1.6377	1.6501	0.0057	0.0067
R(5,23)	1.4645	1.4689	1.461	0.0044	0.0035
R(6,7)	1.6437	1.6571	1.6334	0.0134	0.0103
R(7,8)	1.6437	1.6571	1.6334	0.0134	0.0103
R(7,12)	1.6431	1.6141	1.6766	0.029	0.0335
R(7,24)	1.4646	1.4689	1.4616	0.0043	0.003
R(9,13)	1.6418	1.6536	1.6323	0.0118	0.0095
R(10,15)	1.6424	1.6499	1.6355	0.0075	0.0069
R(11,17)	1.6418	1.6536	1.6324	0.0118	0.0094
R(12,19)	1.645	1.6841	1.6256	0.0391	0.0194
R(13,14)	1.6425	1.6544	1.6319	0.0119	0.0106
R(13,20)	1.6452	1.6173	1.6772	0.0279	0.032
R(13,25)	1.4649	1.4686	1.462	0.0037	0.0029
R(14,15)	1.6441	1.638	1.6508	0.0061	0.0067
R(15,16)	1.6441	1.638	1.6508	0.0061	0.0067
R(15,26)	1.4644	1.4688	1.4609	0.0044	0.0035
R(16,17)	1.6425	1.6544	1.6319	0.0119	0.0106
R(17,18)	1.6452	1.6173	1.6772	0.0279	0.032
R(17,27)	1.4649	1.4686	1.462	0.0037	0.0029
R(18,19)	1.6449	1.674	1.6264	0.0291	0.0185

R(19,20)	1.6449	1.674	1.6264	0.0291	0.0185
R(19,28)	1.8559	1.7825	1.9016	0.0734	0.0457
R(28,29)	1.4062	1.4433	1.4354	0.0371	0.0292
R(28,33)	1.4062	1.4433	1.4354	0.0371	0.0292
R(29,30)	1.3915	1.3706	1.3719	0.0209	0.0196
R(29,36)	1.0863	1.0893	1.0853	0.003	1E-3
R(30,31)	1.4044	1.4399	1.4345	0.0355	0.0301
R(30,37)	1.0853	1.0879	1.085	0.0026	3E-4
R(31,32)	1.4044	1.4399	1.4345	0.0355	0.0301
R(31,34)	1.4348	1.4039	1.4096	0.0309	0.0252
R(32,33)	1.3915	1.3706	1.3719	0.0209	0.0196
R(32,38)	1.0853	1.0879	1.085	0.0026	3E-4
R(33,39)	1.0863	1.0893	1.0852	0.003	0.0011
R(34,35)	1.1632	1.1783	1.1715	0.0151	0.0083

Cy

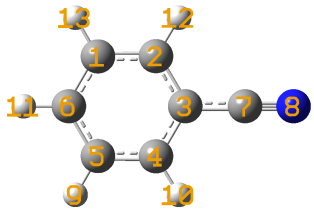

Bonds	R(0)/Å	R(-)/Å	R(+)/Å	|R(-)-R(0)| /Å	|R(+)-R(0)| /Å
R(1,2)	1.3925	1.3768	1.3724	0.0157	0.0201
R(1,6)	1.3971	1.4224	1.4242	0.0253	0.0271

R(1,13)	1.086	1.092	1.0851	0.006	9E-4
R(2,3)	1.4052	1.4513	1.4395	0.0461	0.0343
R(2,12)	1.0853	1.0887	1.085	0.0034	3E-4
R(3,4)	1.4052	1.4513	1.4395	0.0461	0.0343
R(3,7)	1.4343	1.3967	1.4048	0.0376	0.0295
R(4,5)	1.3925	1.3768	1.3724	0.0157	0.0201
R(4,10)	1.0853	1.0887	1.085	0.0034	3E-4
R(5,6)	1.3971	1.4224	1.4242	0.0253	0.0271
R(5,9)	1.086	1.092	1.0851	0.006	9E-4
R(6,11)	1.0864	1.0872	1.0868	8E-4	4E-4
R(7,8)	1.1634	1.1855	1.1743	0.0221	0.0109
Car-POSS-T8 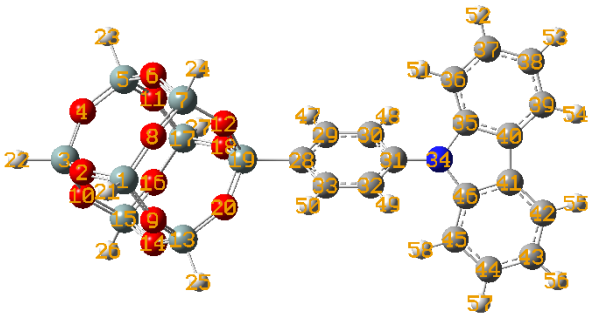					
Bonds	R(0)/Å	R(-)/Å	R(+)/Å	|R(-)-R(0)| /Å	|R(+)-R(0)| /Å
R(1,2)	1.6433	1.6508	1.6389	0.0075	0.0044
R(1,8)	1.6429	1.6374	1.6466	0.0055	0.0037
R(1,9)	1.6439	1.6387	1.6477	0.0052	0.0038

R(1,21)	1.4648	1.4693	1.4628	0.0045	0.002
R(2,3)	1.643	1.641	1.6442	0.002	0.0012
R(3,4)	1.6431	1.6416	1.6442	0.0015	0.0011
R(3,10)	1.6437	1.6429	1.6448	8E-4	0.0011
R(3,22)	1.4647	1.4692	1.4624	0.0045	0.0023
R(4,5)	1.6433	1.6513	1.6388	0.008	0.0045
R(5,6)	1.643	1.6364	1.6467	0.0066	0.0037
R(5,11)	1.6439	1.6388	1.6477	0.0051	0.0038
R(5,23)	1.4648	1.4692	1.4628	0.0044	0.002
R(6,7)	1.6444	1.6572	1.6385	0.0128	0.0059
R(7,8)	1.6443	1.6582	1.6384	0.0139	0.0059
R(7,12)	1.6409	1.6132	1.6566	0.0277	0.0157
R(7,24)	1.4649	1.4697	1.4637	0.0048	0.0012
R(9,13)	1.6437	1.6556	1.6378	0.0119	0.0059
R(10,15)	1.6434	1.6515	1.639	0.0081	0.0044
R(11,17)	1.6436	1.6558	1.6378	0.0122	0.0058
R(12,19)	1.6487	1.6916	1.6376	0.0429	0.0111
R(13,14)	1.6432	1.6539	1.6372	0.0107	0.006
R(13,20)	1.6419	1.6154	1.6578	0.0265	0.0159
R(13,25)	1.4652	1.4691	1.4642	0.0039	1E-3
R(14,15)	1.6434	1.6363	1.6471	0.0071	0.0037
R(15,16)	1.6433	1.6374	1.647	0.0059	0.0037

R(15,26)	1.4647	1.4691	1.4626	0.0044	0.0021
R(16,17)	1.643	1.6551	1.637	0.0121	0.006
R(17,18)	1.6422	1.6145	1.6581	0.0277	0.0159
R(17,27)	1.4652	1.469	1.4641	0.0038	0.0011
R(18,19)	1.6465	1.6763	1.6368	0.0298	0.0097
R(19,20)	1.6467	1.6775	1.6369	0.0308	0.0098
R(19,28)	1.8485	1.7768	1.875	0.0717	0.0265
R(28,29)	1.4059	1.4507	1.4075	0.0448	0.0016
R(28,33)	1.4061	1.4509	1.4077	0.0448	0.0016
R(29,30)	1.3926	1.3734	1.3904	0.0192	0.0022
R(29,47)	1.0867	1.0889	1.0858	0.0022	9E-4
R(30,31)	1.4014	1.4277	1.4047	0.0263	0.0033
R(30,48)	1.0853	1.0887	1.0852	0.0034	1E-4
R(31,32)	1.4015	1.4275	1.4049	0.026	0.0034
R(31,34)	1.4169	1.4271	1.4182	0.0102	0.0013
R(32,33)	1.3924	1.3735	1.3902	0.0189	0.0022
R(32,49)	1.0853	1.0887	1.0851	0.0034	2E-4
R(33,50)	1.0869	1.0889	1.0859	0.002	1E-3
R(34,35)	1.4024	1.3914	1.3986	0.011	0.0038
R(34,46)	1.4024	1.3913	1.3985	0.0111	0.0039
R(35,36)	1.3976	1.4003	1.4013	0.0027	0.0037
R(35,40)	1.4177	1.424	1.4197	0.0063	0.002

R(36,37)	1.3935	1.3914	1.3956	0.0021	0.0021
R(36,51)	1.0848	1.0851	1.0838	3E-4	1E-3
R(37,38)	1.4051	1.4094	1.4004	0.0043	0.0047
R(37,52)	1.0866	1.0879	1.0849	0.0013	0.0017
R(38,39)	1.3917	1.3923	1.409	6E-4	0.0173
R(38,53)	1.0862	1.0875	1.0854	0.0013	8E-4
R(39,40)	1.3996	1.4007	1.3848	0.0011	0.0148
R(39,54)	1.0869	1.0883	1.0855	0.0014	0.0014
R(40,41)	1.4481	1.4449	1.4615	0.0032	0.0134
R(41,42)	1.3996	1.4007	1.3848	0.0011	0.0148
R(41,46)	1.4177	1.424	1.4198	0.0063	0.0021
R(42,43)	1.3917	1.3923	1.409	6E-4	0.0173
R(42,55)	1.0869	1.0883	1.0855	0.0014	0.0014
R(43,44)	1.4051	1.4093	1.4004	0.0042	0.0047
R(43,56)	1.0862	1.0875	1.0854	0.0013	8E-4
R(44,45)	1.3935	1.3914	1.3956	0.0021	0.0021
R(44,57)	1.0866	1.0879	1.0849	0.0013	0.0017
R(45,46)	1.3977	1.4003	1.4014	0.0026	0.0037
R(45,58)	1.0848	1.0851	1.0838	3E-4	1E-3
Car					

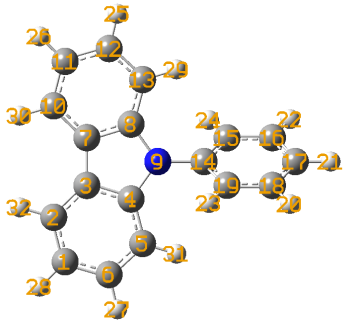

Bonds	R(0)/Å	R(-)/Å	R(+)/Å	|R(-)-R(0)| /Å	|R(+)-R(0)| /Å
R(1,2)	1.3918	1.3905	1.4095	0.0013	0.0177
R(1,6)	1.4056	1.4058	1.4005	2E-4	0.0051
R(1,28)	1.0863	1.0907	1.0854	0.0044	9E-4
R(2,3)	1.3998	1.4274	1.3845	0.0276	0.0153
R(2,32)	1.087	1.0882	1.0855	0.0012	0.0015
R(3,4)	1.4184	1.4371	1.4201	0.0187	0.0017
R(3,7)	1.448	1.4138	1.4617	0.0342	0.0137
R(4,5)	1.3977	1.3849	1.4016	0.0128	0.0039
R(4,9)	1.3998	1.4201	1.3976	0.0203	0.0022
R(5,6)	1.3933	1.4201	1.3955	0.0268	0.0022
R(5,31)	1.085	1.0857	1.0838	7E-4	0.0012
R(6,27)	1.0867	1.0875	1.0848	8E-4	0.0019
R(7,8)	1.4184	1.4371	1.4201	0.0187	0.0017
R(7,10)	1.3998	1.4274	1.3845	0.0276	0.0153
R(8,9)	1.3998	1.4201	1.3977	0.0203	0.0021
R(8,13)	1.3977	1.3849	1.4016	0.0128	0.0039

R(9,14)	1.4212	1.4013	1.4205	0.0199	7E-4
R(10,11)	1.3918	1.3905	1.4095	0.0013	0.0177
R(10,30)	1.087	1.0882	1.0855	0.0012	0.0015
R(11,12)	1.4056	1.4058	1.4005	2E-4	0.0051
R(11,26)	1.0863	1.0907	1.0854	0.0044	9E-4
R(12,13)	1.3933	1.4201	1.3956	0.0268	0.0023
R(12,25)	1.0867	1.0875	1.0848	8E-4	0.0019
R(13,29)	1.085	1.0857	1.0838	7E-4	0.0012
R(14,15)	1.4008	1.4129	1.4048	0.0121	0.004
R(14,19)	1.4008	1.4129	1.4048	0.0121	0.004
R(15,16)	1.3947	1.3909	1.3913	0.0038	0.0034
R(15,24)	1.0856	1.0846	1.085	1E-3	6E-4
R(16,17)	1.3963	1.4013	1.3988	0.005	0.0025
R(16,22)	1.0866	1.0887	1.0854	0.0021	0.0012
R(17,18)	1.3963	1.4013	1.3988	0.005	0.0025
R(17,21)	1.0863	1.0872	1.0855	9E-4	8E-4
R(18,19)	1.3947	1.3909	1.3913	0.0038	0.0034
R(18,20)	1.0866	1.0887	1.0854	0.0021	0.0012
R(19,23)	1.0856	1.0846	1.085	1E-3	6E-4
Cy-Car-POSS-T8					

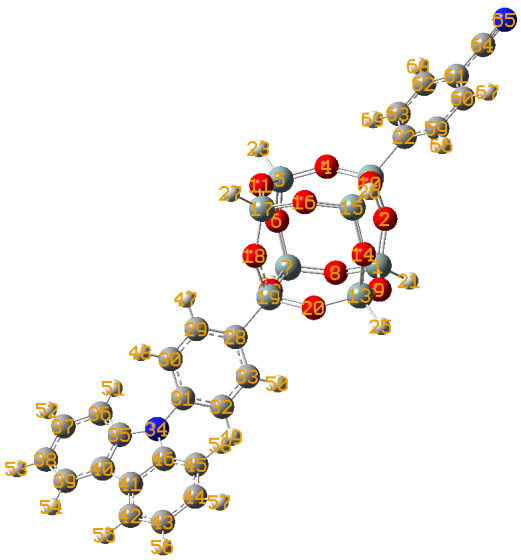

Bonds	R(0)/Å	R(-)/Å	R(+)/Å	|R(-)-R(0)| /Å	|R(+)-R(0)| /Å
R(1,2)	1.6436	1.6225	1.6379	0.0211	0.0057
R(1,8)	1.6429	1.6515	1.6471	0.0086	0.0042
R(1,9)	1.6438	1.6529	1.6481	0.0091	0.0043
R(1,21)	1.4647	1.4683	1.4628	0.0036	0.0019
R(2,3)	1.6454	1.6723	1.6481	0.0269	0.0027
R(3,4)	1.6441	1.6644	1.6466	0.0203	0.0025
R(3,10)	1.6446	1.6658	1.647	0.0212	0.0024
R(3,22)	1.8562	1.8012	1.8502	0.055	0.006
R(4,5)	1.6449	1.6243	1.6392	0.0206	0.0057
R(5,6)	1.6422	1.6503	1.6463	0.0081	0.0041
R(5,11)	1.6426	1.6504	1.6467	0.0078	0.0041
R(5,23)	1.465	1.4682	1.4631	0.0032	0.0019
R(6,7)	1.6454	1.6426	1.6393	0.0028	0.0061

R(7,8)	1.6443	1.6409	1.6383	0.0034	0.006
R(7,12)	1.6403	1.643	1.6562	0.0027	0.0159
R(7,24)	1.4647	1.4683	1.4637	0.0036	1E-3
R(9,13)	1.6439	1.6409	1.6378	0.003	0.0061
R(10,15)	1.645	1.6245	1.6393	0.0205	0.0057
R(11,17)	1.6439	1.6405	1.6379	0.0034	0.006
R(12,19)	1.6488	1.6505	1.6376	0.0017	0.0112
R(13,14)	1.6442	1.641	1.638	0.0032	0.0062
R(13,20)	1.6412	1.6437	1.6573	0.0025	0.0161
R(13,25)	1.465	1.4685	1.4641	0.0035	9E-4
R(14,15)	1.6425	1.6504	1.6466	0.0079	0.0041
R(15,16)	1.6421	1.65	1.6461	0.0079	0.004
R(15,26)	1.4648	1.4681	1.463	0.0033	0.0018
R(16,17)	1.6435	1.6399	1.6373	0.0036	0.0062
R(17,18)	1.6415	1.6442	1.6576	0.0027	0.0161
R(17,27)	1.4649	1.4685	1.464	0.0036	9E-4
R(18,19)	1.647	1.6484	1.6372	0.0014	0.0098
R(19,20)	1.6469	1.6477	1.6369	8E-4	0.01
R(19,28)	1.8478	1.8443	1.8747	0.0035	0.0269
R(22,59)	1.4061	1.4336	1.4064	0.0275	3E-4
R(22,63)	1.4061	1.4333	1.4065	0.0272	4E-4
R(28,29)	1.4059	1.4113	1.4074	0.0054	0.0015

R(28,33)	1.4063	1.4116	1.4077	0.0053	0.0014
R(29,30)	1.3926	1.3902	1.3905	0.0024	0.0021
R(29,47)	1.0866	1.0869	1.0858	3E-4	8E-4
R(30,31)	1.4014	1.4054	1.4046	0.004	0.0032
R(30,48)	1.0853	1.0859	1.0852	6E-4	1E-4
R(31,32)	1.4017	1.4054	1.4048	0.0037	0.0031
R(31,34)	1.4165	1.4194	1.4185	0.0029	0.002
R(32,33)	1.3923	1.39	1.3902	0.0023	0.0021
R(32,49)	1.0852	1.0858	1.0851	6E-4	1E-4
R(33,50)	1.0869	1.0871	1.086	2E-4	9E-4
R(34,35)	1.4026	1.4009	1.3985	0.0017	0.0041
R(34,46)	1.4026	1.4009	1.3984	0.0017	0.0042
R(35,36)	1.3976	1.3967	1.4014	9E-4	0.0038
R(35,40)	1.4176	1.422	1.4198	0.0044	0.0022
R(36,37)	1.3935	1.3951	1.3956	0.0016	0.0021
R(36,51)	1.0848	1.0849	1.0838	1E-4	1E-3
R(37,38)	1.4051	1.4068	1.4004	0.0017	0.0047
R(37,52)	1.0866	1.0868	1.0849	2E-4	0.0017
R(38,39)	1.3917	1.391	1.4091	7E-4	0.0174
R(38,53)	1.0862	1.0869	1.0854	7E-4	8E-4
R(39,40)	1.3996	1.4029	1.3848	0.0033	0.0148
R(39,54)	1.0869	1.0874	1.0855	5E-4	0.0014

R(40,41)	1.4482	1.4425	1.4615	0.0057	0.0133
R(41,42)	1.3996	1.4029	1.3848	0.0033	0.0148
R(41,46)	1.4176	1.422	1.4198	0.0044	0.0022
R(42,43)	1.3917	1.391	1.4091	7E-4	0.0174
R(42,55)	1.0869	1.0874	1.0855	5E-4	0.0014
R(43,44)	1.4051	1.4068	1.4004	0.0017	0.0047
R(43,56)	1.0862	1.0869	1.0854	7E-4	8E-4
R(44,45)	1.3935	1.3951	1.3956	0.0016	0.0021
R(44,57)	1.0866	1.0868	1.0849	2E-4	0.0017
R(45,46)	1.3976	1.3967	1.4014	9E-4	0.0038
R(45,58)	1.0848	1.0849	1.0838	1E-4	1E-3
R(59,60)	1.3915	1.3753	1.3913	0.0162	2E-4
R(59,66)	1.0863	1.0885	1.0863	0.0022	0
R(60,61)	1.4044	1.4323	1.4043	0.0279	1E-4
R(60,67)	1.0853	1.0871	1.0851	0.0018	2E-4
R(61,62)	1.4045	1.4324	1.4044	0.0279	1E-4
R(61,64)	1.4348	1.4097	1.4348	0.0251	0
R(62,63)	1.3914	1.3754	1.3913	0.016	1E-4
R(62,68)	1.0853	1.0871	1.0851	0.0018	2E-4
R(63,69)	1.0864	1.0884	1.0864	0.002	0
R(64,65)	1.1632	1.1752	1.1629	0.012	3E-4

Cy-Car

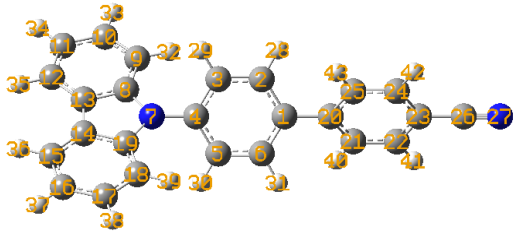

Bonds	R(0)/Å	R(-)/Å	R(+)/Å	|R(-)-R(0)| /Å	|R(+)-R(0)| /Å
R(1,2)	1.4062	1.4347	1.4125	0.0285	0.0063
R(1,6)	1.4062	1.4347	1.4125	0.0285	0.0063
R(1,20)	1.4844	1.4413	1.474	0.0431	0.0104
R(2,3)	1.3935	1.3822	1.3851	0.0113	0.0084
R(2,28)	1.0866	1.0852	1.0849	0.0014	0.0017
R(3,4)	1.4012	1.4093	1.4078	0.0081	0.0066
R(3,29)	1.086	1.0883	1.0846	0.0023	0.0014
R(4,5)	1.4012	1.4093	1.4078	0.0081	0.0066
R(4,7)	1.4194	1.4314	1.4087	0.012	0.0107
R(5,6)	1.3935	1.3822	1.3851	0.0113	0.0084
R(5,30)	1.086	1.0883	1.0846	0.0023	0.0014
R(6,31)	1.0866	1.0852	1.0849	0.0014	0.0017
R(7,8)	1.401	1.3907	1.404	0.0103	0.003
R(7,19)	1.401	1.3907	1.404	0.0103	0.003
R(8,9)	1.3988	1.3992	1.4003	4E-4	0.0015
R(8,13)	1.4189	1.4224	1.418	0.0035	9E-4

R(9,10)	1.3952	1.3919	1.3956	0.0033	4E-4
R(9,32)	1.0855	1.0852	1.0837	3E-4	0.0018
R(10,11)	1.4072	1.4082	1.4007	1E-3	0.0065
R(10,33)	1.0869	1.0875	1.085	6E-4	0.0019
R(11,12)	1.3937	1.3922	1.4061	0.0015	0.0124
R(11,34)	1.0865	1.0872	1.0854	7E-4	0.0011
R(12,13)	1.401	1.4006	1.3868	4E-4	0.0142
R(12,35)	1.0872	1.088	1.0856	8E-4	0.0016
R(13,14)	1.449	1.4465	1.4599	0.0025	0.0109
R(14,15)	1.401	1.4006	1.3868	4E-4	0.0142
R(14,19)	1.4189	1.4224	1.418	0.0035	9E-4
R(15,16)	1.3937	1.3922	1.4061	0.0015	0.0124
R(15,36)	1.0872	1.088	1.0856	8E-4	0.0016
R(16,17)	1.4072	1.4082	1.4007	1E-3	0.0065
R(16,37)	1.0865	1.0872	1.0854	7E-4	0.0011
R(17,18)	1.3952	1.3919	1.3956	0.0033	4E-4
R(17,38)	1.0869	1.0875	1.085	6E-4	0.0019
R(18,19)	1.3988	1.3992	1.4003	4E-4	0.0015
R(18,39)	1.0855	1.0852	1.0837	3E-4	0.0018
R(20,21)	1.4076	1.4371	1.4101	0.0295	0.0025
R(20,25)	1.4076	1.4371	1.4101	0.0295	0.0025
R(21,22)	1.3913	1.3747	1.3874	0.0166	0.0039

R(21,40)	1.0862	1.0861	1.0853	1E-4	9E-4
R(22,23)	1.4057	1.427	1.4063	0.0213	6E-4
R(22,41)	1.0857	1.0878	1.0847	0.0021	1E-3
R(23,24)	1.4057	1.427	1.4063	0.0213	6E-4
R(23,26)	1.4342	1.4111	1.432	0.0231	0.0022
R(24,25)	1.3913	1.3747	1.3874	0.0166	0.0039
R(24,42)	1.0857	1.0878	1.0847	0.0021	1E-3
R(25,43)	1.0862	1.0861	1.0853	1E-4	9E-4
R(26,27)	1.1642	1.1743	1.1631	0.0101	0.0011
Cy-Car-POSS-T8-N_2-Para 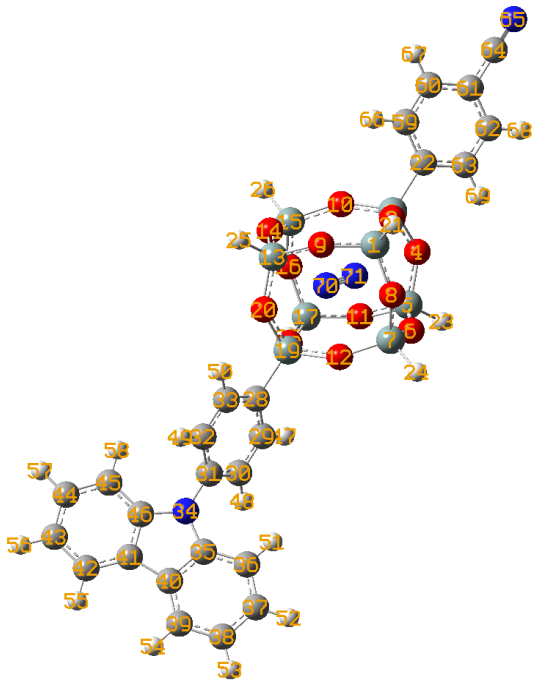					
Bonds	R(0)/Å	R(-)/Å	R(+)/Å	|R(-)-R(0)| /Å	|R(+)-R(0)| /Å

R(1,2)	1.6679	1.6608	1.6627	0.0071	0.0052
R(1,8)	1.6581	1.6611	1.6616	0.003	0.0035
R(1,9)	1.6678	1.6582	1.6715	0.0096	0.0037
R(1,21)	1.4627	1.4699	1.461	0.0072	0.0017
R(1,70)	2.7908	2.8259	2.8155	0.0351	0.0247
R(1,71)	2.7998	2.831	2.7939	0.0312	0.0059
R(2,3)	1.6774	1.6871	1.6809	0.0097	0.0035
R(2,70)	2.999	3.0881	3.0136	0.0891	0.0146
R(2,71)	2.4611	2.5269	2.4439	0.0658	0.0172
R(3,4)	1.6837	1.6888	1.6857	0.0051	0.002
R(3,10)	1.6767	1.6874	1.6799	0.0107	0.0032
R(3,22)	1.8557	1.8916	1.8491	0.0359	0.0066
R(3,71)	2.3772	2.1645	2.3871	0.2127	0.0099
R(4,5)	1.6854	1.6932	1.6783	0.0078	0.0071
R(4,71)	2.4241	2.3685	2.4237	0.0556	4E-4
R(5,6)	1.6747	1.6859	1.6783	0.0112	0.0036
R(5,11)	1.6749	1.6864	1.6783	0.0115	0.0034
R(5,23)	1.4635	1.476	1.4617	0.0125	0.0018
R(5,71)	2.3462	2.2066	2.3667	0.1396	0.0205
R(6,7)	1.6695	1.6584	1.6632	0.0111	0.0063
R(6,70)	3.0268	3.1088	3.0048	0.082	0.022
R(6,71)	2.4517	2.5393	2.4562	0.0876	0.0045

R(7,8)	1.6594	1.6611	1.6536	0.0017	0.0058
R(7,12)	1.6644	1.6596	1.6808	0.0048	0.0164
R(7,24)	1.4628	1.47	1.4621	0.0072	7E-4
R(7,70)	2.8046	2.8347	2.7996	0.0301	0.005
R(7,71)	2.7845	2.8304	2.7944	0.0459	0.0099
R(8,70)	2.7799	2.816	2.7772	0.0361	0.0027
R(8,71)	2.7711	2.8139	2.7671	0.0428	0.004
R(9,13)	1.6762	1.6864	1.6677	0.0102	0.0085
R(9,70)	2.4525	2.5348	2.4679	0.0823	0.0154
R(9,71)	3.0208	3.1087	3.0037	0.0879	0.0171
R(10,15)	1.6684	1.661	1.663	0.0074	0.0054
R(10,70)	2.9947	3.0799	3.008	0.0852	0.0133
R(10,71)	2.4664	2.5257	2.4508	0.0593	0.0156
R(11,17)	1.6689	1.6578	1.6627	0.0111	0.0062
R(11,70)	3.0236	3.1075	2.9989	0.0839	0.0247
R(11,71)	2.4525	2.5386	2.4573	0.0861	0.0048
R(12,19)	1.6807	1.685	1.6707	0.0043	0.01
R(12,70)	2.4603	2.5387	2.4585	0.0784	0.0018
R(12,71)	2.992	3.1016	3.0159	0.1096	0.0239
R(13,14)	1.677	1.6873	1.6686	0.0103	0.0084
R(13,20)	1.6819	1.6922	1.6975	0.0103	0.0156
R(13,25)	1.4635	1.4761	1.4624	0.0126	0.0011

R(13,70)	2.3437	2.2028	2.3759	0.1409	0.0322
R(14,15)	1.6676	1.6582	1.6713	0.0094	0.0037
R(14,70)	2.4487	2.5323	2.4638	0.0836	0.0151
R(14,71)	3.0266	3.1143	3.012	0.0877	0.0146
R(15,16)	1.658	1.6612	1.6614	0.0032	0.0034
R(15,26)	1.4629	1.4701	1.4612	0.0072	0.0017
R(15,70)	2.7802	2.815	2.8031	0.0348	0.0229
R(15,71)	2.8041	2.8317	2.8013	0.0276	0.0028
R(16,17)	1.6594	1.661	1.6538	0.0016	0.0056
R(16,70)	2.7665	2.8038	2.7609	0.0373	0.0056
R(16,71)	2.7743	2.8143	2.774	0.04	3E-4
R(17,18)	1.6648	1.6599	1.6814	0.0049	0.0166
R(17,27)	1.4629	1.4701	1.4621	0.0072	8E-4
R(17,70)	2.7978	2.8283	2.7895	0.0305	0.0083
R(17,71)	2.7872	2.829	2.7991	0.0418	0.0119
R(18,19)	1.6798	1.6846	1.6708	0.0048	0.009
R(18,70)	2.4608	2.5378	2.4564	0.077	0.0044
R(18,71)	2.9957	3.101	3.0208	0.1053	0.0251
R(19,20)	1.6862	1.6857	1.6778	5E-4	0.0084
R(19,28)	1.8469	1.8836	1.8755	0.0367	0.0286
R(19,70)	2.3941	2.2181	2.3002	0.176	0.0939
R(20,70)	2.4239	2.3797	2.4238	0.0442	1E-4

R(22,59)	1.4066	1.407	1.407	4E-4	4E-4
R(22,63)	1.4054	1.4055	1.4058	1E-4	4E-4
R(28,29)	1.4067	1.4057	1.4081	1E-3	0.0014
R(28,33)	1.4054	1.4046	1.4069	8E-4	0.0015
R(29,30)	1.3916	1.3939	1.3896	0.0023	0.002
R(29,47)	1.087	1.0867	1.086	3E-4	1E-3
R(30,31)	1.4022	1.3993	1.4053	0.0029	0.0031
R(30,48)	1.0853	1.0864	1.0852	0.0011	1E-4
R(31,32)	1.4008	1.3983	1.4042	0.0025	0.0034
R(31,34)	1.4166	1.428	1.4183	0.0114	0.0017
R(32,33)	1.3932	1.3955	1.3911	0.0023	0.0021
R(32,49)	1.0853	1.0865	1.0852	0.0012	1E-4
R(33,50)	1.0859	1.0859	1.0852	0	7E-4
R(34,35)	1.4025	1.3954	1.3986	0.0071	0.0039
R(34,46)	1.4025	1.3954	1.3984	0.0071	0.0041
R(35,36)	1.3976	1.3985	1.4012	9E-4	0.0036
R(35,40)	1.4176	1.42	1.4197	0.0024	0.0021
R(36,37)	1.3935	1.3926	1.3957	9E-4	0.0022
R(36,51)	1.0848	1.0849	1.0838	1E-4	1E-3
R(37,38)	1.4051	1.4066	1.4004	0.0015	0.0047
R(37,52)	1.0866	1.087	1.0849	4E-4	0.0017
R(38,39)	1.3917	1.3917	1.4089	0	0.0172

R(38,53)	1.0862	1.0867	1.0854	5E-4	8E-4
R(39,40)	1.3996	1.4002	1.3849	6E-4	0.0147
R(39,54)	1.0869	1.0874	1.0855	5E-4	0.0014
R(40,41)	1.4481	1.4471	1.4614	1E-3	0.0133
R(41,42)	1.3996	1.4002	1.3848	6E-4	0.0148
R(41,46)	1.4176	1.4201	1.4199	0.0025	0.0023
R(42,43)	1.3917	1.3918	1.409	1E-4	0.0173
R(42,55)	1.0869	1.0874	1.0855	5E-4	0.0014
R(43,44)	1.4051	1.4066	1.4004	0.0015	0.0047
R(43,56)	1.0862	1.0867	1.0854	5E-4	8E-4
R(44,45)	1.3935	1.3926	1.3956	9E-4	0.0021
R(44,57)	1.0866	1.087	1.0849	4E-4	0.0017
R(45,46)	1.3976	1.3985	1.4014	9E-4	0.0038
R(45,58)	1.0848	1.0849	1.0838	1E-4	1E-3
R(59,60)	1.3907	1.3909	1.3906	2E-4	1E-4
R(59,66)	1.0866	1.0866	1.0866	0	0
R(60,61)	1.405	1.4059	1.4049	9E-4	1E-4
R(60,67)	1.0853	1.0861	1.0851	8E-4	2E-4
R(61,62)	1.4039	1.4046	1.4038	7E-4	1E-4
R(61,64)	1.4347	1.4336	1.4348	0.0011	1E-4
R(62,63)	1.3921	1.3927	1.392	6E-4	1E-4
R(62,68)	1.0853	1.0862	1.0851	9E-4	2E-4

R(63,69)	1.0855	1.0855	1.0856	0	1E-4
R(64,65)	1.1632	1.1645	1.1629	0.0013	3E-4
R(70,71)	1.0951	1.1609	1.095	0.0658	1E-4

Cy-Car-POSS-T8-N_2-Perp

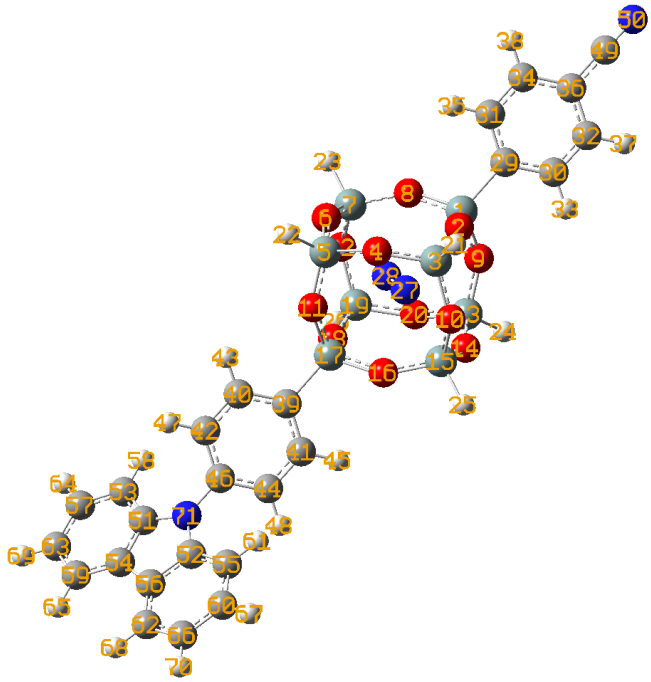

Bonds	R(0)/Å	R(-)/Å	R(+)/Å	|R(-)-R(0)| /Å	|R(+)-R(0)| /Å
R(1,2)	1.6702	1.6567	1.6734	0.0135	0.0032
R(1,8)	1.6686	1.6557	1.6717	0.0129	0.0031
R(1,9)	1.6599	1.6596	1.6623	0.0003	0.0024
R(1,27)	2.827	2.8254	2.8428	0.0016	0.0158
R(1,28)	2.7823	2.8099	2.7863	0.0276	0.004
R(1,29)	1.8532	1.872	1.847	0.0188	0.0062

R(2,3)	1.6754	1.6919	1.6694	0.0165	0.006
R(2,27)	2.462	2.5326	2.4549	0.0706	0.0071
R(2,28)	2.9831	3.0877	2.9686	0.1046	0.0145
R(3,4)	1.676	1.6879	1.6802	0.0119	0.0042
R(3,10)	1.683	1.6893	1.6868	0.0063	0.0038
R(3,21)	1.463	1.476	1.4612	0.013	0.0018
R(3,27)	2.3597	2.1995	2.3702	0.1602	0.0105
R(4,5)	1.6676	1.6568	1.6616	0.0108	0.006
R(4,27)	2.4553	2.5342	2.4523	0.0789	0.003
R(4,28)	3.0198	3.0986	3.0235	0.0788	0.0037
R(5,6)	1.6681	1.6581	1.6621	0.01	0.006
R(5,11)	1.6568	1.6638	1.6727	0.007	0.0159
R(5,22)	1.4631	1.4708	1.4623	0.0077	0.0008
R(5,27)	2.7816	2.828	2.7834	0.0464	0.0018
R(5,28)	2.8079	2.8284	2.8198	0.0205	0.0119
R(6,7)	1.6746	1.6872	1.6786	0.0126	0.004
R(6,27)	3.0048	3.1077	2.9995	0.1029	0.0053
R(6,28)	2.4636	2.5373	2.4631	0.0737	0.0005
R(7,8)	1.6781	1.6932	1.6726	0.0151	0.0055
R(7,12)	1.6815	1.6877	1.6854	0.0062	0.0039
R(7,23)	1.4636	1.4769	1.4617	0.0133	0.0019
R(7,28)	2.3527	2.1979	2.3608	0.1548	0.0081

R(8,27)	3.0335	3.1121	3.0292	0.0786	0.0043
R(8,28)	2.4511	2.533	2.4392	0.0819	0.0119
R(9,13)	1.6602	1.666	1.6549	0.0058	0.0053
R(9,27)	2.7977	2.818	2.7945	0.0203	0.0032
R(9,28)	2.7573	2.8129	2.7407	0.0556	0.0166
R(10,15)	1.6831	1.6883	1.6767	0.0052	0.0064
R(10,27)	2.4236	2.3765	2.4228	0.0471	0.0008
R(11,17)	1.6627	1.6612	1.6526	0.0015	0.0101
R(11,27)	2.7535	2.812	2.7593	0.0585	0.0058
R(11,28)	2.7936	2.8178	2.8135	0.0242	0.0199
R(12,19)	1.6846	1.69	1.6782	0.0054	0.0064
R(12,28)	2.4237	2.3762	2.4222	0.0475	0.0015
R(13,14)	1.6666	1.6572	1.6709	0.0094	0.0043
R(13,20)	1.6661	1.656	1.6705	0.0101	0.0044
R(13,24)	1.4631	1.4707	1.4614	0.0076	0.0017
R(13,27)	2.8094	2.8292	2.8169	0.0198	0.0075
R(13,28)	2.783	2.8291	2.7807	0.0461	0.0023
R(14,15)	1.6761	1.6879	1.6699	0.0118	0.0062
R(14,27)	2.464	2.5389	2.4612	0.0749	0.0028
R(14,28)	3.0053	3.1097	2.9961	0.1044	0.0092
R(15,16)	1.6743	1.6899	1.692	0.0156	0.0177
R(15,25)	1.4635	1.4767	1.4629	0.0132	0.0006

R(15,27)	2.3519	2.2028	2.3545	0.1491	0.0026
R(16,17)	1.6718	1.6576	1.6608	0.0142	0.011
R(16,27)	2.4459	2.5341	2.4581	0.0882	0.0122
R(16,28)	3.0283	3.1124	3.0483	0.0841	0.02
R(17,18)	1.6739	1.6588	1.6611	0.0151	0.0128
R(17,27)	2.7927	2.8213	2.7386	0.0286	0.0541
R(17,28)	2.8377	2.8373	2.7949	0.0004	0.0428
R(17,39)	1.8447	1.8665	1.8712	0.0218	0.0265
R(18,19)	1.6718	1.6889	1.6888	0.0171	0.017
R(18,27)	2.9784	3.0874	2.988	0.109	0.0096
R(18,28)	2.4573	2.5336	2.4745	0.0763	0.0172
R(19,20)	1.6775	1.6887	1.6714	0.0112	0.0061
R(19,26)	1.4631	1.4761	1.4623	0.013	0.0008
R(19,28)	2.3586	2.2023	2.3634	0.1563	0.0048
R(20,27)	3.0203	3.0988	3.0189	0.0785	0.0014
R(20,28)	2.4554	2.5348	2.4501	0.0794	0.0053
R(27,28)	1.0949	1.1609	1.095	0.066	1E-04
R(29,30)	1.4062	1.4061	1.4066	1E-04	0.0004
R(29,31)	1.4058	1.4055	1.4062	0.0003	0.0004
R(30,32)	1.3913	1.3913	1.3911	0	0.0002
R(30,33)	1.0863	1.0864	1.0863	1E-04	0
R(31,34)	1.3916	1.392	1.3914	0.0004	0.0002

R(31,35)	1.0861	1.086	1.0862	1E-04	1E-04
R(32,36)	1.4046	1.4054	1.4045	0.0008	1E-04
R(32,37)	1.0852	1.0858	1.0851	0.0006	1E-04
R(34,36)	1.4043	1.4049	1.4043	0.0006	0
R(34,38)	1.0852	1.0858	1.0851	0.0006	1E-04
R(36,49)	1.4348	1.4341	1.4348	0.0007	0
R(39,40)	1.4062	1.405	1.4074	0.0012	0.0012
R(39,41)	1.4059	1.4049	1.407	0.001	0.0011
R(40,42)	1.3921	1.394	1.3904	0.0019	0.0017
R(40,43)	1.0866	1.0866	1.0858	0	0.0008
R(41,44)	1.3923	1.3942	1.3906	0.0019	0.0017
R(41,45)	1.0866	1.0864	1.0857	0.0002	0.0009
R(42,46)	1.4019	1.3995	1.4045	0.0024	0.0026
R(42,47)	1.0852	1.0861	1.0852	0.0009	0
R(44,46)	1.4016	1.3992	1.4043	0.0024	0.0027
R(44,48)	1.0852	1.0861	1.0851	0.0009	1E-04
R(46,71)	1.4159	1.426	1.4191	0.0101	0.0032
R(49,50)	1.1632	1.1642	1.1629	0.001	0.0003
R(51,53)	1.3976	1.3984	1.4015	0.0008	0.0039
R(51,54)	1.4175	1.4196	1.4199	0.0021	0.0024
R(51,71)	1.4029	1.3967	1.3981	0.0062	0.0048
R(52,55)	1.3976	1.3984	1.4015	0.0008	0.0039

R(52,56)	1.4175	1.4197	1.42	0.0022	0.0025
R(52,71)	1.403	1.3967	1.3981	0.0063	0.0049
R(53,57)	1.3935	1.3927	1.3956	0.0008	0.0021
R(53,58)	1.0848	1.0849	1.0838	1E-04	0.001
R(54,56)	1.4482	1.4472	1.4616	0.001	0.0134
R(54,59)	1.3996	1.4001	1.3847	0.0005	0.0149
R(55,60)	1.3936	1.3927	1.3956	0.0009	0.002
R(55,61)	1.0848	1.0849	1.0838	1E-04	0.001
R(56,62)	1.3996	1.4001	1.3847	0.0005	0.0149
R(57,63)	1.405	1.4064	1.4005	0.0014	0.0045
R(57,64)	1.0866	1.0869	1.0848	0.0003	0.0018
R(59,63)	1.3917	1.3917	1.4093	0	0.0176
R(59,65)	1.0869	1.0873	1.0855	0.0004	0.0014
R(60,66)	1.405	1.4064	1.4004	0.0014	0.0046
R(60,67)	1.0866	1.0869	1.0848	0.0003	0.0018
R(62,66)	1.3917	1.3917	1.4093	0	0.0176
R(62,68)	1.0869	1.0873	1.0855	0.0004	0.0014
R(63,69)	1.0862	1.0867	1.0854	0.0005	0.0008
R(66,70)	1.0862	1.0867	1.0854	0.0005	0.0008

Pentacene

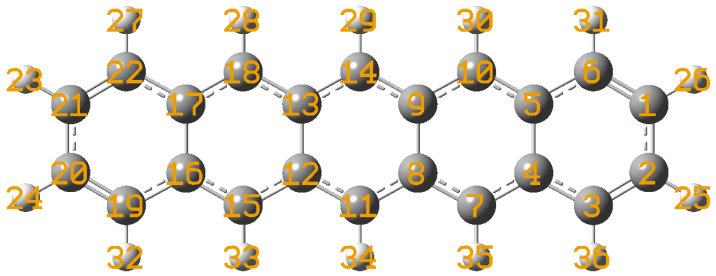

Bonds	R(0)/Å	R(-)/Å	R(+)/Å	|R(-)-R(0)| /Å	|R(+)-R(0)| /Å
R(1,2)	1.4337	1.4185	1.4198	0.0152	0.0139
R(1,6)	1.365	1.3797	1.377	0.0147	0.012
R(1,26)	1.0867	1.0885	1.0856	0.0018	0.0011
R(2,3)	1.365	1.3797	1.377	0.0147	0.012
R(2,25)	1.0867	1.0885	1.0856	0.0018	0.0011
R(3,4)	1.4364	1.425	1.4227	0.0114	0.0137
R(3,36)	1.0876	1.0896	1.0863	0.002	0.0013
R(4,5)	1.455	1.4507	1.4478	0.0043	0.0072
R(4,7)	1.3886	1.4049	1.4036	0.0163	0.015
R(5,6)	1.4364	1.425	1.4227	0.0114	0.0137
R(5,10)	1.3886	1.4049	1.4036	0.0163	0.015
R(6,31)	1.0876	1.0896	1.0863	0.002	0.0013
R(7,8)	1.4152	1.4087	1.4053	0.0065	0.0099
R(7,35)	1.0882	1.09	1.0873	0.0018	9E-04
R(8,9)	1.4566	1.4634	1.455	0.0068	0.0016

R(8,11)	1.4023	1.4087	1.4063	0.0064	0.004
R(9,10)	1.4152	1.4087	1.4053	0.0065	0.0099
R(9,14)	1.4023	1.4087	1.4063	0.0064	0.004
R(10,30)	1.0882	1.09	1.0873	0.0018	9E-04
R(11,12)	1.4022	1.4087	1.4063	0.0065	0.0041
R(11,34)	1.0881	1.0898	1.0873	0.0017	8E-04
R(12,13)	1.4566	1.4634	1.455	0.0068	0.0016
R(12,15)	1.4152	1.4087	1.4053	0.0065	0.0099
R(13,14)	1.4022	1.4087	1.4063	0.0065	0.0041
R(13,18)	1.4152	1.4087	1.4053	0.0065	0.0099
R(14,29)	1.0881	1.0898	1.0873	0.0017	8E-04
R(15,16)	1.3885	1.4049	1.4036	0.0164	0.0151
R(15,33)	1.0882	1.09	1.0873	0.0018	9E-04
R(16,17)	1.4551	1.4507	1.4478	0.0044	0.0073
R(16,19)	1.4364	1.425	1.4227	0.0114	0.0137
R(17,18)	1.3885	1.4049	1.4036	0.0164	0.0151
R(17,22)	1.4364	1.425	1.4227	0.0114	0.0137
R(18,28)	1.0882	1.09	1.0873	0.0018	9E-04
R(19,20)	1.365	1.3797	1.377	0.0147	0.012
R(19,32)	1.0876	1.0896	1.0863	0.002	0.0013
R(20,21)	1.4337	1.4185	1.4198	0.0152	0.0139
R(20,24)	1.0867	1.0885	1.0856	0.0018	0.0011

R(21,22)	1.365	1.3797	1.377	0.0147	0.012
R(21,23)	1.0867	1.0885	1.0856	0.0018	0.0011
R(22,27)	1.0876	1.0896	1.0863	0.002	0.0013
dipentacene POSS 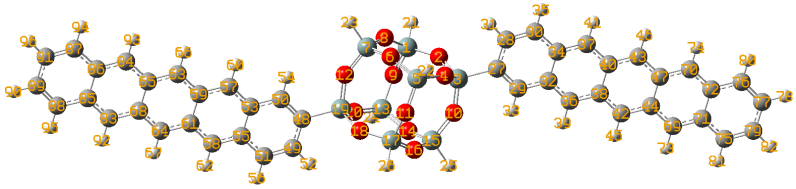					
R(1,2)	1.6401	1.6356	1.6445	0.0045	0.0044
R(1,8)	1.6451	1.6459	1.6443	8E-04	8E-04
R(1,9)	1.6438	1.6449	1.6426	0.0011	0.0012
R(1,21)	1.4652	1.4669	1.4638	0.0017	0.0014
R(2,3)	1.6487	1.6538	1.6443	0.0051	0.0044
R(3,4)	1.6487	1.6538	1.6443	0.0051	0.0044
R(3,10)	1.6463	1.6503	1.6431	0.004	0.0032
R(3,27)	1.8466	1.8366	1.8562	0.01	0.0096
R(4,5)	1.6401	1.6356	1.6445	0.0045	0.0044
R(5,6)	1.6451	1.6459	1.6443	8E-04	8E-04
R(5,11)	1.6438	1.6449	1.6426	0.0011	0.0012
R(5,22)	1.4652	1.4669	1.4638	0.0017	0.0014
R(6,7)	1.6429	1.6442	1.6417	0.0013	0.0012
R(7,8)	1.6429	1.6442	1.6417	0.0013	0.0012

R(7,12)	1.6424	1.6375	1.6469	0.0049	0.0045
R(7,23)	1.4658	1.4671	1.4646	0.0013	0.0012
R(9,13)	1.6438	1.6449	1.6426	0.0011	0.0012
R(10,15)	1.6424	1.6375	1.6469	0.0049	0.0045
R(11,17)	1.6438	1.6449	1.6426	0.0011	0.0012
R(12,19)	1.6463	1.6503	1.6431	0.004	0.0032
R(13,14)	1.6451	1.6459	1.6443	8E-04	8E-04
R(13,20)	1.6401	1.6356	1.6445	0.0045	0.0044
R(13,24)	1.4652	1.4669	1.4638	0.0017	0.0014
R(14,15)	1.6429	1.6442	1.6417	0.0013	0.0012
R(15,16)	1.6429	1.6442	1.6417	0.0013	0.0012
R(15,25)	1.4658	1.4671	1.4646	0.0013	0.0012
R(16,17)	1.6451	1.6459	1.6443	8E-04	8E-04
R(17,18)	1.6401	1.6356	1.6445	0.0045	0.0044
R(17,26)	1.4652	1.4669	1.4638	0.0017	0.0014
R(18,19)	1.6487	1.6538	1.6443	0.0051	0.0044
R(19,20)	1.6487	1.6538	1.6443	0.0051	0.0044
R(19,48)	1.8466	1.8366	1.8562	0.01	0.0096
R(27,28)	1.4451	1.4381	1.4377	0.007	0.0074
R(27,29)	1.3741	1.3835	1.3783	0.0094	0.0042
R(28,30)	1.3634	1.369	1.3691	0.0056	0.0057
R(28,31)	1.087	1.0876	1.0866	6E-04	4E-04

R(29,32)	1.4349	1.4272	1.4296	0.0077	0.0053
R(29,33)	1.0875	1.0879	1.087	4E-04	5E-04
R(30,34)	1.4359	1.4315	1.429	0.0044	0.0069
R(30,35)	1.0875	1.0883	1.0869	8E-04	6E-04
R(32,34)	1.4535	1.4516	1.4491	0.0019	0.0044
R(32,36)	1.389	1.3979	1.3959	0.0089	0.0069
R(34,37)	1.3878	1.3939	1.3959	0.0061	0.0081
R(36,38)	1.4149	1.4111	1.4099	0.0038	0.005
R(36,39)	1.0881	1.0887	1.0876	6E-04	5E-04
R(37,40)	1.4158	1.4138	1.4099	0.002	0.0059
R(37,41)	1.0881	1.0888	1.0875	7E-04	6E-04
R(38,40)	1.4572	1.4605	1.456	0.0033	0.0012
R(38,42)	1.4022	1.4053	1.4044	0.0031	0.0022
R(40,43)	1.4017	1.4032	1.4046	0.0015	0.0029
R(42,44)	1.4025	1.4057	1.404	0.0032	0.0015
R(42,45)	1.088	1.0886	1.0876	6E-04	4E-04
R(43,46)	1.088	1.0887	1.0875	7E-04	5E-04
R(43,47)	1.4028	1.4068	1.4039	0.004	0.0011
R(44,47)	1.4569	1.4596	1.4561	0.0027	8E-04
R(44,69)	1.4147	1.4113	1.4099	0.0034	0.0048
R(47,70)	1.4146	1.4105	1.4099	0.0041	0.0047
R(69,71)	1.3891	1.3969	1.3964	0.0078	0.0073

R(69,73)	1.0881	1.0889	1.0876	8E-04	5E-04
R(70,72)	1.3892	1.3972	1.3964	0.008	0.0072
R(70,74)	1.0881	1.0889	1.0875	8E-04	6E-04
R(71,72)	1.4552	1.4521	1.4512	0.0031	0.004
R(71,75)	1.4357	1.4304	1.4289	0.0053	0.0068
R(72,76)	1.4357	1.4302	1.4289	0.0055	0.0068
R(75,79)	1.3656	1.3721	1.3713	0.0065	0.0057
R(75,81)	1.0874	1.0883	1.0867	9E-04	7E-04
R(76,77)	1.3656	1.3723	1.3714	0.0067	0.0058
R(76,80)	1.0875	1.0884	1.0867	9E-04	8E-04
R(77,78)	1.0866	1.0874	1.0859	8E-04	7E-04
R(77,79)	1.433	1.4257	1.4259	0.0073	0.0071
R(79,82)	1.0866	1.0874	1.0859	8E-04	7E-04
R(48,49)	1.4451	1.4381	1.4377	0.007	0.0074
R(48,50)	1.3741	1.3835	1.3783	0.0094	0.0042
R(49,51)	1.3634	1.369	1.3691	0.0056	0.0057
R(49,52)	1.087	1.0876	1.0866	6E-04	4E-04
R(50,53)	1.4349	1.4272	1.4296	0.0077	0.0053
R(50,54)	1.0875	1.0879	1.087	4E-04	5E-04
R(51,55)	1.4359	1.4315	1.429	0.0044	0.0069
R(51,56)	1.0875	1.0883	1.0869	8E-04	6E-04
R(53,55)	1.4535	1.4516	1.4491	0.0019	0.0044

R(53,57)	1.389	1.3979	1.3959	0.0089	0.0069
R(55,58)	1.3878	1.3939	1.3959	0.0061	0.0081
R(57,59)	1.4149	1.4111	1.4099	0.0038	0.005
R(57,60)	1.0881	1.0887	1.0876	6E-04	5E-04
R(58,61)	1.4158	1.4138	1.4099	0.002	0.0059
R(58,62)	1.0881	1.0888	1.0875	7E-04	6E-04
R(59,61)	1.4572	1.4605	1.456	0.0033	0.0012
R(59,63)	1.4022	1.4053	1.4044	0.0031	0.0022
R(61,64)	1.4017	1.4032	1.4046	0.0015	0.0029
R(63,65)	1.4025	1.4057	1.404	0.0032	0.0015
R(63,66)	1.088	1.0886	1.0876	6E-04	4E-04
R(64,67)	1.088	1.0887	1.0875	7E-04	5E-04
R(64,68)	1.4028	1.4068	1.4039	0.004	0.0011
R(65,68)	1.4569	1.4596	1.4561	0.0027	8E-04
R(65,84)	1.4147	1.4113	1.4099	0.0034	0.0048
R(68,83)	1.4146	1.4105	1.4099	0.0041	0.0047
R(83,85)	1.3892	1.3972	1.3964	0.008	0.0072
R(83,92)	1.0881	1.0889	1.0875	8E-04	6E-04
R(84,86)	1.3891	1.3969	1.3964	0.0078	0.0073
R(84,93)	1.0881	1.0889	1.0876	8E-04	5E-04
R(85,86)	1.4552	1.4521	1.4512	0.0031	0.004
R(85,88)	1.4357	1.4302	1.4289	0.0055	0.0068

R(86,87)	1.4357	1.4304	1.4289	0.0053	0.0068
R(87,91)	1.3656	1.3721	1.3713	0.0065	0.0057
R(87,94)	1.0874	1.0883	1.0867	9E-04	7E-04
R(88,89)	1.3656	1.3723	1.3714	0.0067	0.0058
R(88,95)	1.0875	1.0884	1.0867	9E-04	8E-04
R(89,90)	1.0866	1.0874	1.0859	8E-04	7E-04
R(89,91)	1.433	1.4257	1.4259	0.0073	0.0071
R(91,96)	1.0866	1.0874	1.0859	8E-04	7E-04

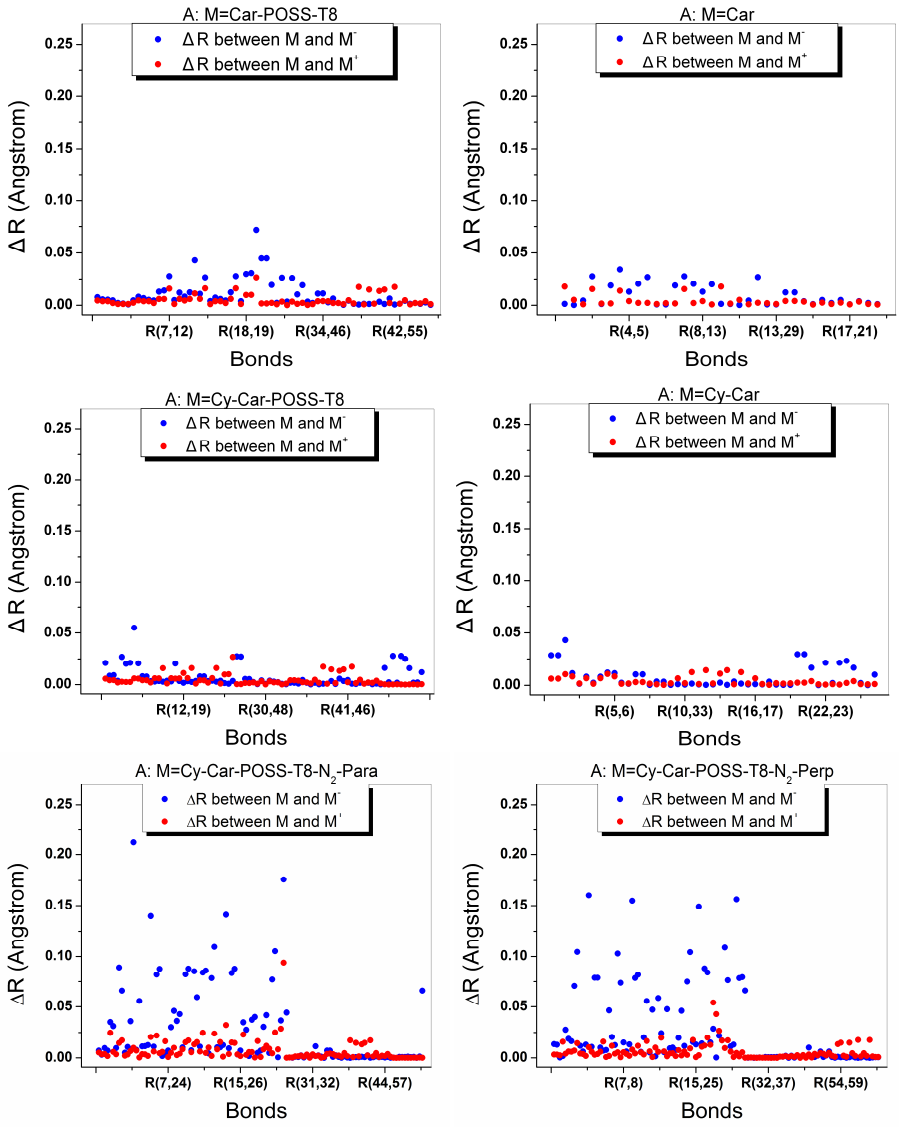

Figure A.1. Bond length changes between optimized neutral and charged geometries.

Appendix B. Survey of fluorescent OLED data published between year 1989 and year 2010

We collected all the data from the journal papers which satisfy the following criteria: (1) the emission is from small molecular fluorescent materials; (2) PL efficiency measured from solid thin film of emitting layer is provided; (3) EQE of the devices is provided; (4) devices are fabricated on planar glass substrates without any out-coupling techniques. Singlet generation fraction is calculated at the approximation of B3LYP/6-31G* (see Chapter 4) except stated. Singlet generation fraction of some host materials is also listed.

Names	Molecular structure	Ebs/eV	Ebt/eV	χ_{FG}	PLQE (%)	Experimental EQE (%)	Calculated EQE Based on χ_{FG}	Calculated EQE based on χ_{SST} = 0.25	Reference
Alq	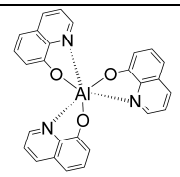	0.503	1.147	0.432	40	3.0	3.30	1.91	12
CBP	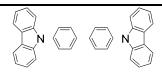	0.522	1.126	0.418	--	--	--	--	This work
B1	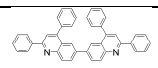	0.406	1.371	0.529	48	4.5	4.86	2.30	3
Bt	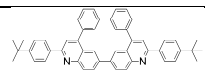	0.409	1.341	0.522	52	4.45	5.19	2.49	3
B2	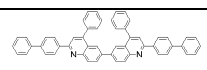	0.400	1.271	0.514	74	6.56	7.28	3.54	3
BD	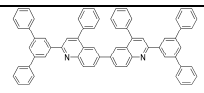	0.417	1.358	0.521	48	4.52	4.78	2.30	3

MPS	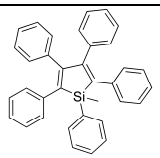	0.486	1.773	0.549	85	8	8.93	4.07	4
NPAFN	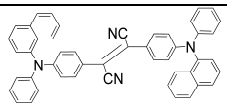	0.346	1.049	0.502	40	2.4	3.84	1.91	5
FPhSPFN	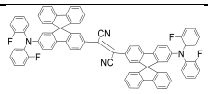	0.342	0.873	0.460	46	3.1	4.05	2.20	5
PhSPFN	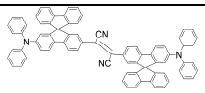	0.314	0.700	0.426	34	1.8	2.77	1.63	5
PPP	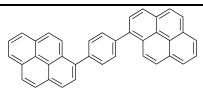	0.290	1.462	0.627	70	4.5	8.39	3.35	6
DMPPP	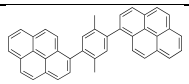	0.271	1.652	0.670	75	5.2	9.62	3.59	6
DOPPP	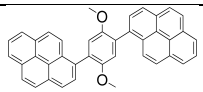	0.361	1.472	0.576	63	3.4	6.95	3.01	6
DPV	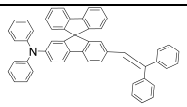	0.368	1.174	0.516	51	3.4	5.03	2.44	7
DCV=PhSPDCV	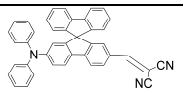	0.220	0.801	0.548	33	3.6	3.46	1.58	8
CHO	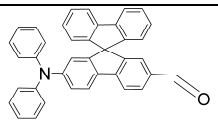	0.321	0.981	0.505	42	2.7	4.06	2.01	8
pTFDCV	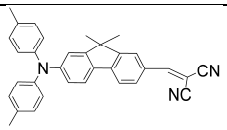	0.209	0.772	0.552	27	2.1	2.85	1.29	8
pTSPDCV	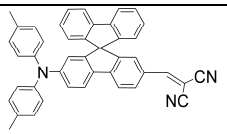	0.213	0.769	0.547	25	2.6	2.61	1.20	8
2DPV(at B3LYP/3-21g)	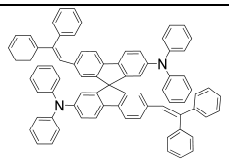	0.403	1.100	0.476	21	2.8	2.61	1.00	8

2DCV	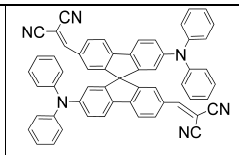	0.387	0.777	0.401	6	0.69	0.46	0.29	8
2CHO	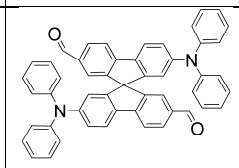	0.442	0.909	0.407	10	0.8	0.78	0.48	8
2PSP	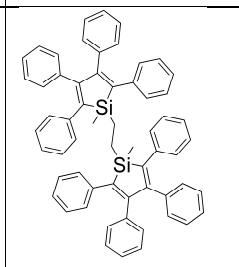	0.481	1.711	0.542	97	4.8	10.06	4.64	9 10
TDAF1	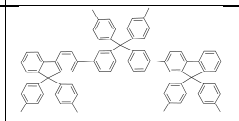	0.419	1.276	0.504	90	5.3	8.67	4.30	11 12
TDAF2	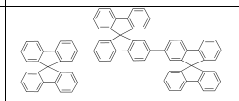	0.419	1.281	0.505	90	4.1	8.69	4.30	11 12
D1	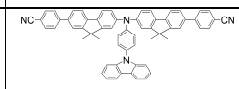	0.356	0.814	0.432	90	2.6	7.47	4.32	This work
D2	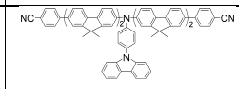	0.275	0.689	0.455	93	6.2	8.11	4.45	This work
D3	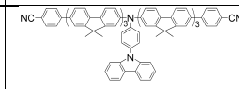	0.199	0.628	0.513	54	4.5	5.25	2.56	This work
CzPhB	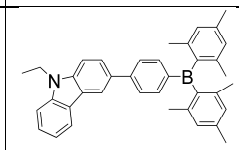	0.398	0.946	0.442	54	4.3	4.57	2.58	13
CzThB	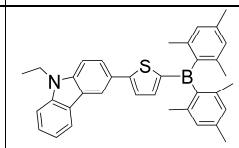	0.395	1.236	0.511	51	6.9	4.98	2.44	13
Pu1	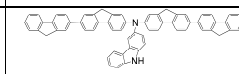	0.406	0.936	0.435	34	1.35	2.83	1.63	14
Pu2	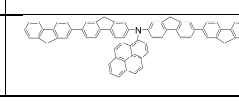	0.435	1.116	0.461	40	1.06	3.53	1.91	14

Pu3	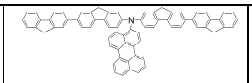	0.370	1.205	0.520	23	0.93	2.29	1.10	14
Pu4	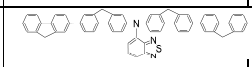	0.469	0.985	0.412	10	0.6	0.79	0.48	14
AC5 (doped in CBP)	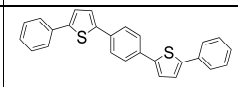	0.327	1.372	0.583	84	4.8	8.04	4.02	15
HPICbz	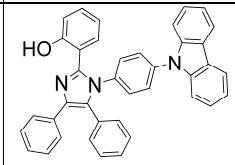	0.556	1.294	0.437	44	2.94	3.68	2.10	16
HPIOxd	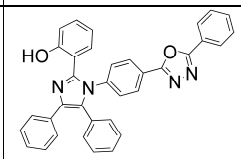	0.470	0.633	0.310	38	1.36	2.25	1.82	16
TCB2	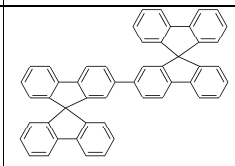	0.409	1.442	0.541	66	3.6	6.83	3.16	17
TCT2	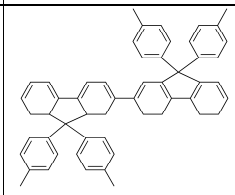	0.404	1.440	0.543	63	2.8	6.54	3.01	17
TCTB2	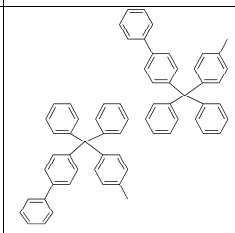	0.410	1.434	0.538	57	2.7	5.87	2.73	17
HC5a	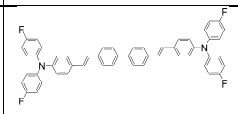	0.342	1.154	0.529	89	4.87	9.01	4.26	18
DFBTA	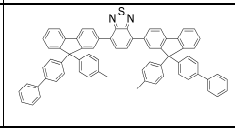	0.438	1.235	0.484	81	3.7	7.51	3.87	19

TDPVBi	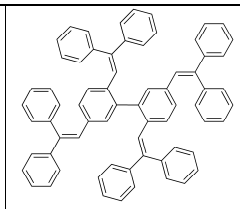	0.419	1.407	0.528	80	3.8	8.08	3.83	20
PPSPP	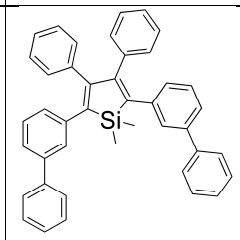	0.498	1.802	0.547	85	3.4	8.89	4.07	9
JNM1	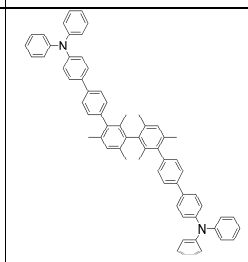	0.274	1.572	0.657	52	4.09	6.54	2.49	21
JNM2	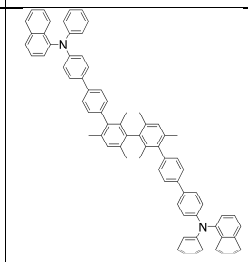	0.602	1.636	0.475	17	4.23	1.55	0.81	21
BPPB	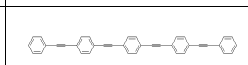	0.314	1.185	0.557	71	0.53	7.57	3.40	22
TBPSF	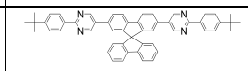	0.428	1.249	0.493	80	2.3	7.55	3.83	23
TPF	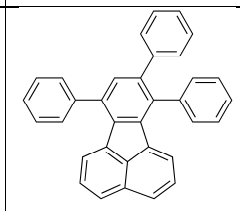	0.516	1.487	0.490	51	1.83	4.78	2.44	24
In2Bt	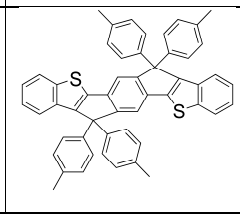	0.338	1.391	0.578	14	1.3	1.55	0.67	25

MYL1	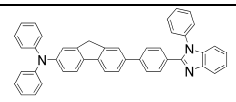	0.361	0.991	0.478	80	3	7.31	3.83	26
MYL2	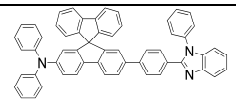	0.369	1.005	0.476	72	1.6	6.55	3.44	26
C545T(doped in TPBA)	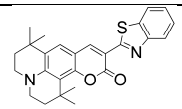	0.218	1.254	0.658	100	9.9	12.41	4.78	27
TPBA	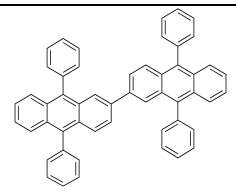	0.286	1.522	0.639	--	--	--	--	27
D1(doped in CBP)	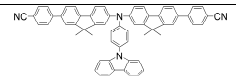	0.356	0.814	0.432	100	8.1	8.13	4.78	This work
D2(doped in CBP)	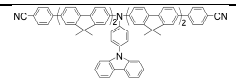	0.275	0.689	0.455	100	9.4	8.35	4.78	This work
D3(doped in CBP)	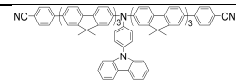	0.199	0.628	0.513	100	10.7	8.91	4.78	This work
DCM(doped in Alq)	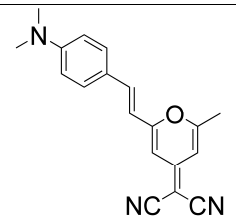	0.137	1.263	0.754	30	4.2	3.40	1.43	28
J1	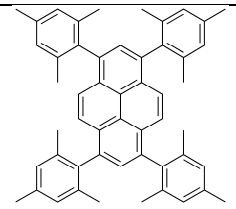	0.190	1.643	0.742	30	2.6	4.26	1.43	29
J2	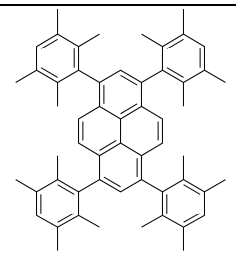	0.197	1.639	0.735	24	1.01	3.38	1.15	29

J3	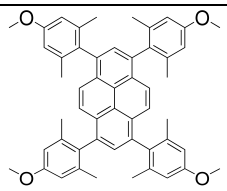	0.191	1.642	0.741	44	3.26	6.24	2.10	29
BFAn	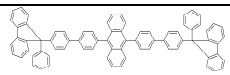	0.348	1.740	0.625	84	5.1	10.05	4.02	30
DPP(doped in Alq)	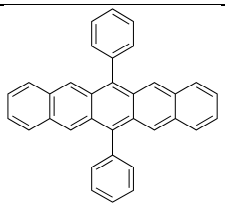	0.277	1.623	0.662	30	1.3	3.14	1.43	31
POAn	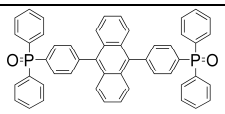	0.340	1.758	0.633	71	4.7	8.59	3.40	32
PHP	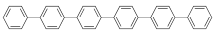	0.418	1.378	0.524	30	3.4	3.01	1.43	33 34
Almq	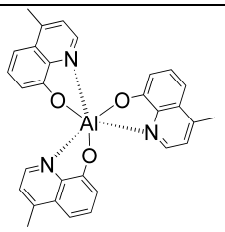	0.498	1.140	0.433	42	2.5	3.31	1.91	35 36
AlmmND	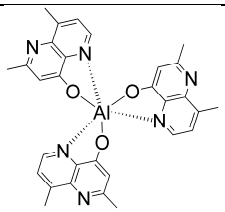	0.512	1.206	0.440	39	4.18	3.28	1.87	1
DEQ(doped in Almq)	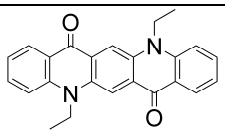	0.383	1.099	0.489	73	2.7	6.43	3.49	37
Rubrene(doped in Almq)	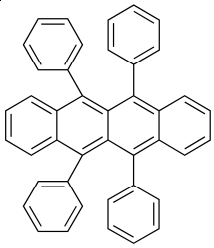	0.325	1.562	0.615	77	2.9	7.72	3.68	37

DMPP(doped in Alq)	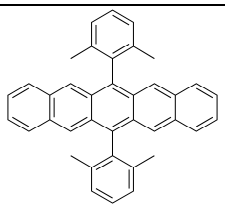	0.279	1.624	0.660	30	1.6	3.13	1.43	38
DtPP(doped in Alq)	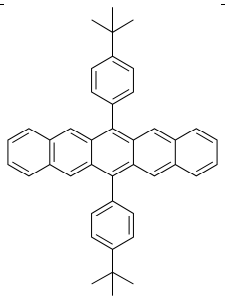	0.243	1.605	0.688	32	1.4	3.43	1.53	39
ASP	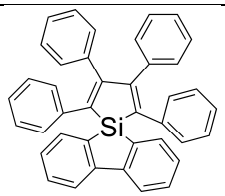	0.509	1.730	0.531	87	4.3	8.84	4.16	9
TPP	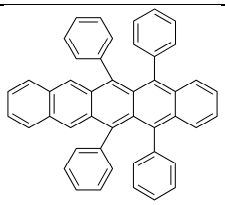	0.300	1.579	0.637	22	0.8	2.68	1.05	40
DMPDPP	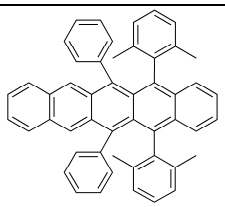	0.305	1.594	0.635	19	0.9	2.31	0.91	40
FLBD(doped in FLBH)	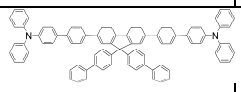	0.353	0.947	0.472	91	5.4	8.63	4.35	41
FLBH	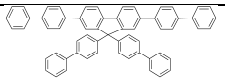	0.413	1.338	0.519	--	--	--	--	41
DPA-DSB(doped in TSB)	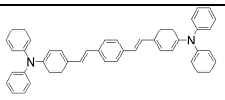	0.311	1.205	0.564	68	6.2	7.47	3.25	42
TSB	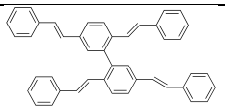	0.324	1.368	0.585			--	--	42

HZ1	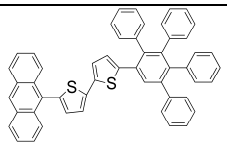	0.491	1.653	0.529	40	1.85	4.05	1.91	43
ET2ME(doped in CBP 3% mol)	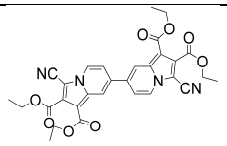	0.338	1.340	0.569	67	1.8	6.33	3.20	44
JYS7	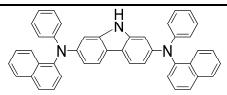	0.499	1.058	0.414	21	1.9	1.66	1.00	45
JYS9	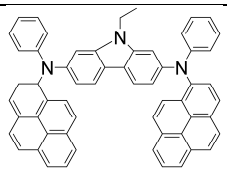	0.404	1.058	0.466	32	2.4	2.85	1.53	45
TP5(doped in Alq)	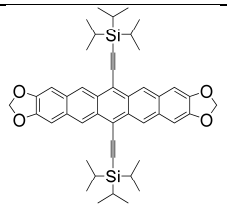	0.230	1.412	0.672	59	2.8	6.23	2.82	46
EtTP5(doped in Alq)	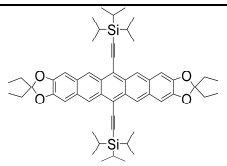	0.234	1.401	0.666	76	3.3	7.98	3.63	46
NPAML1	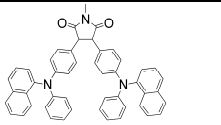	0.425	1.000	0.440	15	2.4	1.26	0.72	47
SSS	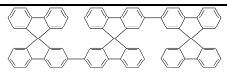	0.432	1.405	0.520	56	2.6	5.57	2.68	48
TST	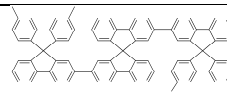	0.426	1.405	0.524	60	3.1	6.01	2.87	48
BTP	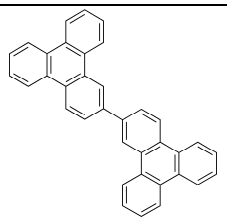	0.430	1.530	0.543	46	4.2	4.78	2.20	49

T1	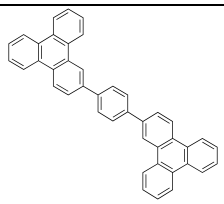	0.426	1.434	0.529	60	4.6	6.07	2.87	49
T2	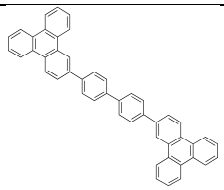	0.428	1.367	0.516	66	5.2	6.51	3.16	49
BPYPQ	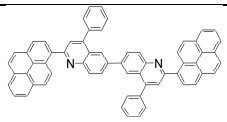	0.327	1.237	0.558	50	3.5	5.34	2.39	50
B3PPQ	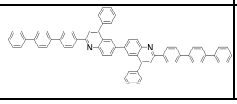	0.387	1.217	0.512	57	3.4	5.58	2.73	50

References:

(1) Liao, S. H.; Shiu, J. R.; Liu, S. W.; Yeh, S. J.; Chen, Y. H.; Chen, C. T.; Chow, T. J.; Wu, C. I. *J. Am. Chem. Soc.* **2009**, *131*, 763-777.

(2) Li, W. X.; Jones, R. A.; Allen, S. C.; Heikenfeld, J. C.; Steckl, A. J. *J. Display Technol.* **2006**, *2*, 143-152.

(3) Tonzola, C. J.; Kulkarni, A. P.; Gifford, A. P.; Kaminsky, W.; Jenekhe, S. A. *Adv. Funct. Mater.* **2007**, *17*, 863-874.

(4) Chen, H. Y.; Lam, W. Y.; Luo, J. D.; Ho, Y. L.; Tang, B. Z.; Zhu, D. B.; Wong, M.; Kwok, H. S. *Appl. Phys. Lett.* **2002**, *81*, 574-576.

(5) Lee, Y. T.; Chiang, C. L.; Chen, C. T. *Chem. Comm.* **2008**, 217-219.

(6) Wu, K. C.; Ku, P. J.; Lin, C. S.; Shih, H. T.; Wu, F. I.; Huang, M. J.; Lin, J. J.; Chen, I. C.; Cheng, C. H. *Adv. Funct. Mater.* **2008**, *18*, 67-75.

(7) Chiang, C. L.; Tseng, S. M.; Chen, C. T.; Hsu, C. P.; Shu, C. F. *Adv. Funct. Mater.* **2008**, *18*, 248-257.

(8) Chiang, C. L.; Wu, M. T.; Dai, D. C.; Wen, Y. S.; Wang, J. K.; Chen, C. T. *Adv. Funct. Mater.* **2005**, *15*, 231-238.

(9) Palilis, L. C.; Murata, H.; Uchida, M.; Kafafi, Z. H. *Org. Electron.* **2003**, *4*, 113-121.

(10) Murata, H.; Kafafi, Z. H.; Uchida, M. *Appl. Phys. Lett.* **2002**, *80*, 189-191.

(11) Wu, C. C.; Lin, Y. T.; Wong, K. T.; Chen, R. T.; Chien, Y. Y. *Adv. Mater.* **2004**, *16*, 61.

(12) Wong, K. T.; Chien, Y. Y.; Chen, R. T.; Wang, C. F.; Lin, Y. T.; Chiang, H. H.; Hsieh, P. Y.; Wu, C. C.; Chou, C. H.; Su, Y. O.; Lee, G. H.; Peng, S. M. *J. Am. Chem. Soc.* **2002**, *124*, 11576-11577.

(13) Lin, S. L.; Chan, L. H.; Lee, R. H.; Yen, M. Y.; Kuo, W. J.; Chen, C. T.; Jeng, R. J. *Adv. Mater.* **2008**, *20*, 3947.

(14) Pu, Y. J.; Higashidate, M.; Nakayama, K.; Kido, J. *J. Mater. Chem.* **2008**, *18*, 4183-4188.

(15) Matsushima, T.; Adachi, C. *Chem. Mater.* **2008**, *20*, 2881-2883.

(16) Park, S.; Seo, J.; Kim, S. H.; Park, S. Y. *Adv. Funct. Mater.* **2008**, *18*, 726-731.

(17) Chao, T. C.; Lin, Y. T.; Yang, C. Y.; Hung, T. S.; Chou, H. C.; Wu, C. C.; Wong, K. T. *Adv. Mater.* **2005**, *17*, 992.

(18) Li, H. C.; Lin, Y. P.; Chou, P. T.; Cheng, Y. M.; Liu, R. S. *Adv. Funct. Mater.* **2007**, *17*, 520-530.

(19) Ku, S. Y.; Chi, L. C.; Hung, W. Y.; Yang, S. W.; Tsai, T. C.; Wong, K. T.; Chen, Y. H.; Wu, C. I. *J. Mater. Chem.* **2009**, *19*, 773-780.

(20) Liu, S. J.; He, F.; Wang, H.; Xu, H.; Wang, C. Y.; Li, F.; Ma, Y. G. *J. Mater. Chem.* **2008**, *18*, 4802-4807.

(21) Moorthy, J. N.; Venkatakrishnan, P.; Huang, D. F.; Chow, T. J. *Chem. Comm.* **2008**, 2146-2148.

(22) Fenenko, L.; Shao, G.; Orita, A.; Yahiro, M.; Otera, J.; Svechnikov, S.; Adachi, C. *Chem. Comm.* **2007**, 2278-2280.

(23) Wu, C. C.; Lin, Y. T.; Chiang, H. H.; Cho, T. Y.; Chen, C. W.; Wong, K. T.; Liao, Y. L.; Lee, G. H.; Peng, S. M. *Appl. Phys. Lett.* **2002**, *81*, 577-579.

(24) Chiechi, R. C.; Tseng, R. J.; Marchioni, F.; Yang, Y.; Wudl, F. *Adv. Mater.* **2006**, *18*, 325.

(25) Tsai, T. C.; Hung, W. Y.; Chi, L. C.; Wong, K. T.; Hsieh, C. C.; Chou, P. T. *Org. Electron.* **2009**, *10*, 158-162.

(26) Lai, M. Y.; Chen, C. H.; Huang, W. S.; Lin, J. T.; Ke, T. H.; Chen, L. Y.; Tsai, M. H.; Wu, C. C. *Angew. Chem. Int. Ed.* **2008**, *47*, 581-585.

(27) Okumoto, K.; Kanno, H.; Hamaa, Y.; Takahashi, H.; Shibata, K. *Appl. Phys. Lett.* **2006**, *89*,

(28) Littman, J.; Martic, P. *J. Appl. Phys.* **1992**, *72*, 1957-1960.

(29) Moorthy, J. N.; Natarajan, P.; Venkatakrishnan, P.; Huang, D. F.; Chow, T. J. *Org. Lett.* **2007**, *9*, 5215-5218.

(30) Wu, C. H.; Chien, C. H.; Hsu, F. M.; Shih, P. I.; Shu, C. F. *J. Mater. Chem.* **2009**, *19*, 1464-1470.

(31) Picciolo, L. C.; Murata, H.; Kafafi, Z. H. *Appl. Phys. Lett.* **2001**, *78*, 2378-2380.

(32) Chien, C. H.; Chen, C. K.; Hsu, F. M.; Shu, C. F.; Chou, P. T.; Lai, C. H. *Adv. Funct. Mater.* **2009**, *19*, 560-566.

(33) Stampf, J.; Tasch, S.; Leising, G.; Scherf, U. *Synth. Met.* **1995**, *71*, 2125-2128.

(34) Winkler, B.; Meghdadi, F.; Tasch, S.; Evers, B.; Schneider, I.; Fischer, W.; Stelzer, F.; Leising, G. *Synth. Met.* **1999**, *102*, 1083-1084.

(35) Kido, J.; Iizumi, Y. *Appl. Phys. Lett.* **1998**, *73*, 2721-2723.

(36) Mattoussi, H.; Murata, H.; Merritt, C. D.; Iizumi, Y.; Kido, J.; Kafafi, Z. H. *J. Appl. Phys.* **1999**, *86*, 2642-2650.

(37) Kafafi, Z. H.; Murata, H.; Picciolo, L. C.; Mattoussi, H.; Merritt, C. D.; Iizumi, Y.; Kido, J. *Pure App. Chem.* **1999**, *71*, 2085-2094.

(38) Palilis, L. C.; Melinger, J. S.; Wolak, M. A.; Kafafi, Z. H. *J. Phys. Chem. B* **2005**, *109*, 5456-5463.

(39) Wolak, M. A.; Jang, B. B.; Palilis, L. C.; Kafafi, Z. H. *J. Phys. Chem. B* **2004**, *108*, 5492-5499.

(40) Jang, B. B.; Lee, S. H.; Kafafi, Z. H. *Chem. Mater.* **2006**, *18*, 449-457.

(41) Matsumoto, N.; Miyazaki, T.; Nishiyama, M.; Adachi, C. *J. Phys. Chem. C* **2009**, *113*, 6261-6266.

(42) He, F.; Tian, L. L.; Xie, W. J.; Li, M.; Gao, Q.; Hanif, M.; Zhang, Y. F.; Cheng, G.; Yang, B.; Ma, Y. G.; Liu, S. Y.; Shen, J. C. *J. Phys. Chem. C* **2008**, *112*, 12024-12029.

(43) Zhang, H. J.; Xu, X. J.; Qiu, W. F.; Qi, T.; Gao, X. K.; Liu, Y.; Lu, K.; Du, C. Y.; Yu, G.; Liu, Y. Q. *J. Phys. Chem. C* **2008**, *112*, 13258-13263.

(44) Matsushima, T.; Kimura, R.; Asahara, M.; Murata, H. *Chem. Lett.* **2008**, *37*, 1260-1261.

(45) Shen, J. Y.; Yang, X. L.; Huang, T. H.; Lin, J. T.; Ke, T. H.; Chen, L. Y.; Wu, C. C.; Yeh, M. C. P. *Adv. Funct. Mater.* **2007**, *17*, 983-995.

(46) Wolak, M. A.; Delcamp, J.; Landis, C. A.; Lane, P. A.; Anthony, J.; Kafafi, Z. *Adv. Funct. Mater.* **2006**, *16*, 1943-1949.

(47) Wu, W. C.; Yeh, H. C.; Chan, L. H.; Chen, C. T. *Adv. Mater.* **2002**, *14*, 1072.

(48) Wong, K. T.; Liao, Y. L.; Lin, Y. T.; Su, H. C.; Wu, C. C. *Org. Lett.* **2005**, *7*, 5131-5134.

(49) Yu, J. Y.; Huang, M. J.; Chen, C. H.; Lin, C. S.; Cheng, C. H. *J. Phys. Chem. C* **2009**, *113*, 7405-7410.

(50) Hancock, J. M.; Gifford, A. P.; Tonzola, C. J.; Jenekhe, S. A. *J. Phys. Chem. C* **2007**, *111*, 6875-6882.